CHAPTER 4

AIRCRAFT DYNAMICS AND CLASSICAL CONTROL DESIGN

4.1 INTRODUCTION

In the previous chapters we have developed mathematical tools, realistic aircraft models, and algorithms for performing flight simulation and flight control design. Before we attempt to use all of these tools, models, and algorithms, we must have a clear idea of their applicability and the rationale and design goals for automatic flight control systems. Some idea of the history of the development of automatic flight controls is helpful in this respect.

Historical Perspective

The success of the Wright brothers in achieving the first powered flight in December 1903 has been attributed to both their systematic design approach (they built and used a wind tunnel) and the emphasis they placed on making their aircraft controllable by the pilot rather than inherently stable. However, the difficulties of controlling the early aircraft and the progress toward longer flight times led quickly to the development of an automatic control system. Thus, in 1912 an autopilot was developed by the Sperry Gyroscope Company and tested on a Curtiss flying boat. By 1914 the "Sperry Aeroplane Stabilizer" had reached such a state of development that a public flying demonstration was given in which the mechanic walked along the wing while the pilot raised his hands from the controls.

World War I (1914–1918) provided the impetus for great progress in aircraft design. However, a human pilot was perfectly capable of providing the normal stabilizing and control functions for the aircraft of this era, and the time was not ripe for rapid developments in automatic control. The small-perturbation theory of aircraft

Aircraft Control and Simulation: Dynamics, Controls Design, and Autonomous Systems, Third Edition.
Brian L. Stevens, Frank L. Lewis, Eric N. Johnson.

dynamics had been developed (Bryan, 1911), and in the 1920s stability derivatives were measured and calculated and the theory was confirmed by flight tests. Little practical use was made of the theory because even the problem of finding the roots of a quartic equation was difficult at the time. Development of autopilots continued, using gyroscopes as the reference sensor and pneumatic servomechanisms to position the control surfaces. A Sperry autopilot also helped Wiley Post to fly around the world in less than eight days in 1933.

In the late 1930s classical control theory began to develop. The need to design stable telephone repeater amplifiers with closely controlled gain led to the work of Black in "regeneration theory" and to Nyquist's frequency-domain stability criterion. The same stimuli also led to Bode's complex-frequency-domain theory for the relationships between gain and phase and his logarithmic plots of gain and phase. World War II (1939–1945) led to further developments in control theory because of the need for radar tracking and the development of servomechanisms for positioning guns and radar antennas. Once again wartime spurred improvements in aircraft design. The large expansion of the speed-altitude envelope and the need to carry and dispose of large payloads led to large variations in the aircraft dynamics, thus creating a need to analyze the dynamic behavior. Larger aircraft required power-boosted control surfaces, and developments in hydraulic servomechanisms resulted. Also, the need to fly at night and in bad weather conditions led to developments in radio navigation aids and a need to couple these aids to the autopilot. Thus, in 1947, a U.S. Air Force C-53 made a transatlantic flight, including takeoff and landing, completely under the control of an autopilot.

By the late 1940s the concepts of frequency response and transfer functions had become more generally known and the first analog computers were becoming available. The root-locus technique, published by W. R. Evans in 1948, was a major development in analyzing and designing control systems (it is even more useful in the computer age!). Analyses of the stability and performance of aircraft under automatic control began to be performed more commonly by the aircraft companies. The aircraft altitude-speed envelope was being expanded rapidly by the first jet fighters and by a series of research aircraft (the "x" series in the United States).

The rocket-powered Bell X-1aircraft made its first flight in January 1946; in October 1947 it achieved supersonic flight, and in August 1949 an altitude of nearly 72,000 ft was reached. The envelope was extended further by the next generation of X-planes, X-1A through X-1D. After reaching Mach 2.44 and 75,000 ft altitude, *inertia coupling* (see Chapter 1 Section Angular Motion and Section Control Augmentation Systems) caused the X-1A to spin around all three axes, almost killing the pilot, Major Charles Yeager. Inertia coupling effects were encountered because these aircraft had the basic form of a modern jet fighter with short stubby wings, most of the mass concentrated along the longitudinal axis, and relatively small tail surfaces for directional stability. Before the problem was fully understood, a number of aircraft of the period suffered inertia coupling effects, sometimes with disastrous results. These included the X-2 and X-3 and the F-100 jet fighter during the course of its production program in 1953.

Many other factors besides inertia coupling contributed to the need for a more analytical approach to aircraft stability and control problems. The changes in aircraft

mass properties, together with the need to reduce the area of the aerodynamic surfaces (for lower drag at high speed), caused changes in the natural modes of the aircraft, so that they were no longer easily controllable by the pilot. In addition, the damping of the natural modes tended to decrease as the altitude limits of the airplanes were expanded; these factors made it more important to predict the frequency and damping of the modes analytically. Also, the expansion of the aircraft speed-altitude envelope meant that much greater variations in the dynamics of the aircraft were encountered.

Power-boosted or fully powered control surfaces were introduced because of the increasing aerodynamic loads associated with greater performance and larger aircraft and because they could eliminate the many hours of flight test needed to balance the control surfaces carefully. Properly balanced control surfaces were previously necessary to provide a suitable feel to the pilot's controls. With power-boosted controls the feel could be modified with springs and bobweights, and with fully powered irreversible controls the feel could be provided completely artificially. Thus, the "handling qualities" of the aircraft could be adjusted to be satisfactory over a very wide envelope. Power-boosted controls also made possible the use of *stability augmentation*, in which signals from angular rate sensors could be fed to the control surface actuators to modify the natural modes of the aircraft. In addition, they facilitated the use of more complex autopilots.

The year 1949 saw the first flight of the de Havilland Comet, the aircraft that essentially defined the modern jet transport aircraft. In the early 1950s the problems of supersonic flight up to Mach 3 and beyond were beginning to be investigated. The Lockheed X-7 unmanned rocket plane was built to provide a testbed for a ramjet engine. During a five-year test program beginning in 1951, it also provided information on high-speed aerodynamics, aerothermodynamics, special fuels, and special materials. Data from programs such as this undoubtedly contributed to the design of aircraft such as the F-104 and the SR-71. The X-15 rocket plane, which first flew in 1959, expanded the envelope for manned flight to beyond Mach 6 and above 300,000 ft. This aircraft was equipped with a Honeywell-designed adaptive control system that provided three-axis stability augmentation and a transition from aerodynamic control to reaction control as the aerodynamic controls became ineffective at high altitude.

In the early 1960s small fighter aircraft were approaching Mach 2 speeds; a French Mirage achieved Mach 2.3, and later an F-4 Phantom made a record-breaking Mach 2.4 flight. In the civil aviation field, this was the time of the Boeing 707 and Douglas DC8 passenger jets and the development of the Aerospatiale-British Aerospace Concorde SST. The digital computer was beginning to have a major impact on engineering, the techniques of numerical analysis assumed greater importance, and this stimulated the growth of modern control theory in the mid-1960s.

A great deal of hypersonic aerodynamics knowledge was gained from the X-15 program and from hypersonic wind tunnel studies in the late 1950s. The X-20 (Dyna-Soar) vehicle, to be built by Boeing under a 1960 contract, was to be a rocket-launched unpowered glider that would gather data to solve the problems of pilot-controlled reentry from orbit. The final design was a unique V-shaped vehicle with a thick wing and upturned wing tips. Although the program was canceled

before completion of the first vehicle, it pioneered the technology for the U.S. space shuttle. Later, the unmanned ASSET (1963–1965) and PRIME (X-23A; 1966–1967) vehicles provided flight data on structures, materials, control systems, and other technologies for maneuvering reentry. This was followed in 1969 and the early 1970s by the X-24 manned, blunt lifting body vehicles. These provided data on the low-speed characteristics of maneuverable reentry vehicles, including stability characteristics, pilot experience for comparison with simulators, man-vehicle interface data, and much control system information.

Because of the digital computer, the 1970s saw great strides in computational fluid dynamics, structural and flutter (structural divergence) analysis, simulation of complex dynamical systems, and the application of guidance and control theory in real-time onboard digital computers. Simulation techniques made possible realistic pilot training on the ground, and the automatic flight control system on board an aircraft allowed the dynamic behavior of an entirely different aircraft to be simulated. Thus, space shuttle pilots trained on a Gulfstream-II aircraft that simulated the feel of the space shuttle.

In the 1970s, flight control technology advances allowed the F-16 aircraft to be designed for "relaxed static stability" and all-electric (full "fly-by-wire") control. Previous aircraft had used "high-authority" electrical control superimposed on the basic electrohydraulic system (e.g., the F-111) or, as in the case of the Concorde, an electrical system with mechanical backup. The processing of electrical signals for automatic flight control systems was still in analog rather than digital form.

The 1980s saw the flight testing of aircraft with additional aerodynamic control surfaces that provided direct-lift control or direct sideforce control (such as the AFTI F-16 and the Grumman forward-swept wing X-29A aircraft) and with digital flight control systems (e.g., McDonnell F-15E and F-18). The AFTI F-16 aircraft allowed the use of sideforce control through a ventral fin and direct-lift control through the combination of the horizontal tail and wing leading-edge flaps. The *decoupled motions* provided by this control were evaluated for possible use in combat situations. The X-29A research aircraft is unstable in pitch (−35% static margin at low speed) and has three-surface pitch control (canards, wing flaperons, and strake flaps). The flight control system is a triply redundant digital system (three digital processors with "voting" to eliminate a faulty channel) with analog backup for each processor. These aircraft raise interesting multivariable control problems for modern control theory.

The U.S. space shuttle made its first flight in March 1981. There was also a resurgence of interest in hypersonic flight during the 1980s. Single-stage-to-orbit vehicles were studied, including the British HOTOL (horizontal takeoff and landing) unmanned satellite launch vehicle and the U.S. TAV (Trans-Atmospheric Vehicle)—fully reusable rapid-turnaround vehicles for manned reconnaisance, weapon delivery, and delivery of large payloads to orbit. These were followed in the United States by the NASP (National Aerospace Plane) study contracts on a manned single-stage-to-orbit vehicle. Other studies looked at boosted vehicles; these included the French HERMES vehicle (similar to the space shuttle, manned) and a number of U.S. BGVs (boost-glide vehicles).

Many lessons were learned about the control of hypersonic vehicles. The trajectories must be carefully controlled because the frictional heating in the atmosphere can create temperatures of a few thousand degrees Fahrenheit at critical points on the vehicle. A change in flight conditions can cause localized changes in the airflow, from laminar to turbulent flow, and this can lead to a rapid increase in temperature at some point on the surface of the vehicle. Manual control is difficult or not feasible in most flight phases and, if attempted, would limit the performance. The trajectory can be controlled by feedback comparison with a precomputed reference trajectory or with real-time trajectory prediction calculations (as in the case of the space shuttle).

There can be large uncertainties in the aerodynamic coefficients of the hypersonic vehicles, and this complicates the design of the automatic control systems and limits their performance. The control systems must be adapted (gain scheduled, or self-adaptive) in flight to allow for the wide variations in vehicle dynamics over the large flight envelope. If fixed "scheduling" is used, difficulties are encountered in sensing the flight conditions. External probes sensing "air data" (dynamic pressure and Mach) can only be used at low Mach numbers, and the air data must be derived from the navigation system and a stored model of the atmosphere. The real atmosphere can show large, unpredictable variations in density; therefore, the control systems must be designed to tolerate these variations.

The era of true "aerospace" vehicles introduces many new challenges for the control engineer. He or she must now think in terms of guidance and control, algorithms and simulation, and numerical methods and digital implementation. Many relatively new analytical techniques are required, including numerical optimization, analysis of sensitivity and robustness to parameter variations, adaptive techniques, and multivariable control. Furthermore, the control engineer can no longer work in isolation; many other technologies will be closely integrated into a design, and constraints will be imposed on the designs from a variety of sources (e.g., structural, thermal, propulsion, energy management and performance, and human factors).

The Need for Automatic Control Systems

The evolution of modern aircraft created a need for power-driven aerodynamic control surfaces and automatic pilot control systems, as described in the preceding subsection. In addition, the widening performance envelope created a need to augment the stability of the aircraft dynamics over some parts of the envelope. This need for stability augmentation is now described in more detail.

Figure 4.1-1 shows the altitude-Mach envelope of a modern high-performance aircraft; the boundaries of this envelope are determined by a number of factors. The low-speed limit is set by the maximum lift that can be generated (the alpha limit in the figure), and the high-speed limit follows a constant dynamic pressure contour (because of structural limits, including temperature). At the higher altitudes the speed becomes limited by the maximum engine thrust (which has fallen off with altitude). The altitude limit imposed on the envelope is where the combination of airframe and engine characteristics can no longer produce a certain minimum rate of climb (this is the "service ceiling").

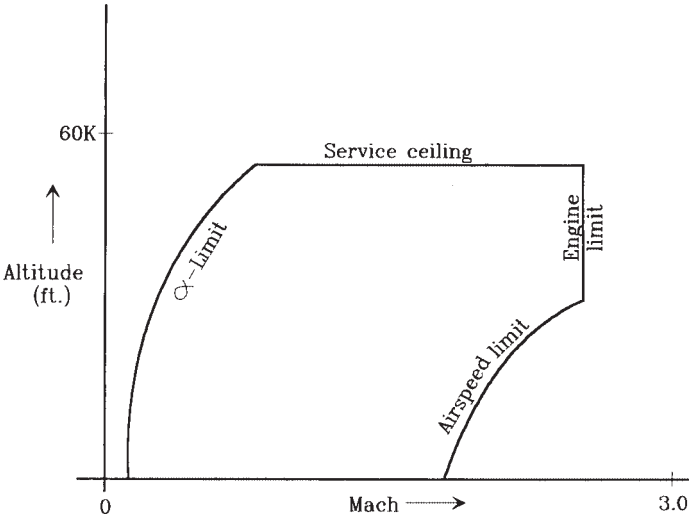

Figure 4.1-1 Aircraft altitude-Mach envelope.

The aircraft envelope covers a very wide range of dynamic pressure. For example, in the landing phase the dynamic pressure may be as low as 50 psf, whereas at Mach 1.2 at sea level the dynamic pressure is 2150 psf. Large variations in dynamic pressure cause correspondingly large variations in the coefficients of the dynamic equations. Other factors also contribute to changes in the aircraft dynamics. The basic aerodynamic coefficients change with Mach number and as functions of the aerodynamic angles, and the mass properties change with different payloads and changing fuel load.

Because of the large changes in aircraft dynamics, a dynamic mode that is stable and adequately damped in one flight condition may become unstable, or at least inadequately damped, in another flight condition. A lightly damped oscillatory mode may cause a great deal of discomfort to passengers or make it difficult for the pilot to control the trajectory precisely. These problems are overcome by using feedback control to modify the aircraft dynamics. The aircraft motion variables are sensed and used to generate signals that can be fed into the aircraft control surface actuators, thus modifying the dynamic behavior. This feedback must be adjusted according to the flight condition. The adjustment process is called *gain scheduling* because, in its simplest form, it involves only changing the amount of feedback as a function of a "scheduling" variable. These scheduling variables will normally be measured dynamic pressure and/or Mach number.

In the case of low-performance aircraft with relatively narrow envelopes and control surfaces that are not power driven, an unsatisfactory dynamic mode must be corrected by modifying the basic design. As in the case of the high-performance aircraft, this requires an understanding of the dynamic modes and their dependence on the aerodynamic coefficients and aerodynamic derivatives.

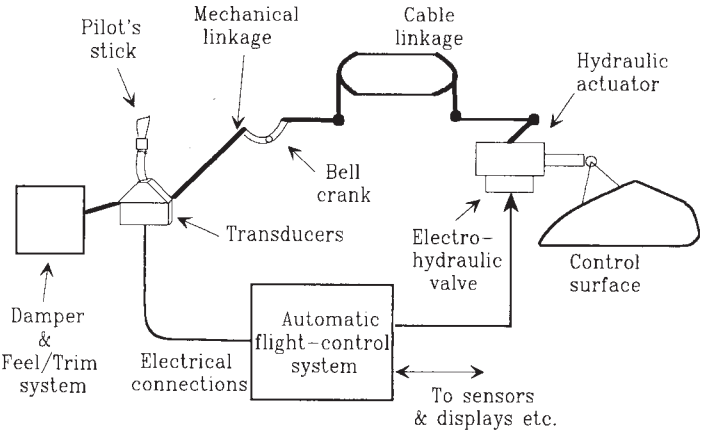

Figure 4.1-2 An electromechanical control system.

Figure 4.1-2 shows how a fully powered aircraft control system might be implemented with mechanical, hydraulic, and electrical components. Because the control surfaces are fully power driven, there is no force or motion feedback to the pilot's control stick. This is called an *irreversible* control system, and bob weights and springs (or electrical or hydraulic devices) must be added to the control stick to provide some "feel" to the pilot. The stick and rudder pedals are shown linked to the actuators by a combination of mechanical links and bell cranks and control wires. The control surfaces are driven by a hydraulic servomechanism that has a follow-up action; that is, the high-power output shaft is driven until its position corresponds to the position of the low-power input shaft.

Augmentation signals are conveniently added to the system of Figure 4.1-2 by electrical means. The signals from rate gyros (angular rate measuring devices), accelerometers, the air data computer, and other sources are processed by the flight control computer. The electrical output of the flight control computer (converted to analog form) is used to drive electrohydraulic valves, and these superimpose additional motion on the hydromechanical control system.

The Functions of the Automatic Control Systems

The descriptions and analyses of aircraft modes in Chapters 3 and 4 show that they can be divided into different categories. One category includes modes that involve mainly the rotational degrees of freedom; these are the short-period, roll, and dutch roll modes. Their natural frequencies (or time constants, if purely exponential) are determined by the moments of inertia of the aircraft and the moments generated by the aerodynamic surfaces; their damping is determined by the rate-dependent aerodynamic moments. The remaining modes (phugoid and spiral) involve changes in the flight path and are much slower modes. The phugoid mode involves the translational degrees of freedom and is dependent on the aerodynamic forces of lift and drag and

their variation with speed. The spiral mode depends on aerodynamic moments, but only weak aerodynamic forces are involved.

The responsiveness of an aircraft to maneuvering commands is determined in part by the speed of the rotational modes. The frequencies of these modes tend to be sufficiently high that a pilot would find it difficult or impossible to control the aircraft if the modes were lightly damped or unstable. Therefore, it is necessary to provide automatic control systems to give these modes suitable damping and natural frequencies. Such control systems are known as *stability augmentation systems* (SASs). If the augmentation system is intended to control the mode and to provide the pilot with a particular type of response to the control inputs, it is known as a *control augmentation system* (CAS). An example of this is a normal acceleration CAS, in which the pilot's inputs are intended to control the acceleration generated along the negative z-axis.

The slow modes (phugoid and spiral) are controllable by a pilot. But since it is undesirable for a pilot to have to pay continuous attention to controlling these modes, an automatic control system is needed to provide "pilot relief." An *autopilot* is an automatic control system that provides both pilot relief functions and special functions such as automatic landing.

The common types of SAS, CAS, and autopilot functions can be listed as follows:

SAS	CAS	Autopilots
Roll damper	Roll rate	Pitch-attitude hold
Pitch damper	Pitch rate	Altitude hold
Yaw damper	Normal acceleration	Speed/Mach hold
	Lateral/directional	Automatic landing
		Roll angle hold
		Turn coordination
		Heading hold/VOR hold

These control systems are described and illustrated by numerical examples in Sections 4.4 through 4.7.

4.2 AIRCRAFT RIGID-BODY MODES

In this section algebraic expressions for the rigid-body modes will be derived so that their dependence on the stability derivatives and on the flight conditions can be examined and conditions for stability can be deduced. When decoupling of the longitudinal and lateral-directional dynamics occurs ("lat-long" decoupling), it becomes feasible to manipulate the aircraft transformed state equations algebraically. Both the longitudinal and lateral-directional dynamics are still fourth order, so the modes are obtained from the roots of a fourth-order characteristic polynomial. Algebraic solution of a quartic equation is not practicable, but with some simplifying assumptions based on knowledge of the stability derivatives and the physics of flight, this problem can be bypassed.

Algebraic Derivation of Longitudinal Transfer Functions and Modes

The coefficient matrices for the decoupled longitudinal state equations are given in (2.6-29). The SISO transfer functions can be derived very easily by applying Cramer's rule to the Laplace transformed state equations as follows. The matrix $(sE - A)$ is given by

$$(sE-A)=\begin{bmatrix} s(V_{T_e}-Z_{\dot{\alpha}})-Z_{\alpha} & -(V_{T_e}+Z_q) & -Z_V+X_{T_V}\sin(\alpha_e+\alpha_T) & g_D\sin\gamma_e \\ -sM_{\dot{\alpha}}-M_{\alpha}-M_{T_{\alpha}} & s-M_q & -(M_V+M_{T_V}) & 0 \\ -X_{\alpha} & 0 & s-X_V-X_{T_V}\cos(\alpha_e+\alpha_T) & g_D\cos\gamma_e \\ 0 & -1 & 0 & s \end{bmatrix} \tag{4.2-1}$$

and the B-matrix is

$$B=\begin{bmatrix} Z_{\delta e} & -X_{\delta t}\sin\left(\alpha_e+\alpha_T\right) \\ M_{\delta e} & M_{\delta t} \\ X_{\delta e} & X_{\delta t}\cos(\alpha_e+\alpha_T) \\ 0 & 0 \end{bmatrix}$$

If, for example, the $q/\delta e$ transfer function is required, the δ_e column of B must be substituted for the q column of $|sE - A|$. The transfer function is

$$\frac{q}{\delta_e}=\frac{1}{|sE-A|}\begin{vmatrix} S(V_{T_e}-Z_{\dot{\alpha}})-Z_{\alpha} & Z_{\delta e} & -Z_V+X_{T_V}\sin(\alpha_e+\alpha_T) & g_D\sin\gamma_e \\ -sM_{\dot{\alpha}}-M_{\alpha}-M_{T\alpha} & M_{\delta e} & -(M_V+M_{T_V}) & 0 \\ -X_{\alpha} & X_{\delta e} & s-X_V-X_{T_V}\cos(\alpha_e+\alpha_T) & g_D\cos\gamma_e \\ 0 & 0 & 0 & s \end{vmatrix} \tag{4.2-2}$$

It is evident from inspection of the determinant that this transfer function is of the form

$$\frac{q(s)}{\delta_e(s)}=\frac{s(b_2s^2+b_1s+b_0)}{a_4s^4+a_3s^3+a_2s^2+a_1s+a_0} \tag{4.2-3}$$

Expressions for the numerator and denominator coefficients can be derived in a straightforward way by expanding the determinants. However, the coefficients are complicated functions of the dimensional derivatives and are tedious to evaluate without a digital computer. This is a feasible method of deriving transfer functions from the stability derivatives, but it relies on lat-long decoupling and provides very little insight. We will now examine various approximations that lead to transfer functions that are simple enough to provide some insight into the dynamic behavior.

Consider the decoupled longitudinal dynamics; a time-history simulation in Section 3.6 showed that it was possible to excite separately the short-period and phugoid modes. In the phugoid case speed and theta varied, with alpha and q almost constant; while in the short-period case alpha, q, and theta varied, with speed

constant. This implies additional decoupling in the dynamic equations that will now be investigated.

Returning to the longitudinal coefficient matrices (2.6-29), with state and control vectors

$$x = [\alpha \;\; q \;\; v_T \;\; \theta]^T \qquad u = [\delta_e \;\; \delta_t]^T \tag{4.2-4}$$

partition the state equations as

$$\begin{bmatrix} E_1 & 0 \\ 0 & I \end{bmatrix} \dot{x} = \begin{bmatrix} A_{11} & A_{12} \\ A_{21} & A_{22} \end{bmatrix} x + \begin{bmatrix} B_{11} & B_{12} \\ B_{21} & B_{22} \end{bmatrix} u, \tag{4.2-5}$$

with $E_1(2 \times 2)$, $A_{ij}(2 \times 2)$, and $B_{ij}(2 \times 1)$. Now if it is to be possible for v_T and θ to vary, without significant changes in α and q, the submatrix A_{12} must introduce very little coupling from the second set of equations into the first. An examination of the appropriate terms of the matrix $E^{-1}A$ in Example 3.7-2 shows that this is the case in that particular example. More generally, the a_{14} term is null when the flight-path angle is zero, and a_{24} is identically zero. The a_{23} term is insignificant when the tuck derivative and the thrust derivative M_{T_V} are negligible. The tuck derivative is negligible at low Mach numbers, and the thrust derivative is often negligible because the thrust vector passes close to the cg. When the a_{13} term is expanded in terms of dimensionless derivatives, components due to $2g_D/V_{T_e}$, C_{L_V}, and C_{T_V} are found. The gravity term is small at normal airspeeds, and the variation of lift coefficient with airspeed is negligible at low Mach numbers. The thrust derivative depends on the type of propulsion, but it is found to be multiplied by $\sin(\alpha_e + \alpha_T)$ and is then usually small under normal flight conditions. In summary, the conditions for decoupling in the A-matrix include small flight path angle, small angle of attack, and low Mach number.

If the control stick is held fixed and there are no feedback control systems operating, the input u is null and we can ignore the B-matrix. The eigenvalues of the A-matrix then yield *stick-fixed modes* of the aircraft. Here we will look for decoupling in the B-matrix and find a transfer function for the decoupled equations. The B_{12} block in (4.2-5) includes the variation of the thrust and pitching moment coefficients with throttle changes. The thrust coefficient term is multiplied by $\sin(\alpha_e + \alpha_T)$ and may often be neglected; the pitching moment term is negligible when the thrust vector passes close to the cm.

We will now neglect the A_{12} and B_{12} terms in (4.2-5) and extract the alpha and pitch-rate equations from the complete dynamics to obtain a short-period transfer function.

The Short-Period Approximation

The short-period approximation obtained from (4.2-5) is

$$\begin{bmatrix} V_{Te} - Z_{\dot{\alpha}} & 0 \\ -M_{\dot{\alpha}} & 1 \end{bmatrix} \begin{bmatrix} \dot{\alpha} \\ \dot{q} \end{bmatrix} = \begin{bmatrix} Z_\alpha & V_{Te} + Z_q \\ M_\alpha & M_q \end{bmatrix} \begin{bmatrix} \alpha \\ q \end{bmatrix} + \begin{bmatrix} Z_{\delta e} \\ M_{\delta e} \end{bmatrix} \delta_e, \tag{4.2-6}$$

where, for compactness, M_α will be assumed to include M_{T_α}. The transfer function matrix is given by

$$C(sE-A)^{-1}B = \frac{C}{\Delta_{sp}}\begin{bmatrix} \left(s-M_q\right)Z_{\delta e} + (V_{T_e}+Z_q)M_{\delta e} \\ (sM_{\dot\alpha}+M_\alpha)Z_{\delta e} + [s(V_{T_e}-Z_{\dot\alpha})-Z_\alpha]M_{\delta e}\end{bmatrix},$$

where C is the appropriate coupling matrix for α or q and Δ_{sp} is the short-period characteristic polynomial:

$$\begin{aligned}\Delta_{sp} = {} & (V_{T_e}-Z_{\dot\alpha})s^2 - [Z_\alpha + (V_{T_e}-Z_{\dot\alpha})M_q + (V_{T_e}+Z_q)M_{\dot\alpha}]s \\ & + M_qZ_\alpha - (V_{T_e}+Z_q)M_\alpha \end{aligned} \tag{4.2-7}$$

The individual transfer functions are

$$\frac{\alpha}{\delta_e} = \frac{Z_{\delta e}s + (V_{T_e}+Z_q)M_{\delta e} - M_qZ_{\delta e}}{\Delta_{sp}} \tag{4.2-8}$$

$$\frac{q}{\delta_e} = \frac{[(V_{T_e}-Z_{\dot\alpha})M_{\delta e} + Z_{\delta e}M_{\dot\alpha}]s + M_\alpha Z_{\delta e} - Z_\alpha M_{\delta e}}{\Delta_{sp}} \tag{4.2-9}$$

The short-period mode is normally complex, so comparing the denominator with the quadratic standard form (3.3-16) gives

$$\omega_{n_{sp}}^2 = \frac{M_qZ_\alpha - M_\alpha(V_{T_e}+Z_q)}{V_{T_e}-Z_{\dot\alpha}} \tag{4.2-10a}$$

$$-2\zeta_{sp}\omega_{n_{sp}} = M_q + \frac{M_{\dot\alpha}(V_{T_e}+Z_q)+Z_\alpha}{V_{T_e}-Z_{\dot\alpha}} \tag{4.2-10b}$$

The derivatives Z_q and $Z_{\dot\alpha}$ are normally small compared to V_{T_e} and will be dropped from these equations. Then, when the dimensionless derivatives are substituted and the approximation $C_D \ll C_{L_\alpha}$ is used, the results are

$$\omega_{n_{sp}}^2 = \frac{\overline{q}S\overline{c}}{J_y}\left[-C_{m_\alpha} - \frac{\rho S\overline{c}}{4\mathrm{m}}C_{m_q}C_{L_\alpha}\right] \tag{4.2-11}$$

$$\zeta_{sp} = \frac{1}{4\sqrt{2}}\left[\frac{(\rho S\overline{c})\,\overline{c}^2}{J_y}\right]^{1/2}\frac{\left[-C_{m_q} - C_{m_{\dot\alpha}} + \dfrac{2J_Y}{\mathrm{m}\overline{c}^2}C_{L_\alpha}\right]}{\left[-C_{m_\alpha} - \dfrac{\rho S\overline{c}}{4\mathrm{m}}C_{m_q}C_{L_\alpha}\right]^{1/2}} \tag{4.2-12}$$

In both equations the term $\rho S\overline{c}/4\mathrm{m}$ is a mass ratio, typically on the order of 0.001 and decreasing with altitude. However, $C_{m_q}C_{L_\alpha}$ may be quite large and so, compared to C_{m_α}, we may not be able to neglect this term. In the natural frequency formula these terms are multiplied by dynamic pressure so, without any assumptions about

the mass ratio term, we can say that the natural frequency is directly proportional to airspeed and tends to decrease with air density (i.e., with altitude).

The inertia ratio $2J_Y/m\bar{c}^2$ that occurs in the damping formula is equal to twice the square of the quantity: pitching radius of gyration over mean chord, which may be around unity. Therefore, it is difficult to say anything about a dominant term in the numerator, though we do expect the pitch damping derivative to be important. The inertia ratio $(\rho S\bar{c})\bar{c}^2/J_y$ will cause the damping ratio to *decrease as the square root of the air density* (unless the pitch stiffness is near zero, so that the density term in the denominator cancels this effect).

It must be emphasized again that the above results are only valid at low Mach numbers where the stability derivatives are reasonably constant. Also, the above analysis assumed a damped, oscillatory short-period mode; different behavior will be illustrated later.

The Phugoid Approximation

Approximations for the natural frequency and damping of the phugoid mode will be developed by extending the approach used to derive the short-period results. Refer again to (4.2-5) and assume that only the phugoid mode has been excited. If the derivatives $\dot{\alpha}$ and $\dot{q}$ are then neglected, the first pair of equations reduce to algebraic equations that act as a constraint on the remaining differential equations in the phugoid variables. Therefore, we have

$$0 = A_{11}\begin{bmatrix}\alpha\\ q\end{bmatrix} + A_{12}\begin{bmatrix}v_T\\ \theta\end{bmatrix}$$

$$\begin{bmatrix}\dot{v}_T\\ \dot{\theta}\end{bmatrix} = A_{21}\begin{bmatrix}\alpha\\ q\end{bmatrix} + A_{22}\begin{bmatrix}v_T\\ \theta\end{bmatrix}$$

When the algebraic equations are used to eliminate α and q from the differential equations, the following equations for the phugoid variables are obtained:

$$\begin{bmatrix}\dot{v}_T\\ \dot{\theta}\end{bmatrix} = (A_{22} - A_{21}A_{11}^{-1}A_{12})\begin{bmatrix}v_T\\ \theta\end{bmatrix} \tag{4.2-13}$$

In order to evaluate the coefficient matrix, we will make the usual assumption that $\gamma_e = 0$. This greatly simplifies the derivation, but as we will see later, γ has a significant effect on the phugoid mode. Equation (4.2-13) now becomes

$$\begin{bmatrix}\dot{v}_T\\ \dot{\theta}\end{bmatrix} = \begin{bmatrix} X'_V - \dfrac{X_\alpha\left[M_q(Z_V - X_{T_V}\sin(\alpha_e+\alpha_T)) - (V_{T_e}+Z_q)(M_V+M_{T_V})\right]}{\Delta_p} & -g_D \\ \dfrac{M_\alpha(Z_V - X_{T_V}\sin(\alpha_e+\alpha_T)) - Z_\alpha(M_V+M_{T_V})}{\Delta_p} & 0 \end{bmatrix}\begin{bmatrix}v_T\\ \theta\end{bmatrix} \tag{4.2-14}$$

where

$$X'_V = X_V + X_{T_V}\cos(\alpha_e + \alpha_T)$$
$$\Delta_p = M_q Z_\alpha - M_\alpha(V_{T_e} + Z_q)$$

The characteristic equation can now be found from $|sI - A|$, and a comparison with the quadratic standard form gives the following expressions for the phugoid natural frequency and damping:

$$\omega_{n_P}^2 = g_D \frac{M_\alpha(Z_V - X_{T_V}\sin(\alpha_e + \alpha_T)) - Z_\alpha(M_V + M_{T_V})}{M_q Z_\alpha - M_\alpha(V_{T_e} + Z_q)} \tag{4.2-15a}$$

$$2\zeta_P\omega_{n_P} = -X'_V + \frac{X_\alpha[M_q(Z_V - X_{T_V}\sin(\alpha_e + \alpha_T)) - (V_{T_e} + Z_q)(M_V + M_{T_V})]}{M_q Z_\alpha - M_\alpha(V_{T_e} + Z_q)} \tag{4.2-15b}$$

These expressions are considerably more complicated than those for the short-period mode; nevertheless, some conclusions can be drawn from them.

Consider the expression for the phugoid frequency, and for simplicity neglect the thrust derivatives and Z_q. Then insert dimensionless derivatives, with $C_{m_e} = 0$ and $C_{D_e} \ll C_{L_\alpha}$; the result is

$$\omega_{np}^2 = \frac{2g_D}{\overline{c}} \frac{C_{m_\alpha}(2C_{L_e} + C_{L_V}) - C_{L_\alpha}C_{m_V}}{C_{m_q}C_{L_\alpha} + \dfrac{4\mathrm{m}}{\rho S\overline{c}}C_{m_\alpha}} \tag{4.2-16}$$

This is the equation that will be used to calculate the phugoid frequency, but the variation with flight conditions can be illustrated as follows. The numerator contains the compressibility effects C_{L_V} and C_{m_V} and the equilibrium lift C_{L_e}. The denominator is the same as the square-bracket term in the short-period equation (4.2-11), except that the whole expression is now multiplied by $4\mathrm{m}/(\rho S\overline{c})$, $(\approx 10^3)$. If the mass ratio times pitch stiffness does dominate the denominator, and if we also neglect the compressibility terms in the numerator, we get a very simple expression for the phugoid frequency:

$$\omega_{n_p}^2 \approx \frac{2g_D}{\overline{c}}\frac{\rho S\overline{c}}{4\mathrm{m}}(2C_{Le}) = \frac{2g_D^2}{V_{T_e}^2}\frac{\overline{q}SC_{Le}}{\mathrm{m}g_D} \tag{4.2-17a}$$

In level flight, with a small angle of attack, the lift is approximately equal to the weight, and this equation reduces to

$$\omega_{n_P} \approx \frac{g_D}{V_T}\sqrt{2} \tag{4.2-17b}$$

Therefore, phugoid frequency is inversely proportional to airspeed, other things being equal. For a given speed, at higher altitude, alpha will be bigger and so the thrust will

provide a larger component of the total vertical force, and a smaller aerodynamic lift component will be needed. Therefore, according to (4.2-17*a*), the frequency will be lower at higher altitude. The result given in Equation (4.2-17*b*) was found by F. W. Lanchester in 1908 and can be derived for large-amplitude motion from energy considerations.

It is more difficult to derive simple expressions for the damping of the phugoid and, furthermore, in the next subsection, the damping equation (4.2-15*b*) is shown to be quite inaccurate. Nevertheless it is still worthwhile to examine this equation to understand what factors influence the phugoid damping. The second term in the equation is often much smaller than the first, and analyzing only the first term gives

$$2\zeta_p\omega_{n_p} \approx -[X_V + X_{T_V}\cos(\alpha_e + \alpha_T)]$$

The dimensional derivatives on the right-hand side contain the equilibrium values of drag and thrust, and we will substitute the steady-state condition (2.4-1*a*) for these quantities, thus

$$2\zeta_p\omega_{n_p} \approx \frac{-2g_D \sin\gamma_e}{V_{T_e}} + \frac{\overline{q}S}{\mathrm{m}V_{T_e}}[C_{D_V} - C_{T_V}\cos(\alpha_e + \alpha_T)]$$

Now consider the level flight case; use (4.2-17*a*) to substitute for ω_{n_p} and equate lift to weight,

$$\zeta_p = \frac{1}{2\sqrt{2}}\frac{[C_{D_V} - C_{T_V}\cos(\alpha_e + \alpha_T)]}{C_{L_e}} \tag{4.2-18}$$

The phugoid mode involves changes in speed, and this equation shows that the damping depends on the changes in drag and thrust with speed. The speed damping derivative C_{D_V} is small until the transonic drag rise begins and then usually negative in the supersonic regime. Therefore, (4.2-18) indicates the possibility of an unstable phugoid (negative damping) in the supersonic regime, depending on the way in which thrust varies with Mach. Roskam (1979) provides (approximate) comparative analyses of the derivative C_{T_V} for jets, propeller aircraft, rocket aircraft, and unpowered aircraft. However, we should remember that even Equation (4.2-15*b*) does not necessarily give very accurate results for the phugoid damping. More accurate numerical results given in the next subsection show that at subsonic speeds *the phugoid damping ratio increases with airspeed and decreases with altitude*. Example 4.2-2 shows, in addition, that the damping decreases rapidly with flight-path angle.

Accuracy of the Short-Period and Phugoid Approximations

The short-period approximation almost always gives a good approximation for the α and q response to elevator inputs with constant throttle setting, and it will play an important role in the numerical designs in this chapter. The phugoid approximation usually gives good accuracy for the period of the phugoid oscillation but not for the damping ratio. These facts are borne out by the transport aircraft model.

The dimensional-derivative evaluation program used in Example 3.7-1 was extended to calculate the short-period and phugoid properties from (4.2-7) and (4.2-14), respectively. Thus, the characteristic roots (or the frequencies and damping ratios) could be calculated for the transport aircraft from any given set of steady-state flight conditions. The program also calculated the matrix $E^{-1}A$ (as used in Example 3.7-1) so that "exact" dynamic modes could be obtained from this matrix using an eigenvalue program. The flight conditions were level flight at sea level, with different airspeeds and cg positions. Table 4.2-1 shows the results of these calculations. An asterisk in the table indicates characteristic roots instead of period and damping ratio.

The first three sets of entries show the effect of varying airspeed; the last four sets show the effect of moving the cg position further aft with speed held constant. The short-period approximation is seen to be a very good approximation for the first five cases. The phugoid approximation gives accurate results for the period; the damping ratio is quite inaccurate but the accuracy appears to improve when the period is large. Note that the phugoid mode is unstable at low airspeed (200 ft/s).

When the cg is moved aft, the short-period roots move onto the real axis, and then one real root moves toward the phugoid roots. The short-period and phugoid approximations break down and one real root moves into the right-half plane. At the same time a new oscillatory mode appears that has a phugoid-like period with a short-period damping ratio. This mode is sometimes known as the *third oscillatory mode*, and it is characteristic of a statically unstable airplane. Also, the fact that one real root becomes unstable signals an exponential instability in pitch (a pitch "departure") rather than an oscillatory instability. This is the kind of instability that might be intuitively associated with the loss of positive pitch stiffness.

TABLE 4.2-1 Accuracy of Short-Period and Phugoid Formulas

Airspeed/cg		Calculation	T_{SP}	ζ_{SP}	T_P	ζ_P
200,	0.25	Approximate	7.44	0.555	32.3	0.102
		Exact	7.33	0.565	32.7	−0.0129
400,	0.25	Approximate	3.73	0.551	63.5	0.064
		Exact	3.72	0.551	63.6	0.035
600,	0.25	Approximate	2.48	0.551	96.5	0.112
		Exact	2.48	0.551	96.6	0.099
400,	0.30	Approximate	4.04	0.598	65.4	0.067
		Exact	4.04	0.524	65.5	0.033
400,	0.40	Approximate	5.04	0.744	74.1	0.083
		Exact	5.02	0.652	74.3	0.036
400,	0.50	Approximate	$(-0.523,$	$-1.33)^*$	476	0.691
		Exact	$(-0.810 \pm j0.200)^*$		476	0.630
400,	0.55	Approximate	$(-1.70,$	$-0.158,$	$-0.158,$	$0.128)^*$
		Exact	$(-1.44,$	$0.100,$	$-0.150 \pm j0.123)^*$	

In the example, the stability boundary for the aft-cg location occurs when the cg lies between $0.501\,\overline{c}$ and $0.502\,\overline{c}$. It is evident that the characteristic equation of the short-period approximation cannot be used as an accurate means of calculating this cg position. However, the condition for a single real root to move into the right-half plane can be derived quite easily from the complete longitudinal dynamics, as we now show.

Pitch Stability

Sections 2.2 and 2.4 described the concept of positive pitch stiffness and pointed out that positive stiffness was not sufficient to guarantee stability of the longitudinal motion. The stability of the longitudinal motion will now be investigated by means of a dynamic analysis.

The characteristic polynomial of the decoupled longitudinal dynamics can be obtained from the determinant $|sE - A|$, with the E- and A-matrices as given in (2.6-29). The constant term in the characteristic polynomial is equal to the product of the roots, and therefore the constant term will vanish when a real root reaches the origin, as the pitch-stability limit is reached. This constant term is obtained by putting $s = 0$ in $|sE - A|$, and therefore the stability boundary is given by $|A| = 0$. If the determinant obtained from (2.6-29) is expanded about the (4, 2) element, with $\gamma_e = 0$, the result is

$$0 = |A| = \begin{vmatrix} Z_\alpha Z_V - X_{T_V} \sin\left(\alpha_e + \alpha_T\right) & 0 \\ M_\alpha + M_{T_\alpha} M_V + M_{T_V} & 0 \\ X_\alpha X_V + X_{T_V} \cos(\alpha_e + \alpha_T) & -\mathrm{g_D} \end{vmatrix}$$

$$= -g_D \begin{vmatrix} Z_\alpha Z_V & -X_{T_V} \sin\left(\alpha_e + \alpha_T\right) \\ M_\alpha + M_{T_\alpha} & M_V + M_{T_V} \end{vmatrix}$$

or

$$Z_\alpha(M_V + M_{T_V}) - (M_\alpha + M_{T_\alpha})(Z_V - X_{T_V} \sin(\alpha_e + \alpha_T)) = 0$$

When the dimensionless derivatives are substituted into this equation, the factors $(\overline{q}S/\mathrm{m})$, $(\overline{q}S\overline{c}/J_y)$, and $(1/V_{T_e})$ are removed, and the equilibrium condition $(C_{M_e} + C_{M_{T_e}}) = 0$ is applied, the stability boundary becomes

$$(C_{D_e} + C_{L_\alpha})(C_{m_V} + C_{m_{T_V}}) - (C_{m_\alpha} + C_{m_{T_\alpha}})[2C_{L_e} + C_{L_V} + (2C_{T_e} + C_{T_V}) \sin(\alpha_e + \alpha_T)] = 0$$

This equation can be simplified by using (2.4-1b) to get the following relationship for steady-state level flight:

$$2C_{T_e} \sin(\alpha_e + \alpha_T) + 2C_{L_e} = 2\mathrm{m}g_D/(\overline{q}S) \equiv 2C_{W_e},$$

where $C_W(\approx C_L)$ is the aircraft weight made dimensionless in the usual way. Substituting this result into the stability boundary condition, we get

$$(C_{D_e} + C_{L_\alpha})(C_{m_V} + C_{m_{T_V}}) - (C_{m_\alpha} + C_{m_{T_\alpha}})[2C_{W_e} + C_{L_V} + C_{T_V}\sin(\alpha_e + \alpha_T)] = 0$$

To further simplify the expression, neglect the drag coefficient compared to the lift-curve slope, and let the thrust and aerodynamic moment derivatives be included in a single derivative. Then,

$$0 = C_{L_\alpha} C_{m_V} - C_{m_\alpha}[2C_{W_e} + C_{L_V} + C_{T_V}\sin(\alpha_e + \alpha_T)] \tag{4.2-19}$$

This condition still holds when the last two terms on the right are negligible and, knowing that C_{W_e} and C_{L_α} are always positive, we can deduce that the condition for pitch stability is

$$C_{m_\alpha} < \frac{C_{L_\alpha} C_{m_V}}{2C_{W_e} + C_{L_V} + C_{T_V}\sin(\alpha_e + \alpha_T)} \tag{4.2-20}$$

When the tuck derivative is zero, (4.2-20) reduces to the static stability condition [see, for example, (2.4-19)]. When the aircraft has an unstable tuck ($C_{m_V} < 0$) at high subsonic Mach numbers, a greater low-speed static margin is required to maintain pitch stability at those Mach numbers. Roskam (1979) points out that the pitch divergence of most subsonic jet transports is rather slow and not necessarily objectionable.

Algebraic Derivation of Lateral-Directional Transfer Functions

The lateral-directional coefficient matrices are given by (2.6-31). We will eliminate the E-matrix by dividing the first lateral equation by V_{T_e}; the characteristic polynomial is then

$$|sI - A| = \begin{vmatrix} s - \dfrac{Y_\beta}{V_{T_e}} & \dfrac{-g_D\cos\theta_e}{V_{T_e}} & \dfrac{-Y_p}{V_{T_e}} & 1 - \dfrac{Y_r}{V_{T_e}} \\ 0 & s & -c\gamma_e/c\theta_e & -s\gamma_e/c\theta_e \\ -L'_\beta & 0 & s - L'_p & -L'_r \\ -N'_\beta & 0 & -N'_p & s - N'_r \end{vmatrix} \tag{4.2-21}$$

and the B-matrix is

$$B = \begin{bmatrix} \dfrac{Y_{\delta a}}{V_{T_e}} & \dfrac{Y_{\delta r}}{V_{T_e}} \\ 0 & 0 \\ L'_{\delta a} & L'_{\delta r} \\ N'_{\delta a} & N'_{\delta r} \end{bmatrix} \tag{4.2-22}$$

Cramer's rule can now be used to find any particular transfer function. It is usual to make the lateral-directional equations manageable by assuming level flight ($\gamma_e = 0$). Then, for example, the aileron-to-roll-rate transfer function is

$$\frac{p(s)}{\delta_a(s)} = \frac{1}{|sI - A|} \begin{vmatrix} s - \dfrac{Y_\beta}{V_{T_e}} & \dfrac{-g_D \cos\theta_e}{V_{T_e}} & \dfrac{Y_{\delta a}}{V_{T_e}} & 1 - \dfrac{Y_r}{V_{T_e}} \\ 0 & s & 0 & 0 \\ -L'_\beta & 0 & L'_{\delta a} & -L'_r \\ -N'_\beta & 0 & N'_{\delta a} & s - N'_r \end{vmatrix}, \tag{4.2-23}$$

which is of the form

$$\frac{p(s)}{\delta_a(s)} = \frac{ks(s^2 + 2\zeta_\phi \omega_\phi s + \omega_\phi^2)}{a_4 s^4 + a_3 s^3 + a_2 s^2 + a_1 s + a_0} \tag{4.2-24}$$

The subscript ϕ has been used on the numerator quadratic because the same factor appears in the roll angle transfer function, and the notation is in common use.

Once again, the polynomial coefficients are complicated functions of the dimensional derivatives, but some simplifications are possible. If the sideforce and yawing effects of the ailerons are neglected (i.e., neglect $Y_{\delta a}/V_{T_e}$ and $N'_{\delta a}$), the determinant in (4.2-23) has a simple expansion about the third column. Then assuming that $Y_r/V_{T_e} \ll 1.0$, the numerator of (4.2-24) can be written as

$$ks(s^2 + 2\zeta_\phi \omega_\phi s + \omega_\phi^2) = sL'_{\delta a}[s^2 - s(N'_r + Y_\beta/V_{T_e}) + (N'_\beta + Y_\beta N'_r/V_{T_e})] \tag{4.2-25}$$

When the aircraft has negligible *roll-yaw coupling*, the quadratic factor on the right-hand side of (4.2-25) also appears in the lateral-directional characteristic polynomial. This is shown in the next subsection. The resulting cancellation leaves a particularly simple expression for the aileron-to-roll-rate transfer function.

The lateral-directional characteristic equation does not separate into factors that clearly define each mode. Approximations will be derived that may describe an individual mode reasonably well, but they must be checked for applicability in any given case. Nevertheless, these approximations do provide useful insight into the dynamic behavior, and they will be derived for this reason. We start with the dutch roll approximation.

The Dutch Roll Approximation

The dihedral derivative C_{l_β} determines the amount of rolling in the dutch roll mode, and when this derivative is small, the mode will consist mainly of sideslipping and yawing. The dihedral derivative tends to be large in modern swept-wing aircraft and so it will be neglected only for the purpose of deriving the traditional "3-DoF dutch roll approximation." A more modern approximation will then be given.

The coefficient of the roll angle in the beta-dot equation is the gravity term in the characteristic determinant (4.2-21). When this element is neglected, the determinant has a simple reduction about the second column. The reduction of the subsequent third-order determinant can be further simplified if the terms Y_p/V_{T_e} and Y_r/V_{T_e} can be dropped (Y_p is often zero, and $Y_r/V_{T_e} \ll 1.0$). The cross-derivative term N'_p (yawing moment due to roll rate) is also often negligible. The dihedral derivative then no longer appears in the characteristic polynomial, which is given by

$$|sI - A| = s(s - L'_p)[s^2 - s(N'_r + Y_\beta/V_{T_e}) + (N'_\beta + Y_\beta N'_r/V_{T_e})] \tag{4.2-26}$$

This polynomial has a root at the origin and at $s = L'_p$, which respectively approximate the spiral pole and the roll subsidence pole. The quadratic factor contains the dutch roll poles, and it exactly matches the numerator quadratic of the roll-rate transfer function (4.2-25). Therefore, an approximation to the aileron-to-roll-rate transfer function (4.2-24) is given by

$$\frac{p(s)}{\delta_a(s)} = \frac{L'_{\delta a}}{(s - L'_p)} \tag{4.2-27}$$

Equation (4.2-26) gives the dutch roll approximations as

$$\begin{aligned} \omega^2_{n_d} &= N'_\beta + (Y_\beta/V_{T_e})N'_r \\ \zeta_d &= -(N'_r + Y_\beta/V_{T_e})/(2\omega_{n_d}) \end{aligned} \tag{4.2-28a}$$

A more recent approximation (Ananthkrishnan and Unnikrishnan, 2001) is

$$\omega^2_{n_d} = N'_\beta + \frac{Y_\beta}{V_{T_e}}N'_r + \frac{g_D}{V_{T_e}}\frac{L'_\beta}{L'_p} - \left(L'_\beta + \frac{Y_\beta}{V_{T_e}}L'_r\right)\frac{N'_p}{L'_p}, \tag{4.2-28b}$$

whose first two terms agree with (4.2-28*a*). The damping equation in (4.2-28*a*) is unchanged, and so improved accuracy in the damping calculation will only come via the more accurate natural frequency.

We will now substitute dimensionless stability derivatives into the traditional dutch roll formulas and examine the dependence on flight conditions. The derivative N'_β is given by

$$N'_\beta = \frac{N_\beta + (J'_{XZ}/J'_Z)L_\beta}{1 - J'^2_{XZ}/(J'_X J'_Z)} \tag{4.2-29}$$

The stability-axes cross-product of inertia J'_{XZ} varies rapidly with the equilibrium angle of attack, typically changing from a small positive value at low alpha to a much larger negative value at high alpha. This larger value is still relatively small compared to J'_Z, so the primed derivatives are normally quite close to their unprimed values. It is possible for N_β to decrease and even change sign at high alpha, but then the linear equations are unlikely to be valid.

If we simply use the unprimed derivative N_β in the formula for the dutch roll frequency and then substitute the dimensionless derivatives, we obtain

$$\omega_{n_d}^2 = \frac{\overline{q}Sb}{J_z'}\left[C_{n_\beta} + \frac{\rho Sb}{4\mathrm{m}} C_{Y_\beta} C_{n_r}\right] \tag{4.2-30}$$

The C_{n_r} term is usually negligible compared to C_{n_β}, and this equation shows that the dutch roll frequency is proportional to the square root of dynamic pressure, assuming constant C_{n_β}. Therefore, at constant altitude, the *frequency increases in proportion to the airspeed*, and for a given speed the *frequency decreases with altitude*.

When unprimed derivatives are substituted into the damping formula, followed by dimensionless derivatives and the natural frequency expression from (4.2-28*a*), the damping ratio is given by

$$\zeta_d = -\frac{1}{4}\left[\frac{(\rho Sb)\, b^2}{2J_z'}\right]^{1/2} \frac{C_{n_r} + (2J_Z'/\mathrm{m}b^2)C_{Y_\beta}}{[C_{n_\beta} + (\rho Sb/4\mathrm{m})C_{n_r} C_{Y_\beta}]^{1/2}} \tag{4.2-31}$$

This expression indicates that the dutch roll damping is independent of dynamic pressure. *It will be proportional to the square root of density* since the second term of the denominator is usually negligible.

The dutch roll natural frequency formula tends to be quite accurate if the dihedral derivative is small, although the damping formula is not. This is illustrated in Example 4.2-1. Finally, note that the approximation to the roll subsidence pole, $s = L_p'$, is not very accurate, and a more accurate approximation will be derived next.

The Spiral and Roll Subsidence Approximations

The rolling and spiral modes usually involve very little sideslip. The rolling mode is almost pure rolling motion around the x-stability axis, and the spiral mode consists of yawing motion with some roll. It is common for the spiral mode to be unstable, and the motion then consists of increasing yaw and roll angles in a tightening downward spiral.

These facts allow approximations to be devised by modifying the $\dot{\beta}$ equation and leaving the moment equations unchanged. Sideforce due to sideslip is eliminated from the equation, $\dot{\beta}$ is neglected, and the gravity force is balanced against the force component associated with yaw rate. Thus, in the characteristic determinant (4.2-21) the term $s - Y_\beta/V_{T_c}$ is eliminated, and the Y_p/V_{T_e} term is again neglected. Because the gravity force is intimately involved in the spiral mode, the mode is dependent on flight-path angle. Unfortunately, the assumption of level flight is needed to allow a reasonably simple analysis and will therefore be used here. The effect of flight-path angle will be investigated numerically in Example 4.2-2. When the simplified determinant is expanded, the following second-order characteristic equation is obtained:

$$N_\beta' s^2 + (L_\beta' N_p' - L_p' N_\beta' - L_\beta' g_D/V_{T_e})s + (L_\beta' N_r' - N_\beta' L_r')g_D/V_{T_e} = 0 \tag{4.2-32}$$

The roots of this quadratic equation are usually real, stable, and widely separated because the spiral pole is very much closer to the origin than the roll pole. Therefore, the sum of the roots (given by the negative of the coefficient of s when the quadratic is made monic) is approximately equal to the reciprocal of the roll time constant τ_R,

$$\tau_R \approx \frac{N'_\beta}{L'_\beta N'_p - L'_p N'_\beta - L'_\beta g_D / V_{T_e}} \tag{4.2-33}$$

The quadratic constant term (i.e., the product of the roots) divided by the roll root gives the reciprocal of the spiral time constant τ_S,

$$\tau_S \approx \frac{L'_\beta N'_p - L'_p N'_\beta - L'_\beta g_D / V_{T_e}}{(L'_\beta N'_r - N'_\beta L'_r) g_D / V_{T_e}} \tag{4.2-34}$$

Note that a negative value for the time constant will simply mean an unstable exponential mode. A slightly more accurate formula for τ_s is given by Ananthkrishnan and Unnikrishnan (2001), but the difference is usually negligible. In the denominator of the roll time constant equation, the first term contains cross-derivatives and is usually negligible; the second term usually dominates the third, and under these conditions,

$$\tau_R \approx \frac{1}{L'_p} = -\frac{b}{V_T} \frac{4J'_X}{(\rho S b) b^2} \frac{1}{C_{\ell_p}} \text{ secs.} \tag{4.2-35}$$

This equation indicates that *the roll time constant will vary inversely as the product of density and speed*, given the above approximations, and a constant roll damping derivative.

The numerator of the spiral equation is the same as the denominator of the roll equation, and making the same approximation as above,

$$\tau_S \approx \frac{-L'_p N'_\beta}{(L'_\beta N'_r - L'_r N'_\beta)} = \frac{-C_{\ell_P} C_{n_\beta}}{(C_{\ell_\beta} C_{n_r} - C_{\ell_r} C_{n_\beta})} \frac{V_{T_e}}{g_D} \tag{4.2-36}$$

This equation indicates that the spiral time constant is proportional to speed, given the earlier approximations, and that the stability derivatives remain constant.

Spiral Stability

The condition for a pole at the origin is given by $|A| = 0$, and in the case of the lateral dynamics this normally represents the spiral pole becoming neutrally stable. From the characteristic determinant (4.2-21), we obtain

$$|A| = \begin{vmatrix} \frac{Y_\beta}{V_{T_e}} & \frac{(g_D \cos\theta_e)}{V_{T_e}} & \frac{Y_p}{V_{T_e}} & -1 + \frac{Y_r}{V_{T_e}} \\ 0 & 0 & c\gamma_e / c\theta_e & s\gamma_e / c\theta_e \\ L'_\beta & 0 & L'_p & L'_r \\ N'_\beta & 0 & N'_p & N'_r \end{vmatrix}$$

When the determinant is expanded, the spiral stability boundary is found to be given by

$$(L'_\beta N'_r - N'_\beta L'_r)\cos\gamma_e + (L'_p N'_\beta - L'_\beta N'_p)\sin\gamma_e = 0 \qquad (4.2\text{-}37)$$

This equation shows that spiral stability is dependent on flight-path angle, as noted earlier.

Accuracy of the Lateral-Mode Approximations

The accuracy of the lateral-mode formulas is often quite good apart from the dutch roll damping. The spiral time constant is also accurately predicted when this mode is unstable. This accuracy will be demonstrated in the following example using a model of a business jet in a cruising flight condition.

Example 4.2-1: Lateral Modes of a Business Jet The following lateral-directional data for a business jet are taken from Roskam (1979).

Flight Condition:
$W = 13{,}000$ lb, $g = 32.17$, $h = 40{,}000$ ft ($\rho = 0.000588$ slug/ft^3)
$V_T = 675$ ft/s, $\gamma = 0$ deg, $\alpha = 2.7$ deg
$J_x = 28{,}000$; $J_z = 47{,}000$; $J_{xz} = 1{,}350$ slug-ft^2 (body axes)

Geometrical Data: $S = 232$ ft^2, $b = 34.2$ ft

Stability Derivatives:
$C_{y_\beta} = -0.730$, $C_{y_p} = 0$, $C_{y_r} = +0.400$
$C_{l_\beta} = -0.110$, $C_{l_p} = -0.453$, $C_{l_r} = +0.163$
$C_{n_\beta} = +0.127$, $C_{n_p} = +0.008$, $C_{n_r} = -0.201$

A short program was written to convert the moments of inertia to stability axes, calculate the elements of the decoupled A-matrix, and evaluate the approximate equations for the modal characteristics [from (4.2-28a) and (4.2-32)–(4.2-34)]. Some intermediate results are:

Stability-Axes Moments of Inertia:
$J'_X = 27{,}915$ $J'_Z = 47{,}085$ $J'_{XZ} = 450.0$

Dimensional Derivatives:
$Y_\beta = -56.14$, $Y_p = 0$, $Y_r = 0.7793$
$L_\beta = -4.188$, $L_p = -0.4369$, $L_r = 0.1572$
$N_\beta = 2.867$, $N_p = 0.004575$, $N_r = -0.1149$

Primed Dimensional Derivatives:

$L'_\beta = -4.143;\ \ L'_p = -0.4369;\ \ L'_r = 0.1554$

$N'_\beta = 2.827;\ \ N'_p = 0.0003991;\ \ N'_r = -0.1135$

The full A-matrix was calculated from (4.2-21) so that an eigenvalue program could be used to determine the modes "exactly." The exact and approximate results are as follows:

Dutch Roll Mode:

Exact: $\omega_n = 1.689\,\text{rad/s},\ \ \zeta = 0.03878$

Equations (4.2-28a): $\omega_n = 1.684\,\text{rad/s},\ \ \zeta = 0.05837$

Roll Subsidence Mode:

Exact: $\tau_R = 1.994$

Equation (4.2-32): $\tau_R = 1.980$

Equation (4.2-33): $\tau_R = 1.976$

Spiral Mode:

Exact: $\tau_S = 978.4$

Equation (4.2-32): $\tau_S = 976.7$

Equation (4.2-33): $\tau_S = 978.6$

These results are in remarkably good agreement, apart from the dutch roll damping. ■

Mode Variation from the Nonlinear Model

It is not very realistic to use a fixed set of stability derivatives to show the variation of the modal characteristics with flight conditions. Therefore, as a final example we will use the completely numerical approach to calculate the modes of the nonlinear F-16 model at different flight conditions. The modes will only be calculated accurately since the numerical linearization is set up to produce the state equation coefficient matrices, not the stability derivatives. The variation of the modes with flight-path angle will also be determined, since this could not easily be done with the approximate formulas.

Example 4.2-2: Mode Dependence from the Nonlinear Model The nonlinear F-16 model allows a realistic examination of the dependence of the modes on flight conditions, since it is not built from a fixed set of aerodynamic derivatives. The following results were obtained by trimming and numerically linearizing the model at the desired flight condition and then using an eigenvalue program to determine the modes

TABLE 4.2-2 Effect of Flight-Path Angle on F-16 Modes

γ	−5	0	5	10	15	20	deg
T_D	1.934	1.933	1.934	1.937	1.941	1.946	s
ζ_D	0.1346	0.1353	0.1360	0.1366	0.1371	0.1375	
τ_S	55.33	77.91	133.0	461.9	−312.3	−117.0	s
τ_R	0.2777	0.2777	0.2775	0.2772	0.2766	0.2760	s
T_{SP}	3.281	3.277	3.273	3.269	3.266	3.262	s
ζ_{SP}	0.6277	0.6279	0.6281	0.6282	0.6283	0.6283	
T_P	79.60	80.05	80.93	82.39	84.36	86.82	s
ζ_P	0.1297	0.09751	0.06557	0.03396	0.00227	−0.0298	

from the full thirteen-state A-matrix. Virtually identical results could be obtained by using the decoupled lat-long matrices.

The effect of flight-path angle was investigated by trimming the model according to the second set of conditions in Table 3.6-3 (502 ft/s, $h = 0$ ft, cg $= 0.3\,\overline{c}$) but with different values of γ. The modes are shown in Table 4.2-2. It is evident from these results that the "rotational" modes are almost independent of γ. Weak but consistent trends are visible in the dutch roll and roll subsidence modes and in the short period. Overall, the properties of the rotational modes are remarkably constant, considering the nature of the tabular aerodynamic data and the numerical processing (trimming and linearization) required to obtain them. The "flight-path" modes, phugoid and spiral, are strongly influenced by the flight-path angle. The spiral time constant initially increases as the flight-path angle increases, becomes infinite as the stability boundary is approached, and then decreases with flight-path angle when the mode is unstable. The phugoid period is only weakly affected by γ but increases as γ increases. Phugoid damping is more strongly affected; it decreases with increasing γ and the phugoid becomes unstable at a quite modest flight-path angle.

In Table 4.2-3 the model is trimmed in level flight with various combinations of speed and altitude to illustrate the effect of these two variables on the modes. The cg position is again at $0.3\,\overline{c}$. The flight conditions have been chosen to compare different speeds at the same altitude, the same speed at different altitudes, high and low dynamic pressures at the same altitude, and the same dynamic pressure at two greatly different altitudes. The first trim condition (50,000 ft, 900 ft/s) corresponds to 0.93 Mach and is therefore strictly outside the valid Mach range of the model; this is also true to a lesser extent for the third case (0.81 Mach). We do not have a model that includes compressibility effects, and we will simply consider this example as illustrating the variation of the modes when compressibility is not important. The second trim condition (50,000 ft, 600 ft/s) corresponds to full throttle, while the first case (higher speed) corresponds to only 0.765 throttle. Therefore, a dive-and-climb maneuver would be needed to get from the second to the first flight condition. The longitudinal dynamics are unstable in the second case. In the fourth flight condition trial-and-error adjustment of the speed was used to make the dynamic pressure the same as the first case.

TABLE 4.2-3 Effect of Speed and Altitude on F-16 Modes

Altitude/speed (dyn. pres)	50k, 900 (160)	50k, 600 (71)	0, 900 (963)	0, 367 (160)	ft, ft/s lb/ft^2
T_D	2.365	2.735	1.143	2.396	s
ζ_D	0.06480	0.07722	0.1272	0.1470	
τ_S	179.2	138.7	122.1	73.52	s
τ_R	1.050	2.230	0.1487	0.4160	s
T_{SP}	4.507	u/s	2.372	4.023	s
ζ_{SP}	0.2615	u/s	0.8175	0.5735	
T_P	102.1	u/s	183.4	56.93	s
ζ_P	0.005453	u/s	0.3242	0.06240	

The tabulated results show that, as expected, the dutch roll has almost the same period at two widely different speed-altitude combinations with the same dynamic pressure. They also show the expected increase in period with altitude (at constant speed) and the decrease in period with airspeed (at constant altitude). The dutch roll damping does tend to be independent of dynamic pressure and to decrease with altitude, as predicted by the theory.

The spiral time constant is expected to vary directly with V_T if the third numerator term in (4.2-36) is negligible and to vary as $V_T/\overline{q}$ if that term is dominant. The results indicate that the actual variation is somewhere in between these two trends. This is not unexpected because the F-16 has swept wings, and C_{l_β} can be expected to play a significant part in (4.2-36).

The time constant of the roll subsidence mode is approximately proportional to $V_T/\overline{q}$, as predicted. The short-period mode also shows the expected trends; the period is roughly the same at the two equal dynamic pressure conditions and is much smaller at the high dynamic pressure condition. As predicted, the damping is much more strongly affected by altitude than by dynamic pressure.

In the case of the phugoid period the two sea-level results show that the sixfold increase in dynamic pressure causes an increase in the period of 3.2 times (compared to the prediction of $\sqrt{6}$). At constant dynamic pressure the period increases with altitude, as expected. The phugoid damping also shows the expected trend, increasing with airspeed and decreasing with altitude. ■

4.3 THE HANDLING QUALITIES REQUIREMENTS

Background

Control law design can only be performed satisfactorily if a set of design requirements or performance criteria is available. In the case of control systems for piloted aircraft, generally applicable quantitative design criteria are very difficult to obtain. The reason for this is that the ultimate evaluation of a human operator control system

is necessarily subjective and, with aircraft, the pilot evaluates the aircraft in different ways depending on the type of aircraft and phase of flight. For example, in a dynamic maneuvering situation the pilot may be concerned mainly with the control forces that must be exerted and the resulting 6-DoF translational and angular accelerations. In a task requiring precision tracking the pilot's evaluation will be more influenced by visual cues and the response of the aircraft to turbulence.

Also, a pilot's opinion of the *handling qualities* of an aircraft is inevitably influenced by factors other than the obvious control system considerations of response to control inputs and response to disturbance inputs (e.g., turbulence). He or she will be influenced by the ergonomic design of the cockpit controls, the visibility from the cockpit, the weather conditions, the mission requirements, and physical and emotional factors. The variability introduced by all these factors can only be reduced by averaging test results over many flights and many pilots.

A systematic approach to handling qualities evaluation is available through *pilot opinion rating* scales such as the Cooper-Harper scale (Cooper and Harper, 1969). This rating scale is shown in Table 4.3-1. Once a rating scale like this has been

TABLE 4.3-1 Pilot Opinion Rating and Flying Qualities Level

Aircraft Characteristics	Demands on Pilot in Selected Task or Required Operation	Pilot Rating	Flying Qualities Level
Excellent; highly desirable	Pilot compensation not a factor for desired performance	1	
Good; negligible deficiencies	as above	2	1
Fair; some mildly unpleasant deficiencies	Minimal pilot compensation required for desired performance	3	
Minor but annoying deficiencies	Desired performance requires moderate pilot compensation	4	
Moderately objectionable deficiencies	Adequate performance requires considerable pilot compensation	5	2
Very objectionable but tolerable deficiencies	Adequate performance requires extensive pilot compensation	6	
Major deficiencies	Adequate performance not attainable with maximum tolerable pilot compensation controllability not in question	7	
Major deficiencies	Considerable pilot compensation required for control	8	3
Major deficiencies	Intense pilot compensation required to retain control	9	
Major deficiencies	Control will be lost during some portion of required operation	10	

established, it is possible to begin correlating the pilot opinion rating with the properties of the aircraft dynamic model and hence derive some analytical specifications that will guarantee good handling qualities. Although this may seem simple in principle, it has proven remarkably difficult to achieve in practice, and after many years of handling qualities research it is still not possible to precisely specify design criteria for control systems intended to modify the aircraft dynamics. A survey and a large bibliography covering twenty-five years of handling qualities research has been given by Ashkenas (1984). The "background information and user guides" for the military flying qualities specifications MIL-F-8785B and MIL-F-8785C (Chalk et al., 1969; Moorhouse and Woodcock, 1982) also provide much useful information.

We first consider some possible ways in which requirements for dynamic response may be specified. The aircraft model may be linearized in a particular flight condition and the poles and zeros, or frequency response, of a particular transfer function compared with a specification. Alternatively, certain time responses may be derived from the nonlinear model, in a particular flight condition, and compared with specifications. Yet another alternative is to model the human operator as an element in a closed control loop containing the aircraft dynamics and determine what requirements are placed on the operator if the closed-loop control is to have a satisfactory command or disturbance response. All of these techniques have been or are being considered by workers in the field, and we will examine some of the ideas in more detail.

Pole-Zero Specifications

Suppose that lat-long decoupling is assumed and the pitch axis is considered. In addition, assume linear dynamic behavior. Then if a transfer function shows that the dynamic response is dominated by a single pair of complex poles (e.g., the short-period poles), the pilot's opinion of the aircraft handling qualities should correlate with the position of these poles. A number of studies have provided data to link pole positions to pilot opinion rating.

In one of the early studies, O'Hara (1967) produced iso-opinion contours for the location of the short-period poles; these were plotted on axes of undamped natural frequency versus damping ratio. They showed that the most satisfactory pilot opinion rating corresponded to poles inside a closed contour bounded by about 2.4 and 3.8 rad/s and by damping ratios of about 0.4 and 1.0, with its center at about 3.0 rad/s and $\zeta = 0.65$. This and other similar results form the basis of current pole position handling qualities criteria.

Unfortunately for the pole position criterion, even if the decoupling and linearity assumptions are justified, there are at least two reasons why this approach may not work well. The first is that transfer function zeros are also important (they have a strong effect on step-response overshoot). Second, the aircraft and control system dynamics may include quite a lot of poles that contribute significantly to the time response. Pilots are very sensitive to additional dynamics, and the difficulties of specifying requirements on more than just a single pair of poles quickly become prohibitive. The problem of transfer function zeros will be considered first.

The short-period elevator-to-pitch-rate transfer function (4.2-9) plays an important role in the pilot's assessment of the longitudinal-axis flying qualities. In this transfer function the $Z_{\delta e}$, $Z_{\dot{\alpha}}$, and Z_q terms can usually be neglected, with the following result:

$$\frac{q}{\delta_e} = \frac{Z_\alpha M_{\delta e}(sV_{T_e}/Z_\alpha - 1)}{V_{T_e}s^2 - (Z_\alpha + V_{T_e}M_q + V_{T_e}M_{\dot{\alpha}})\,s + M_q Z_\alpha - V_{T_e}M_\alpha} \tag{4.3-1}$$

In the handling qualities literature the dimensional derivative $L_\alpha (\equiv \partial L/\partial\alpha \approx -\mathrm{m}Z_\alpha$, $C_D \ll C_{L_\alpha})$ is often used instead of Z_α, and the time constant associated with the transfer function zero is given the symbol T_{θ_2} (T_{θ_1} is associated with the phugoid mode). Therefore, we see that

$$T_{\theta_2} = -V_{T_e}/Z_\alpha \approx \mathrm{m}V_{T_e}/L_\alpha \tag{4.3-2}$$

This time constant is also often expressed in terms of the aircraft load factor response to angle of attack, n_α. Aircraft *load factor*, n, is defined as lift (L) divided by the weight (W), and n_α is the gradient of this quantity with respect to alpha [$n_\alpha = (\partial L/\partial\alpha)/W$]. Therefore, we have

$$T_{\theta_2} = V_{T_e}/(g_D n_\alpha) \tag{4.3-3}$$

The position of the pitch-rate transfer function zero has been shown to correlate with pilot opinion ratings of the flying qualities (Chalk, 1963). Shomber and Gertsen (1967) derived iso-opinion curves involving the short-period frequency and damping, T_{θ_2}, and n_α. When n_α was less than 15 g/rad, they found that pilot opinion correlated well with $1/(\omega_n T_{\theta_2})$ and ζ, with the optimum conditions being around $1/(\omega_n T_{\theta_2}) = 0.45$, $\zeta = 0.7$. When n_α was greater than 15, they found that the correlation was with n_α/ω_n (i.e., T_{θ_2} no longer fixed) and ζ, with the optimum conditions near $n_\alpha/\omega_n = 10$, $\zeta = 0.7$. The military flying qualities requirements (see later) specify the short-period natural frequency in terms of n_α, and there is still a division of opinion over the importance of T_{θ_2} versus n_α.

The lateral-directional dynamics have proved somewhat less critical than the longitudinal dynamics from the point of view of handling qualities. The normally required changes in the aircraft trajectory can be achieved by a combination of rolling and pitching. O'Hara (1967) used iso-opinion curves to show that lateral dynamics would receive a good rating if the maximum roll acceleration was appropriate for the roll time constant. Both of these quantities are transfer function parameters. Regardless of these studies the current military requirements provide only specifications for the roll time constant and the time to reach a given roll angle. The latter quantity must be obtained from a flight test or a nonlinear simulation.

The dutch roll mode is an unwanted complication in this simple picture; it should be fast and adequately damped (see later) so that the airplane will quickly reorient itself after a directional disturbance. Ideally, the dutch roll should have very little involvement in the lateral dynamics and should therefore almost cancel out of the lateral transfer functions. This requires that quantities ω_ϕ and ζ_ϕ for the complex zeros [see (4.2-24)] should coincide with ω_d and ζ_d for the dutch roll poles. The

ratio ω_ϕ/ω_d is the most important quantity in this respect, and iso-opinion curves of ω_ϕ/ω_d versus ζ_d have been plotted (Ashkenas, 1966).

As might be expected, the optimum value of ω_ϕ/ω_d is close to unity for a stable dutch roll. However, there is a subtlety in these results; it can be shown that favorable yaw is generated in a turn when $\omega_\phi/\omega_d > 1$, and the converse is true. We will refer to this again in connection with the lateral-directional control augmentation system in Section 4.5.

Finally, consider the case of highly augmented aircraft, where the control systems contribute a number of poles and zeros in addition to those associated with the basic rigid-body transfer functions. Specifications placed on poles and zeros quickly become unmanageable and, as in the case of control system design, one must resort to frequency-response techniques. One way in which frequency-domain ideas have been applied to handling qualities specifications is described in the next subsection.

Frequency-Response Specifications

In general, the goal of an aircraft control system design should be to produce dominant closed-loop poles that resemble the basic rigid-body poles, with satisfactory damping and natural frequency. The effect of the additional dynamics resulting from the control system compensation networks, and possibly the lower-frequency flexible modes, can be allowed for by determining an "equivalent low-order system" (Craig and Ashkenas, 1971; Hodgkinson, 1979; Bischoff, 1981; Gentry, 1982).

In this concept the coefficients are determined for a low-order transfer function that matches the frequency response of the actual transfer function over a limited frequency range. The gain and phase are matched simultaneously by adjusting the coefficients of the low-order transfer function to minimize a cost function of the form

$$\text{COST} = \frac{20}{n}\sum_{i=1}^{i=n}\left[\Delta G\left(\omega_i\right)^2 + \frac{\Delta P(\omega_i)^2}{57.3}\right] \tag{4.3-4}$$

Here n is the number of discrete frequencies (ω_i) used, $\Delta G(\omega_i)$ is the difference in gain (in decibels) between the transfer functions at the frequency ω_i, and $\Delta P(\omega_i)$ is the difference in phase (in degrees) at ω_i. The frequency range used is nominally 0.3 to 10 rad/s, and 20 to 30 discrete frequencies are needed. The upper frequency limit is based on the maximum control frequencies that pilots have been observed to use. The lower limit is based on observations that pilots do not provide continuous closed-loop control at very low frequencies, and the value given does not provide for matching the phugoid mode. The cost function is minimized with a multivariable search routine, in the same way that we obtained steady-state trim in Chapter 3.

The stick-force-to-pitch-rate transfer function is typically used to evaluate the longitudinal dynamics. To compare a particular aircraft with both the short-period and phugoid specifications in the military flying qualities specifications, the assumed form of this transfer function is

$$\frac{q}{F_s} = \frac{K(s + 1/T_{\theta_1})(s + 1/T_{\theta_2})e^{-\tau s}}{\left(s^2 + 2\zeta_p\omega_{n_p}s + \omega_{n_p}^2\right)\left(s^2 + 2\zeta_{sp}\omega_{n_{sp}}s + \omega_{n_{sp}}^2\right)}\frac{\text{rad/s}}{\text{lb}} \tag{4.3-5}$$

Here the subscripts p and sp indicate, respectively, the phugoid and short-period modes. The frequency range for matching the transfer functions should be extended down to about 0.01 rad/s when the phugoid is included.

The term $e^{-\tau s}$ is included in the low-order model to provide an equivalent time delay for matching high-frequency effects from, for example, actuator modes, structural modes and mode filters, and noise filters. The time delay term contributes only a phase shift to the transfer function; this is consistent with the fact that the phase variations from high-frequency dynamics extend over a larger frequency range than gain variations. The military requirements suggest that for level-1 handling qualities, the maximum allowable value of the equivalent time delay should be 10.0 ms.

If a good fit to an equivalent low-order system is obtained (e.g., a cost of 10.0 or less), the pole-zero criteria can be applied to this equivalent system. If low values of the cost function cannot be obtained, other criteria must be used.

Another example of frequency-domain specifications applied to aircraft control systems (but not directly to handling qualities) is the military standard requirement document for the design, installation, and test of flight control systems (*MIL-F-9490,* 1975). This provides stability criteria by specifying the minimum gain and phase margins that must be achieved in any actuator path, with all other feedback paths closed. Typical values are a 6-dB gain margin and 30° phase margin.

Time-Response Specifications

Placing handling qualities requirements on the time response has the advantage that a time response can readily be obtained from the full nonlinear model dynamics. It does, however, raise the problems of what type of test input to apply and which output variable to observe. In the case of the longitudinal dynamics, it is natural once again to specify requirements on the pitch-rate response. However, fighter aircraft control systems are normally designed to give the pilot control over pitch rate at low speed and normal acceleration (acceleration measured along the body negative z-axis) at high speed. The latter gives direct control over the variable that stresses the pilot. The two control schemes must be smoothly blended together (see, e.g., Toles, 1985).

Efforts to develop time-response criteria have mostly been linked to the decoupled longitudinal dynamics and have made use of the short-period approximation. They have attempted to define an envelope inside which the pitch rate, angle of attack, or normal acceleration response to an elevator step input should lie. As early as 1963 a step-response envelope for angle of attack was derived from the short-period iso-opinion curves (Rynaski, 1985). Envelope criteria have been published for the pitch-rate response of an SST and of the space shuttle (see Rynaski, 1985).

A time-history envelope criterion, $C^*(t)$, called "C-star," was published in 1965 (Tobie et al., 1966) and is still in use. The C^* criterion uses a linear combination of pitch rate and normal acceleration at the pilot's station:

$$C^*(t) = a_{n_p} + 12.4q, \tag{4.3-6}$$

where a_{n_p} is the normal acceleration in g's (approximately zero g's = level flight) and q is the pitch rate in radians per second. The envelope for the C^* criterion is shown in

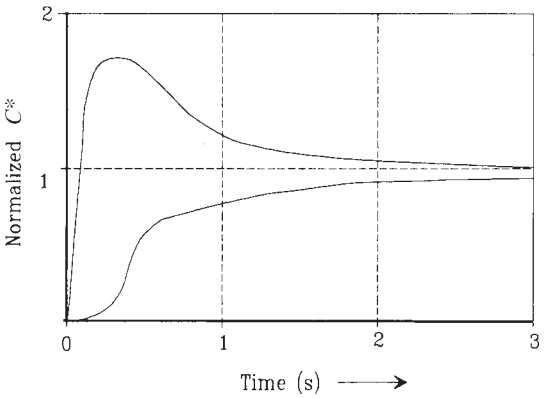

Figure 4.3-1 The *C*-star envelope.

Figure 4.3-1. If the response $C^*(t)$ to an elevator step input falls inside the envelope, level-1 flying qualities on the pitch axis will hopefully be obtained. A more recent time-domain criterion than C^* relates pilot opinion ratings to target tracking error and time on target for a step target tracking task (Onstott and Faulkner, 1978).

The cited envelope criteria often give conflicting results and may disagree with the pilot ratings for specific aircraft. Pitch-rate responses having large overshoots and poor settling times have often corresponded to good pilot opinion ratings. It is known that for fighter aircraft air combat modes a pitch-rate overshoot is required for good gross acquisition of targets, and a deadbeat pitch-rate response is required for good fine tracking. Rynaski (1985) has argued that angle of attack should be the basic response variable, and it appears that the angle-of-attack response corresponding to good handling qualities may be more like a good conventional step response (i.e., small overshoot and fast nonoscillatory settling).

A time-response criterion, called D^* (or coordination perception parameter), has been devised for the lateral-directional response (Kisslinger and Wendle, 1971). The idea is similar to C^* in that the coordination perception parameter is a blend of lateral acceleration and sideslip angle, and envelope limits for acceptable performance are specified.

Requirements Based on Human Operator Models

For certain types of control tasks it is possible to model a human operator with linear differential equations or a transfer function. An example of such a task is a compensatory tracking task with a random input, that is, a control task in which the operator uses only tracking *error* information to track an unpredictable target. This information may be presented by instruments such as a pilot's artificial horizon display. The human operator model consists of the transfer function and an added nonanalytic output signal called the *remnant*. The purpose of the remnant is to account for the discrepancies between experimental results with a human operator and analyses using the model. The transfer function model is often given the name *human operator*

describing function (not to be confused with the describing function of nonlinear control theory).

The human operator transfer function model for the compensatory tracking task is usually assumed to be

$$Y(s) = \frac{K_p e^{-ds}(\tau_\ell s + 1)}{(\tau_i s + 1)(\tau_n s + 1)} \tag{4.3-7}$$

In this transfer function the pure delay, d, may be taken to represent the motor control functions in the cerebellum and the neuromuscular delay, while the lag τ_n models the mechanical properties of the muscles and limbs. It is known that the speed of response is severely limited by the delay term rather than the lag, and the latter is neglected in many applications. The gain, K_p, lead time constant, τ_ℓ, and lag time constant, τ_i, represent the capability of the human operator to optimize his or her control of a given task. Thus, the operator may use lag compensation to achieve high gain and fine control in some low-bandwidth tasks or lead compensation to achieve high bandwidth.

This model has been applied to aircraft piloting tasks, and hypotheses (the *adjustment rules*) have been developed for the way in which the adaptive parameters will be "chosen" by the pilot (McRuer et al., 1965). It is also used as the basis of a transfer function method of assessing flying qualities (Neal and Smith, 1970). Interesting examples of the transfer function model applied to a pilot controlling roll angle are given by Etkin (1972) and Roskam (1979).

In the Neal-Smith method the model (4.3-7) is used in conjunction with the aircraft stick-force-to-pitch-attitude transfer function in a closed pitch-attitude control loop. It is assumed that the human pilot adjusts the lead, lag, and gain, so that the *droop* and *peak magnification* of the closed-loop frequency response are minimized, as shown in Figure 4.3-2. Therefore, this process is duplicated with the models, the lag τ_n is neglected, and the delay is taken as $d = 0.3$ s. The lead and lag time constants are adjusted, according to the adjustment rules, to optimize the closed-loop frequency response. When this has been done, the maximum lead or lag provided by the pilot

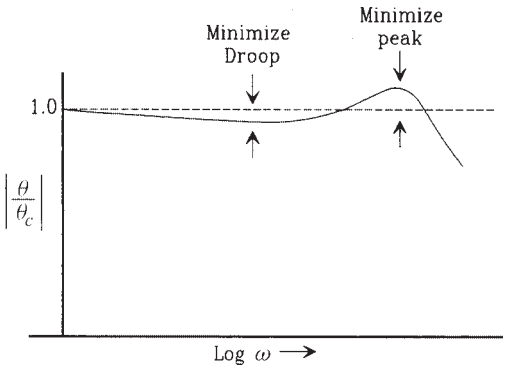

Figure 4.3-2 Closed-loop frequency response for Neal-Smith criterion.

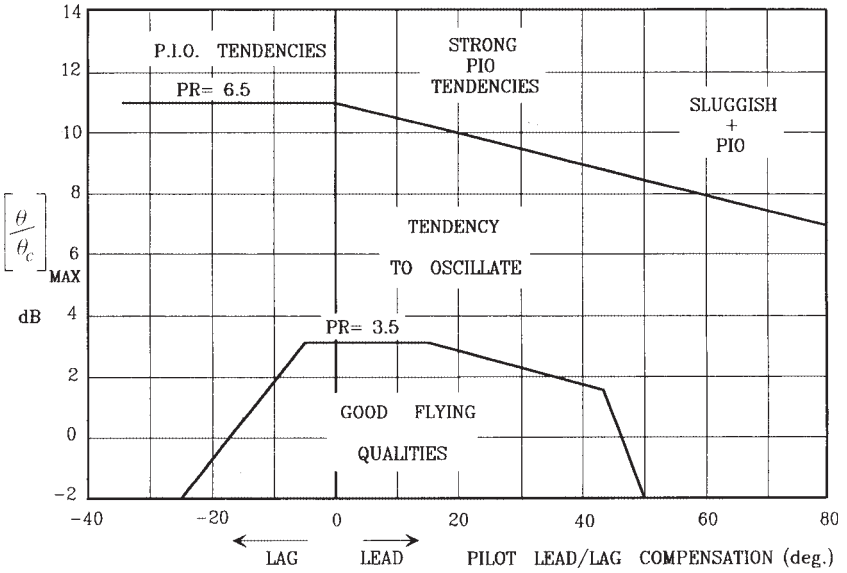

Figure 4.3-3 Neal-Smith evaluation chart.

model is determined, together with the value of the peak magnification. The pilot opinion rating is then determined from a plot like that shown in Figure 4.3-3.

A later development than the transfer function model of the human operator is the *optimal control model* (OCM), attributable mainly to Baron, Kleinman, and Levison (Kleinman et al., 1970, p. 358). It uses a state-variable formulation and optimal control theory and is based on the assumption that "a well-motivated, well-trained human operator behaves in a near optimal manner, subject to his inherent limitations and constraints and his control task." A description of this model is outside the scope of this chapter, since it has not found its way directly into flying qualities specifications. More information can be found in the book by Sheridan and Ferrell (1974) and in the references cited. A summary of work in human operator modeling, with a fairly comprehensive bibliography, has been given by Gerlach (1977).

Human operator modeling applied to a pilot performing compensatory tracking tasks has now accumulated quite a long history, and attention has turned to modeling the human operator performing other piloting tasks. In a modern fighter aircraft the workload involved in operating all of the different systems (flight control, navigation, radar, weapons, etc.) can be overwhelming, and modeling the human decision-making process has become important. A survey of the relationship of flying qualities specifications to task performance and the use of pilot models has been given by George and Moorhouse (1982).

Other Requirements

The preceding subsections described ways in which the dynamic response of an aircraft and its control systems can be characterized and how these may lead to handling

qualities criteria. There are a number of other requirements that must be satisfied for an aircraft to receive a good handling qualities rating. Some of these have no direct effect on control system design, but they are "inside the loop" that is closed by the pilot. They will be briefly described because of their importance.

One of the more important characteristics of the pilot's controls is the *control feel*, that is, the force and deflection characteristics of the control stick during a particular maneuver. Aircraft whose control surfaces are not power boosted require much careful balancing of the control surfaces and the addition of a mass and springs to the control stick in order to obtain satisfactory feel. Aircraft with fully powered, irreversible controls require an artificial-feel system.

Artificial feel may take the form of centering springs, an electromechanical damper, and, for longitudinal control, a mechanical or hydraulic system that provides a stick reaction force proportional to the normal acceleration in *g*s during a pull-up maneuver. Iso-opinion studies have shown that the amount of stick force per *g* is quite critical and there is an associated optimum value of stick deflection. Stick-force-per-*g* requirements are given in the military aircraft specifications, in addition to the control forces required in various flight phases.

Another factor that influences a pilot's opinion of handling qualities, particularly in the landing phase, is speed stability. The aircraft response to a speed disturbance is an exponential change, and this response will typically be rated as satisfactory if it is stable with a time constant of less than about 50 s. An unstable exponential response may be acceptable under some conditions provided that the time constant is greater than about 25 s.

The Military Flying Qualities Specifications

In the preceding subsections we attempted to convey some idea of the difficulty of specifying analytical performance criteria for the dynamic behavior of piloted aircraft. The civil and military aviation authorities of various countries are also faced with this problem. In general, their requirements documents are not very analytical and do not provide any way out of our difficulty. However, the U.S. "Military Specification for the Flying Qualities of Piloted Airplanes" (*MIL-F-8785C,* 1980) does provide some analytical specifications that must be met by U.S. military aircraft. A background document and user guide, containing much useful information and a large bibliography, is also available (Chalk et al., 1969). These documents are readily available, and only the mode specifications of *MIL-F-8785C* will be summarized here. (Note that *MIL-F-8785C* has now been superseded by *MIL 1797,* which contains additional information, but this document has limited circulation.)

The military specification defines airplane classes, flight phases, and flying qualities levels, so that different modes can be specified for the various combinations. These are defined in Table 4.3-2; the flying qualities levels are linked to the Cooper-Harper ratings as shown in Table 4.3-1. The specifications for the aircraft modes are as follows.

TABLE 4.3-2 Definitions—Flying Qualities Specifications

Airplane Classes

Class I: Small, light airplanes.
Class II: Medium weight, low-to-medium-maneuverability airplanes.
Class III: Large, heavy, low-to-medium-maneuverability airplanes.
Class IV: High-maneuverability airplanes.

Flight Phases

Category A: Nonterminal flight phases generally requiring rapid maneuvering.
Category B: Nonterminal flight phases normally accomplished using gradual maneuvers without precision tracking, although accurate flight-path control may be required.
Category C: Terminal flight phases normally accomplished using gradual maneuvers and usually requiring accurate flight-path control.

Flying Qualities Levels

Level 1: Flying qualities adequate for the mission flight phase.
Level 2: Flying qualities adequate to accomplish the mission flight phase, but some increase in pilot workload or degradation in mission effectiveness exists.
Level 3: Flying qualities such that the airplane can be controlled safely, but pilot workload is excessive, or mission effectiveness is inadequate, or both.

Phugoid Specifications The military specification dictates that for the different levels of flying qualities the damping ζ_p and natural frequency ω_{n_p} of the phugoid mode will satisfy the following requirements:

$$\text{Level 1}: \quad \zeta_P \geq 0.04$$

$$\text{Level 2}: \quad \zeta_P \geq 0.0$$

$$\text{Level 3}: \quad T_{2_p} \geq 55.0\, s$$

In the level-3 requirement the mode is assumed to be unstable, and T_2 denotes the time required for the mode to double in amplitude. For an exponentially growing sinusoidal mode this time is given by

$$T_2 = \log_e 2/(-\zeta\omega_n) \ (\zeta \text{ has negative values})$$

These requirements apply with the pitch control free or fixed; they need not be met transonically in certain cases.

Short-Period Specifications The short-period requirements are specified in terms of the natural frequency and damping of the "short-period mode" of the equivalent low-order system (as defined earlier). The adequacy of the equivalent system

TABLE 4.3-3*a* Short-Period Damping Ratio Limits

	Cat. A & C Flight Phases		Cat. B Flight Phases	
Level	Minimum	Maximum	Minimum	Maximum
1	0.35	1.30	0.30	2.00
2	0.25	2.00	0.20	2.00
3	0.15*	no limit	0.15*	no limit

*May be reduced at altitude > 20,000 ft with approval.

TABLE 4.3-3*b* Limits on $\omega_{n_{sp}}^2/(n/\alpha)$

	Cat. A Phases		Cat. B Phases		Cat. C Phases	
Level	Min.	Max.	Min.	Max.	Min.	Max.
1	0.28 $\omega_n \geq 1.0$	3.60	0.085	3.60	0.16 $\omega_n \geq 0.7$	3.60
2	0.16 $\omega_n \geq 0.6$	10.0	0.038	10.0	0.096 $\omega_n \geq 0.4$	10.0
3	0.16	no limit	0.038	no limit	0.096	no limit

There are some additional limits on the minimum value of n/α and the minimum value of ω_n for different classes of airplane in category C.

approximation is to be judged by the procuring agency. Table 4.3-3*a* shows the requirements on the equivalent short-period damping ratio ζ_{sp}.

The requirements on equivalent undamped natural frequency ($\omega_{n_{sp}}$) are given in Table 4.3-3*b* and are specified indirectly, in terms of the quantity $\omega_{n_{sp}}^2/(n/\alpha)$. The denominator (n/α) of this term is the aircraft load factor response to angle of attack in *g*'s per radian, as explained in the subsection on pole-zero specifications.

Roll-Mode Specifications The maximum allowable value of the roll-subsidence-mode time constant is given in Table 4.3-4. In addition to these time constant specifications there is a comprehensive set of requirements on the time required to achieve various (large) changes in roll angle following an abrupt roll command. For example, for air-to-air combat (a flight phase within category A for class IV airplanes) the minimum allowable time to achieve a certain roll angle depends on airspeed, but for level-1 flying qualities may be as short as 1.0 s for 90° roll and 2.8 s for 360° roll.

Spiral-Mode Specifications The spiral mode is allowed to be unstable, but limits are placed on the minimum time for the mode to double in amplitude, as shown in Table 4.3-5. These requirements must be met following a roll angle disturbance of up to 20° from trimmed-for-zero-yaw-rate wings-level flight, with the cockpit controls free.

TABLE 4.3-4 Maximum Roll-Mode Time Constant (s)

Fligh Phase Category	Class	Level 1	Level 2	Level 3
A	I IV	1.0	1.4	no limit
	II III	1.4	3.0	no limit
B	All	1.4	3.0	10
C	I, II-C, IV	1.0	1.4	no limit
	II-L, III	1.4	3.0	no limit

TABLE 4.3-5 Spiral-Mode Minimum Doubling Time

Flight Phase Category	Level 1	Level 2	Level 3
A & C	12 s	8 s	4 s
B	20 s	8 s	4 s

TABLE 4.3-6 Dutch-Roll-Mode Specifications

Level	Flight Phase Category	Class	min ζ_d	min $\zeta_d\omega_{n_d}$	min ω_{n_d}
	A	I, IV	0.19	0.35	1.0
		II, III	0.19	0.35	0.4
1	B	all	0.08	0.15	0.4
	C	I,II-C,IV	0.08	0.15	1.0
		II-L, III	0.08	0.15	0.4
2	all	all	0.02	0.05	0.4
3	all	all	0.02	no limit	0.04

Dutch-Roll-Mode Specifications The frequency ω_{n_d} and damping ratio ζ_d of the dutch roll mode must exceed the minimum values given in Table 4.3-6. Note that the quantity $\zeta\omega_n$ is the s-plane real-axis coordinate of the roots, and ω_n is the radial distance from the origin for complex roots. Therefore, these requirements define an area of the s-plane in which the dutch roll roots must lie.

The lower limit on ζ_d is the larger of the two values that come from the table, except that a value of 0.7 need not be exceeded for class III. Also, class III airplanes may be exempted from some of the minimum ω_d requirements. Airplanes that have a large amount of roll-yaw coupling, as measured by the ratio of the maximum roll angle to the maximum value of sideslip in a dutch roll oscillation, are subject to a more stringent requirement on $\zeta_d\omega_{n_d}$ (see *MIL-F-8785C*).

The military requirements document specifies dynamic response mainly through the pole-zero requirements. These have been summarized here so that the reader may evaluate some of the controller designs described later. Much additional information covering other aspects of flying qualities is available in the requirements document, and it is essential reading for anyone with other than a casual interest in this field.

4.4 STABILITY AUGMENTATION

Most high-performance commercial and military aircraft require some form of stability augmentation. Some military aircraft are actually unstable and would be virtually impossible to fly without an automatic control system. The SAS typically uses sensors to measure the body-axes angular rates of the vehicle and feeds back processed versions of these signals to servomechanisms that drive the aerodynamic control surfaces. In this way an aerodynamic moment proportional to angular velocity and its derivatives can be generated and used to produce a damping effect on the motion. If the basic mode is unstable or if it is desired to change both damping and natural frequency independently, additional feedback signals will be required, as we will see.

Stability augmentation systems are conventionally designed separately for the longitudinal dynamics and the lateral-directional dynamics, and this is made possible by the decoupling of the aircraft dynamics in most flight conditions. In the next two subsections aircraft model dynamics will be used to describe the design of the various augmentation systems.

Pitch-Axis Stability Augmentation

The purpose of a pitch SAS is to provide satisfactory natural frequency and damping for the short-period mode. This mode involves the variables alpha and pitch rate; feedback of these variables to the elevator actuator will modify the frequency and damping. Figure 4.4-1 shows the arrangement; if the short-period mode is lightly damped but otherwise adequate, only pitch-rate feedback is required. If the frequency and damping are both unsatisfactory or the mode is unstable, alpha feedback is necessary. The phugoid mode will be largely unaffected by this feedback. Outer feedback

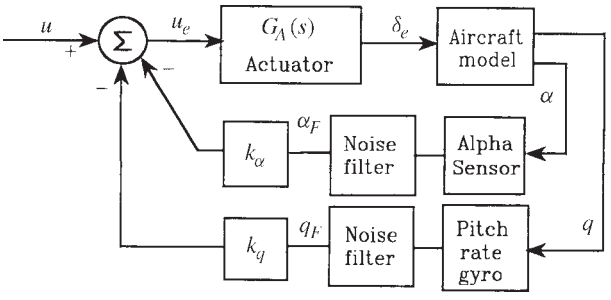

Figure 4.4-1 Pitch-axis stability augmentation.

control loops will often be closed around the pitch SAS to provide, for example, autopilot functions. Automatic adjustment of the augmentation (inner) loop feedback gains may be arranged when the outer feedback loops are engaged, so that the overall performance is optimal.

A physical understanding of the effect of alpha feedback follows from the explanation of pitch stiffness in Chapter 2. A statically unstable aircraft has a pitching moment curve with a positive slope over some range(s) of alpha. If perturbations in alpha are sensed and fed back to the elevator servo to generate a restoring pitching moment, the slope of the pitching moment curve can be made more negative in the region around the operating angle of attack. Furthermore, the overall pitching moment curve and the trimmed elevator deflection will not be affected, thus preserving the trim-drag and maneuverability characteristics that the designer built into the basic airplane design.

The angle-of-attack measurement may be obtained from the pitot-static air data system, or a small "wind vane" mounted on the side of the aircraft forebody and positioned (after much testing and calibration) to measure alpha over a wide range of flight conditions. Two sensors may be used, on opposite sides of the aircraft, to provide redundancy and possibly to average out measurement errors caused by sideslipping. In addition, it may be necessary to compute (in real time) a "true" angle of attack from the "indicated angle of attack," airspeed, and Mach number, in order to relate the freestream angle of attack of the airframe to the direction of the flowfield at the sensor position. The signal from the alpha sensor is usually noisy because of turbulence, and a noise filter is used to reduce the amount of noise injected into the control system.

Alpha feedback is avoided if possible because of the difficulty of getting an accurate, rapidly responding, noise-free measurement and because of the vulnerability of the sensor to mechanical damage. Noise from the alpha sensor can make it difficult to achieve precise pointing (e.g., for targeting), so the amount of alpha feedback is normally restricted.

The pitch-rate sensor is normally a mechanical gyroscopic device arranged to measure the (inertial) angular rate around the pitch axis. The location of the gyro must be chosen very carefully to avoid picking up the vibrations of the aircraft structure. At a node of an idealized structural oscillation there is angular motion but no displacement, and at an antinode the converse is true. Thus, the first choice for the rate gyro location is an antinode corresponding to the most important structural mode. Flight tests must then be used to adjust the position of the gyros. A bad choice of gyro locations can adversely affect handling qualities or, in extreme cases, cause oscillations in the flight control systems (AFWAL-TR-84-3105, 1984). The gyro filter shown in Figure 4.4-1 is usually necessary to remove noise and/or cancel structural-mode vibrations.

The sign convention that has been adopted in this book (see Chapter 3) means that a positive elevator deflection leads to a negative pitching moment. Therefore, for convenience, a phase reversal will be included between the elevator actuator and the control surface in each example, so that the positive-gain root-locus algorithm can be used for design.

Example 4.4-1: The Effects of Pitch Rate and Alpha Feedback The longitudinal (four-state) Jacobian matrices for the F-16 model in the nominal flight condition in Table 3.6-3 are

$$A = \begin{matrix} \\ \\ \\ \\ \end{matrix} \begin{matrix} v_T \\ \\ \\ \\ \end{matrix} \begin{bmatrix} -1.9311E-02 & 8.8157E+00 & -3.2170E+01 & -5.7499E-01 \\ -2.5389E-04 & -1.0189E+00 & 0.0000E+00 & 9.0506E-01 \\ 0.0000E+00 & 0.0000E+00 & 0.0000E+00 & 1.0000E+00 \\ 2.9465E-12 & 8.2225E-01 & 0.0000E+00 & -1.0774E+00 \end{bmatrix} \begin{matrix} \\ \alpha \\ \theta \\ q \end{matrix}$$

$$B = \begin{matrix} \\ \\ \\ \\ \end{matrix} \begin{matrix} \delta_e \\ \\ \\ \\ \end{matrix} \begin{bmatrix} 1.7370E-01 \\ -2.1499E-03 \\ 0.0000E+00 \\ -1.7555E-01 \end{bmatrix} \tag{1}$$

$$C = \begin{bmatrix} 0.000000E+00 & 5.729578E+01 & 0.000000E+00 & 0.000000E+00 \\ 0.000000E+00 & 0.000000E+00 & 0.000000E+00 & 5.729578E+01 \end{bmatrix} \begin{matrix} \alpha \\ q \end{matrix}$$

The single input is the elevator deflection, δ_e, in degrees, and the two outputs are the appropriate feedback signals: alpha and pitch rate. The entries in the C-matrix are the conversions to units of degrees for consistency with the input.

Either of the two SISO transfer functions obtained from the coefficient matrices will exhibit the dynamic modes for this flight condition; the elevator-to-alpha transfer function is

$$\frac{\alpha}{\delta_e} = \frac{-0.1232(s+75.00)(s+0.009820 \pm j0.09379)}{(s-0.09755)(s+1.912)(s+0.1507 \pm j0.1153)} \tag{2}$$

Unlike the transfer functions for stable cg positions (e.g., $x_{CG} = 0.3\,\overline{c}$) in Chapter 3, this transfer function does not exhibit the usual phugoid and short-period poles. The pole at $s \approx .098$ indicates an unstable exponential mode with a time constant of about 10 s. The complex pole pair corresponds to an oscillatory mode with a period of 33 s and damping ratio of 0.79; this is like a phugoid period with a short-period damping ratio. This mode is the "third oscillatory mode" of the statically unstable airplane (see Section Aircraft Rigid-Body Modes).

The modes described above obviously do not satisfy the requirements for good handling qualities, and providing continuous control of the unstable mode would be a very demanding job for a pilot. We will now show that alpha and pitch-rate feedback together will restore stability and provide virtually complete control of the position of the short-period poles.

The configuration shown in Figure 4.4-1 will be used with an alpha filter but, for simplicity, no pitch-rate filter. The actuator and alpha filter models are taken from the original F-16 model report (Nguyen et al., 1979) and are both simple-lag filters with

time constants $\tau_a = 1/20.2$ s and $\tau_F = 0.1$ s, respectively. The aircraft state-space model (1) augmented with these models, is

$$\dot{x} = \left[\begin{array}{cccc:c:c} & & & & & & 0 \\ & & & & & & 0 \\ & A & & & & -B & 0 \\ & & & & & & 0 \\ \hdashline 0 & 0 & 0 & 0 & -20.2 & & 0 \\ 0 & 10.0 & 0 & 0 & 0 & & -10.0 \end{array}\right] \left[\begin{array}{c} v_T \\ \alpha \\ \theta \\ q \\ \hdashline x_a \\ x_F \end{array}\right] + \left[\begin{array}{c} 0 \\ 0 \\ 0 \\ 0 \\ \hdashline 20.2 \\ 0 \end{array}\right] u_e \qquad (3a)$$

$$y = \left[\begin{array}{c} \alpha \\ q \\ \hdashline \alpha_F \end{array}\right] = \left[\begin{array}{cccc:c:c} & & C & & & 0 & 0 \\ & & & & & 0 & 0 \\ \hdashline 0 & 0 & 0 & 0 & & 0 & 57.29578 \end{array}\right] x \qquad (3b)$$

Notice that the original state equations are still satisfied and the original δ_e input is now connected to the actuator state x_a through the phase reversal. The actuator is driven by a new input, u_e. Also, the α filter is driven by the α state of the aircraft dynamics, and an additional output has been created so that the filtered signal α_F is available for feedback. These state equations could also have been created by simulating the filters as part of the aircraft model and running the linearization program again. In the rest of this chapter the augmented matrices will be created by the MATLAB "series" command, as used in Chapter 3.

The state equations (3) can now be used to obtain the loop transfer functions needed for root-locus design. In the case of the innermost (alpha) loop, we already know that the α-loop transfer function will consist of Equation (2) with the two lag filters in cascade, and the effect of the feedback k_α can be anticipated using a sketch of the pole and zero positions. The goal of the alpha feedback is to pull the unstable pole, at $s = 0.098$, back into the left-half s-plane. Let the augmented coefficient matrices in Equation (3) be denoted by *aa*, *ba,* and *ca*. Then the following MATLAB commands can be used to obtain the root locus:

```
k= logspace(-2,1,2000);
r= rlocus(aa,ba,ca(3,:),0,k);     % 3rd row of C
plot(r)
grid on
axis([-20,1,-10,10])
```

Figures 4.4-2*a* and *b* show the root-locus plot for the inner loop on two different scales. The expanded scale near the origin (Figure 4.4-2*b*) shows that the effect of the alpha feedback is to make the loci from the third-mode poles come together on the real axis (near $s = -0.2$). The branch going to the right then meets the locus coming from the unstable pole, and they leave the real axis to terminate on the complex zeros near the origin. This provides a pair of closed-loop poles that correspond to a

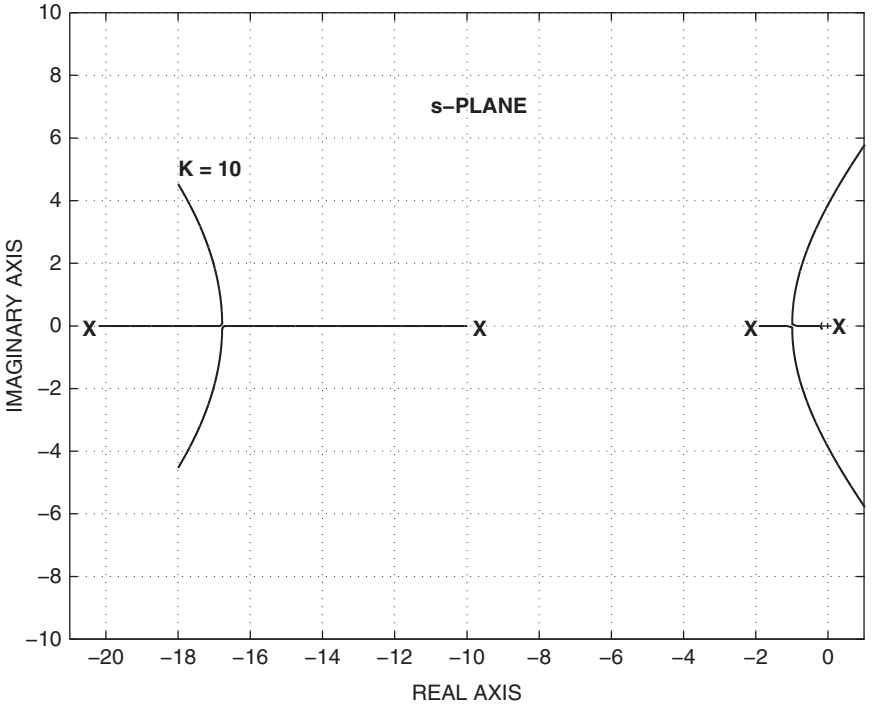

Figure 4.4-2*a* Inner-loop root-locus plot for pitch SAS.

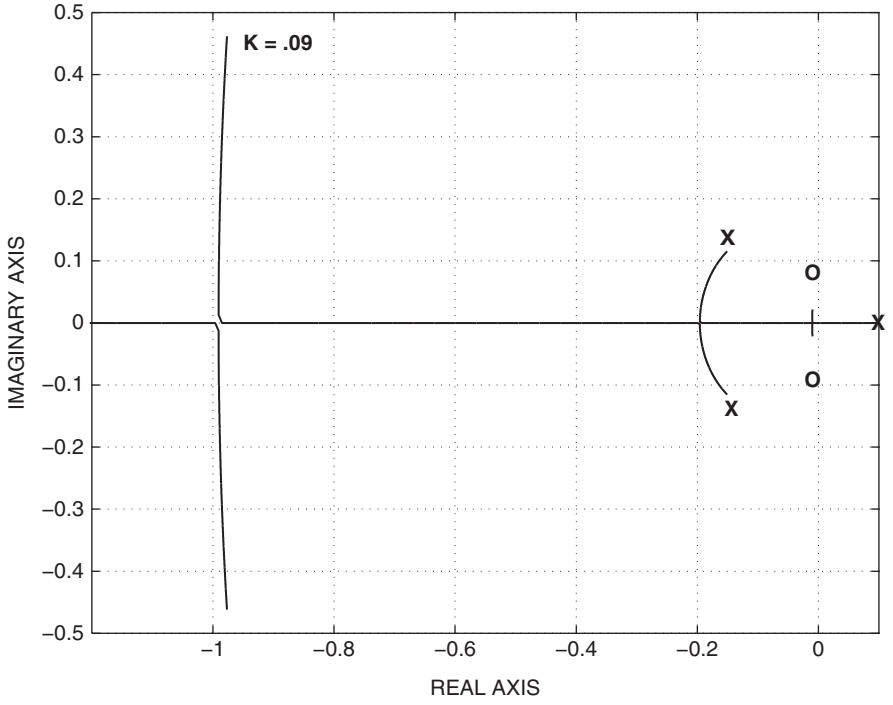

Figure 4.4-2*b* Expanded inner-loop root-locus plot for pitch SAS.

phugoid mode. The left branch from the third-mode poles meets the locus from the pole at $s = -1.9$, and they leave the axis near $s = -1$ to form a short-period mode. Alpha feedback has therefore produced the anticipated effect: The aircraft is stable with conventional longitudinal modes.

The larger-scale plot (Figure 4.4-2*a*) shows that as the magnitude of the alpha feedback is increased, the frequency of the new short-period poles increases and they move toward the right-half plane. The movement toward the right-half plane is in accordance with the constant net damping rule and the filter and actuator poles moving left. A slower (less expensive) actuator would place the actuator pole closer to the origin and cause the short-period poles to have a lower frequency at a given damping ratio. The position of the short-period poles for $k_\alpha = 0.5$ is $-070 \pm j2.0$. At this position the natural frequency is about 2.2 rad/s, which is acceptable according to the flying qualities requirements, but the damping ratio ($\zeta = 0.33$) is quite low.

A root-locus plot will now show the effect of varying k_q, with k_α fixed at 0.5. The following MATLAB commands can be used:

```
acl= aa- ba*k_α*ca(3,:);                % Choose k_α
%[z,p,k]= ss2zp(acl,ba,ca(2,:),0)      % q/u transf. fn
r= rlocus(acl,ba,ca(2,:),0);
plot(r)
```

The *q/u* transfer function with $k_\alpha = 0.5$ and $k_q = 0$ is

$$\frac{q}{u} = \frac{203.2s(s + 10.0)(s + 1.027)(s + 0.02174)}{(s + 20.01)(s + 10.89)(s + 0.6990 \pm j2.030)(s + 0.008458 \pm j0.08269)} \tag{4}$$

Note that the zeros of this transfer function are the $1/T_{\theta_1}$ and $1/T_{\theta_2}$ unaugmented open-loop zeros, with the addition of a zero at $s = -10$. This zero has appeared because of the MIMO dynamics (two outputs, one input). It originally canceled the alpha filter pole out of the pitch-rate transfer function, but the inner-loop feedback has now moved the alpha filter pole to $s = -10.89$.

Figure 4.4-3 shows the root-locus plot for variable k_q. The phugoid poles move very slightly but are not visible on the plot. The short-period poles follow a circular arc around $s = -1$ (roughly constant natural frequency) as the pitch-rate feedback is increased. The poles become real for quite low values of k_q and, with larger values, a new higher-frequency oscillatory mode is created by the filter and actuator poles. Such a mode would be objectionable to the pilot, and we look for lower values of k_q that make the short-period poles match the flying qualities requirements, with no additional oscillatory mode. The value $k_q = 0.25$ places the short-period poles at $s = -2.02 \pm j1.94$. This corresponds to a natural frequency of 2.8 rad/s and a damping ratio of $\zeta = 0.72$. The corresponding closed-loop transfer function for pitch rate is given by

$$\frac{q}{u} = \frac{203.2s(s + 10.0)(s + 1.027)(s + 0.02174)}{(s + 16.39)(s + 11.88)(s + 2.018 \pm j1.945)(s + 0.008781 \pm j0.06681)} \tag{5}$$

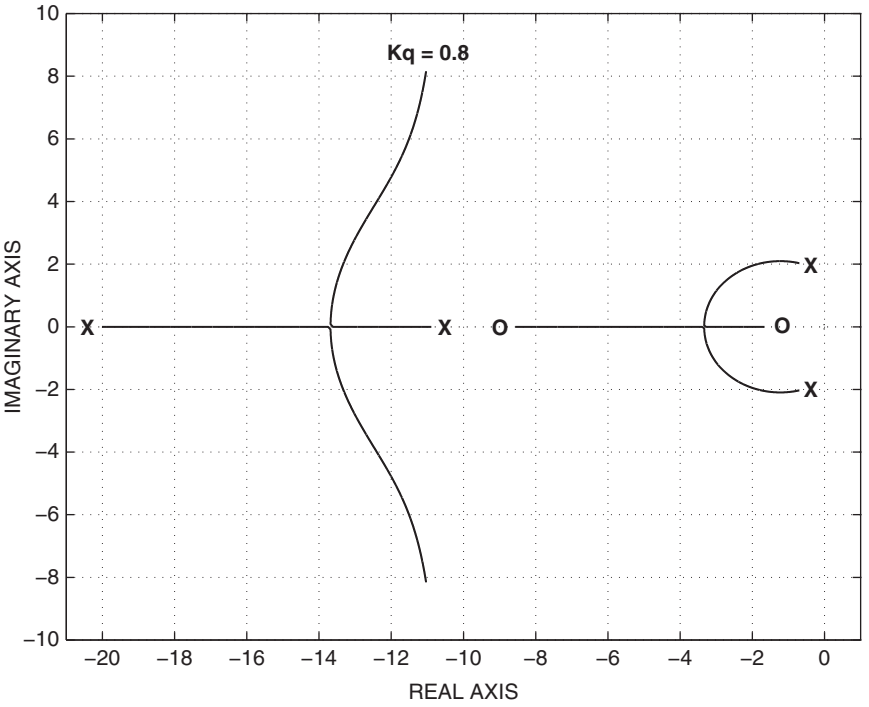

Figure 4.4-3 Outer-loop root-locus plot for pitch SAS.

The original actuator pole has moved from $s = -20.2$ to $s = -16.39$, and the α-filter pole has moved from $s = -10$ to $s = -11.88$. Apart from these factors, this transfer function is very similar to the stable-cg transfer function in Example 3.8-3 but with improved short-period pole positions. ■

Example 4.4-1 shows that alpha feedback stabilizes the unstable short-period mode and determines its natural frequency, while the pitch-rate feedback mainly determines the damping. The amount of alpha feedback needed to get a satisfactory natural frequency was 0.5° of elevator deflection per degree of alpha. The alpha signal is noisy and sometimes unreliable, and this large amount of alpha feedback is preferably avoided. In the second root-locus plot it can be seen that, as the pitch-rate feedback is varied, the locus of the short-period poles circles around the $1/T_{\theta_2}$ zero. Therefore, by moving the zero to the left, a higher natural frequency can be achieved, or the same natural frequency can be achieved with less alpha feedback. This will be demonstrated in the next example.

Example 4.4-2: A Pitch-SAS Design The coefficient matrices *aa*, *bb*, *cc* from Example 4.4-1 are used again here, and the alpha feedback gain will be reduced to $k_\alpha = 0.1$. A lag compensator with a pole at $s = -1$ and a zero at $s = -3$ will be

cascaded with the plant to effectively move the $1/T_{\theta_2}$ zero to $s = -3$. The MATLAB commands are

```
acl= aa - ba*0.1*ca(3,:);          % Close alpha loop, K_α=.1
qfb= ss(acl,ba,ca(2,:),0);         % SISO system for q f.b.
z=3; p=1;
lag= ss(-p,1,z-p,1);               % Lag compensator
csys= series(lag,qfb);             % Cascade Comp. before plant
[a,b,c,d]= ssdata(csys);
k= logspace(-2,0,2000);
r= rlocus(a,b,c,d,k);
plot(r)
grid on
axis([-20,1,-10,10])
```

The root-locus plot is the same shape as Figure 4.4-3, and when the pitch-rate feedback gain is $k_q = 0.2$, the closed-loop transfer function is

$$\frac{q}{u} = \frac{203.2s(s + 10.0)(s + 1.027)(s + 0.0217)(s + 3)}{(s + 18.02)(s + 10.3)(s + 1.025)(s + 1.98 \pm j2.01)(s + 0.0107 \pm j0.0093)} \quad (1)$$

When the pole and zero close to $s = -1$ are canceled out, this transfer function is essentially the same as in Example 4.4-1 except that there is a zero at $s = -3$ instead of $s = -1$. This zero can be replaced by a zero at $s = -1$ once again, by placing the lag compensator in the feedback path. However, a zero at $s = -1$ produces a much bigger overshoot in the step response than the zero at $s = -3$. Therefore the flying qualities requirements on T_{θ_2} should be checked (see Section The Handling Qualities Requirements) to obtain some guidance on the position of the zero.

This example shows that the same short-period mode, as in Example 4.4-1, can be achieved with much less alpha feedback and less pitch-rate feedback. Also, the transfer function (1) shows that no additional modes are introduced. A dynamic compensator is the price paid for this. Section 4.3 shows that the $1/T_{\theta_2}$ zero will move with flight conditions, and so the compensator parameters may have to be changed with flight conditions. ■

Lateral-Directional Stability Augmentation/Yaw Damper

Figure 4.4-4 shows the most basic augmentation system for the lateral-directional dynamics. Body-axis roll rate is fed back to the ailerons to modify the roll subsidence mode, and yaw rate is fed back to the rudder to modify the dutch roll mode (yaw damper feedback). The lateral (rolling) motion is not, in general, decoupled from the yawing and sideslipping (directional) motions. Therefore, the augmentation systems will be analyzed with the aid of the multivariable state equations (two inputs, ailerons and rudder, and two or more outputs), as implied by the figure. This analysis will be restricted to the simple feedback scheme shown in the figure; in a later section additional feedback couplings will be introduced between the roll and yaw channels.

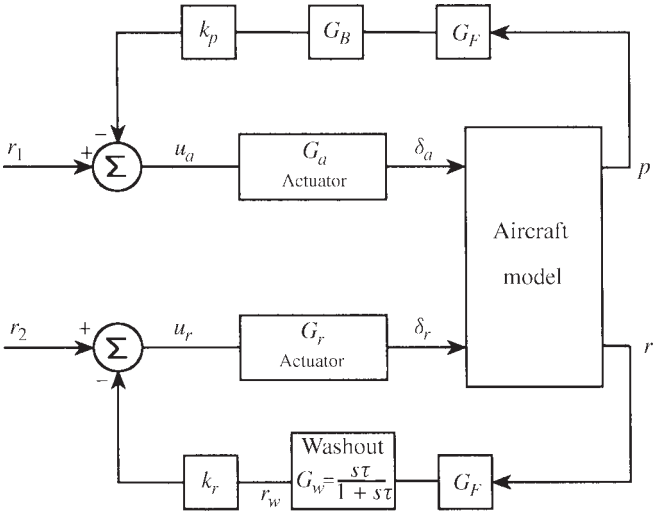

Figure 4.4-4 Lateral-directional augmentation.

The purpose of the yaw damper feedback is to use the rudder to generate a yawing moment that opposes any yaw rate that builds up from the dutch roll mode. This raises a difficulty; in a coordinated steady-state turn the yaw rate has a constant nonzero value (see Table 3.6-3 and the subsection on turn coordination) which the yaw-rate feedback will try to oppose. Therefore, with the yaw damper operating, the pilot must apply larger than normal rudder pedal inputs to overcome the action of the yaw damper and coordinate a turn. This has been found to be very objectionable to pilots. A simple control system solution to the problem is to use "transient rate feedback," in which the feedback signal is differentiated (approximately) so that it vanishes during steady-state conditions. The approximate differentiation can be accomplished with a simple first-order high-pass filter (see Table 3.3-1), called a "washout filter" in this kind of application.

In Figure 4.4-4, G_W is the washout filter, the transfer function G_a represents an equivalent transfer function for differential actuation of the left and right ailerons, and G_r is the rudder actuator. The transfer functions G_F represent noise filtering and any effective lag at the output of the roll-rate and yaw-rate gyros, and G_B is a *bending-mode filter*. The bending-mode filter is needed because the moments generated by the ailerons are transmitted through the flexible-beam structure of the wing, and their effect is sensed by the roll-rate gyro in the fuselage. The transfer function of this path corresponds to a general low-pass filtering effect, with resonances occurring at the bending modes of the wing. Because the wing bending modes are relatively low in frequency, they can contribute significant phase shift, and possibly gain changes, within the bandwidth of the roll-rate loop. The bending-mode filter is designed to compensate for these phase and gain changes.

To understand the purpose of the roll-rate feedback, consider the following facts. In Section 4.2 the variation of the roll time constant with flight conditions was

analyzed, and in Chapter 2 the change of aileron effectiveness with angle of attack was described. These effects cause large, undesirable variations in aircraft roll performance that result in the pilot flying the aircraft less precisely. Closed-loop control of roll rate is used to reduce the variation of roll performance with flight conditions.

While the roll time constant is a feature of the linear small-perturbation model and gives no indication of the maximum roll rate or time to roll through a large angle, it is relevant to the initial speed of response and control of smaller-amplitude motion. Figure 4.4-5 shows a plot of the reciprocal of the F-16 roll time constant versus alpha and indicates that this time constant may become unacceptably slow at high angles of attack. The plot was derived by trimming the F-16 model in straight and level flight at sea level, with the nominal cg position, over a range of speeds. At angles of attack greater than about 20° the roll pole coupled with the spiral pole to form a complex pair.

Landing approach takes place at a relatively high angle of attack, and the roll-rate feedback may be needed to ensure good roll response. Also, satisfactory damping of the dutch roll mode is particularly important during landing approach in gusty crosswind conditions. Our F-16 model does not include flaps and landing gear, so the design of the augmentation loops will simply be illustrated on a low-speed, low-altitude flight condition. If we take the F-16 model dynamics at zero altitude,

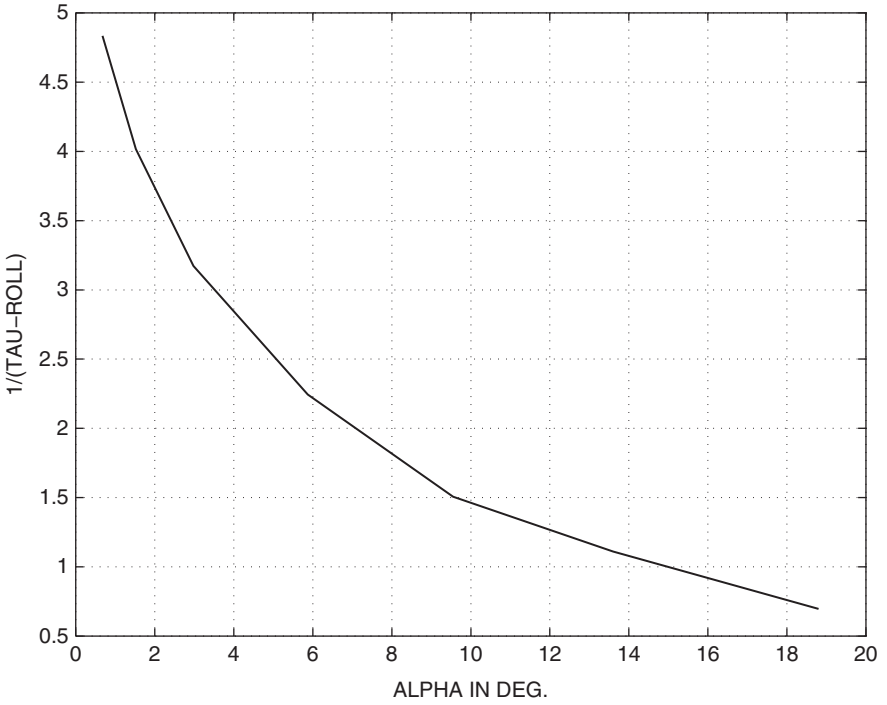

Figure 4.4-5 F-16 model roll time constant versus alpha in degrees.

with the nominal cg position and an airspeed of 205.0 ft/s (alpha = 18.8°), the roll pole is real and quite slow ($\tau = 1.44$ s), and the dutch roll is very lightly damped ($\zeta = 0.2$). The state equations can be found by linearization, and a five-state set of lateral-directional equations can be decoupled from the full thirteen-state set. The coefficient matrices are found to be

$$A = \begin{array}{c} \begin{matrix} \beta & \phi & \psi & p & r \end{matrix} \\ \begin{bmatrix} -0.13150 & 0.14858 & 0.0 & 0.32434 & -0.93964 \\ 0.0 & 0.0 & 0.0 & 1.0 & 0.33976 \\ 0.0 & 0.0 & 0.0 & 0.0 & 1.0561 \\ -10.614 & 0.0 & 0.0 & -1.1793 & 1.0023 \\ 0.99655 & 0.0 & 0.0 & -0.0018174 & -0.25855 \end{bmatrix} \end{array}$$

$$B = \begin{array}{c} \begin{matrix} \delta_a & \delta_r \end{matrix} \\ \begin{bmatrix} 0.00012049 & 0.00032897 \\ 0.0 & 0.0 \\ 0.0 & 0.0 \\ -0.1031578 & 0.020987 \\ -0.0021330 & -0.010715 \end{bmatrix} \end{array} \tag{4.4-1a}$$

$$C = \begin{bmatrix} 0.0 & 0.0 & 0.0 & 57.29578 & 0.0 \\ 0.0 & 0.0 & 0.0 & 0.0 & 57.29578 \end{bmatrix} \begin{matrix} p \\ r \end{matrix} \qquad D = \begin{bmatrix} 0 & 0 \\ 0 & 0 \end{bmatrix} \tag{4.4-1b}$$

The null column in the A-matrix shows that the state ψ is not coupled back to any other states, and it can be omitted from the state equations when designing an augmentation system. The C-matrix has been used to convert the output quantities to degrees, to match the control surface inputs. The transfer functions of primary interest are

$$\frac{p}{\delta_a} = \frac{-5.911(s - 0.05092)(s + 0.2370 \pm j1.072)}{(s + 0.06789)(s + 0.6960)(s + 0.4027 \pm j2.012)} \tag{4.4-2}$$

$$\frac{r}{\delta_a} = \frac{-0.1222(s + 0.4642)(s + 0.3512 \pm j4.325)}{(s + 0.06789)(s + 0.6960)(s + 0.4027 \pm j2.012)} \tag{4.4-3}$$

$$\frac{p}{\delta_r} = \frac{+1.202(s - 0.05280)(s - 2.177)(s + 1.942)}{(s + 0.06789)(s + 0.6960)(s + 0.4027 \pm j2.012)} \tag{4.4-4}$$

$$\frac{r}{\delta_r} = \frac{-0.6139(s + 0.5078)(s + 0.3880 \pm j1.5439)}{(s + 0.06789)(s + 0.6960)(s + 0.4027 \pm j2.012)} \tag{4.4-5}$$

The dutch roll poles are not canceled out of the p/δ_a transfer function by the complex zeros. Therefore, coupling exists between the rolling and yawing motions, and the dutch roll mode will involve some rolling motion. These transfer functions validate the decision to use the MIMO state equations for the analysis. At lower angles of

attack the dutch roll poles will typically be largely canceled out of the p/δ_a transfer function, leaving only the roll subsidence and spiral poles.

The two roll-rate transfer functions given above contain NMP zeros close to the origin. This is because gravity will cause the aircraft to begin to sideslip as it rolls. Then, if the dihedral derivative C_{l_β} is negative (positive roll stiffness), the aircraft will have a tendency to roll in the opposite direction. This effect will be more pronounced in a slow roll when the sideslip has a chance to build up.

The rudder-to-roll-rate transfer function has another NMP zero farther away from the origin, corresponding to faster-acting NMP effects. A positive deflection of the rudder directly produces a positive rolling moment (see Table 3.5-1) and a negative yawing moment. The negative yawing moment rapidly leads to positive sideslip, which will in turn produce a negative rolling moment if the aircraft has positive roll stiffness. This effect tends to cancel the initial positive roll, and the NMP zero is the transfer function manifestation of these competing effects.

Example 4.4-3: A Roll Damper/Yaw Damper Design In Figure 4.4-4 the aileron and rudder actuators will be taken as simple lags with a corner frequency of 20.2 rad/s (as in the original model), and the bending mode filter will be omitted. The coefficient matrices for the plant will be (4.4-1) with the ψ state removed and denoted by *ap*, *bp*, *cp*, *dp*. Positive deflections of the control surfaces lead to negative values for the principal moments (Table 3.5-1) so, in order to use the positive-gain root locus for design, we will insert a phase reversal at the output of the control surface actuators (in the *C*-matrix). The aileron and rudder actuators will be combined into one two-input, two-output state model and cascaded with the plant as follows:

```
aa= [-20.2 0; 0 -20.2];    ba= [20.2 0; 0 20.2];        % Actuator
ca= [-1 0; 0 -1];          da= [0 0; 0 0];           % SIGN CHANGE
actua= ss(aa,ba,ca,da);                          % u1= δa, u2= δr
plant= ss(ap,bp,cp,dp);            % x1=beta, x2=phi, x3=p, x4=r
sys1 = series(actua,plant);                % y1=p, y2=r (degrees)
```

The washout filter will be incorporated in a two-input, two-output model, with the first input-output pair being a direct connection:

```
aw= [-1/τw];           bw= [0 1/τw];       % τw to be defined
cw= [0;-1];            dw= [1 0; 0 1];     % y1=p y2=washed-r
wash= ss(aw,bw,cw,dw);
sys2= series(sys1,wash);     % x1=wash, x2=beta,.., x6=ail, x7=rdr
```

The washout filter time constant is a compromise; too large a value is undesirable since the yaw damper will then interfere with the entry into turns. The following root-locus design plots can also be used to show that too small a value will reduce the achievable dutch roll damping (see Problem 4.4-3). The time constant is normally of the order of 1 s, and $\tau_W = 1.0$ s is used here.

Experience shows that the roll damping loop is the less critical loop, and it is conveniently closed first. The p/u_a transfer function is the same as (4.4-2) with an

additional pole at $s = -20.2$ and the static loop sensitivity changed to 119 (i.e., 20.2 times the original value of 5.91). The MATLAB commands to obtain a root-locus plot and to close the loop are:

```
[a,b,c,d]= ssdata(sys2);
k= linspace(0,.9,3000);
r= rlocus(a,b(:,1),c(1,:),0,k);
plot(r)                          % Roll channel root locus
grid on
axis([-12,1,-5,5])
```

Figure 4.4-6 is the root-locus plot for positive k_p. It shows that the feedback has had the desired effect of speeding up the roll subsidence pole, which moves to the left in the s-plane and eventually combines with the actuator pole to form a complex pair. The spiral pole (not visible) moves a little to the right toward the NMP zero at $s = 0.05$, and the dutch roll poles change significantly as they move toward the open-loop complex zeros. If the feedback gain is made too high in this design, it will be found to be excessive at lower angles of attack. Furthermore, a high value will simply cause the aileron actuators to reach their rate and deflection limits more rapidly, as they become less effective at the higher angles of attack. A feedback gain

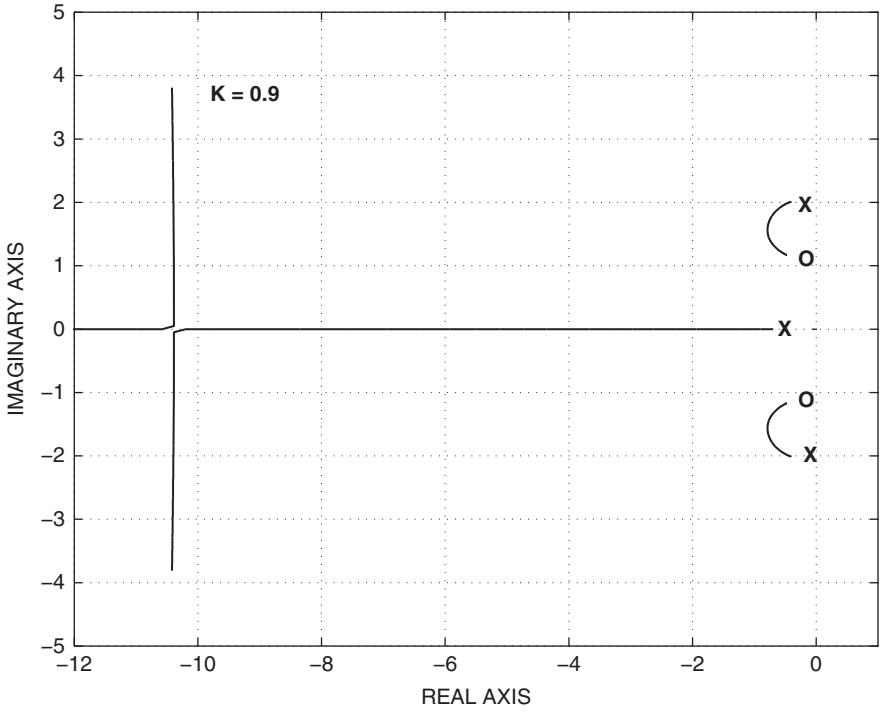

Figure 4.4-6 Root-locus plot for the roll damping loop.

of $k_p = 0.2$ puts the roll subsidence pole at $s = -1.37$, which is about twice as fast as the open-loop value. This is a suitable starting value for investigating the effect of closing the yaw damper loop:

```
acl1= a - b(:,1)*k_p*c(1,:);              % Close roll loop
[z,p,k1]= ss2zp(acl1,b(:,2),c(2,:),0)   % Yaw tr. fn. + wash
r= rlocus( acl1,b(:,2),c(2,:),0,k);
plot(r)                                   % Yaw channel root locus
```

The transfer function r_W/u_r (with $k_p = 0.2$) is

$$\frac{r_w}{u_r} = \frac{12.40s(s + 18.8)(s + 0.760)(s + 0.961 \pm j0.947)}{(s + 1)(s + 18.9)(s + 1.37)(s + 0.0280)(s + 20.2)(s + 0.752 \pm j1.719)} \quad (1)$$

A root-locus plot for closing the yaw-rate loop through the feedback gain k_r is shown in Figure 4.4-7. Although not shown in the figure, one of the actuator poles is effectively canceled by the zero at $s = -18.8$; the remaining actuator pole moves to the right to meet the roll pole and form a new complex pair. As the magnitude of k_r is increased, the spiral pole moves slightly closer to the washout zero at the origin, and the washout pole moves toward the zero at $s = -0.76$. At first the dutch roll poles

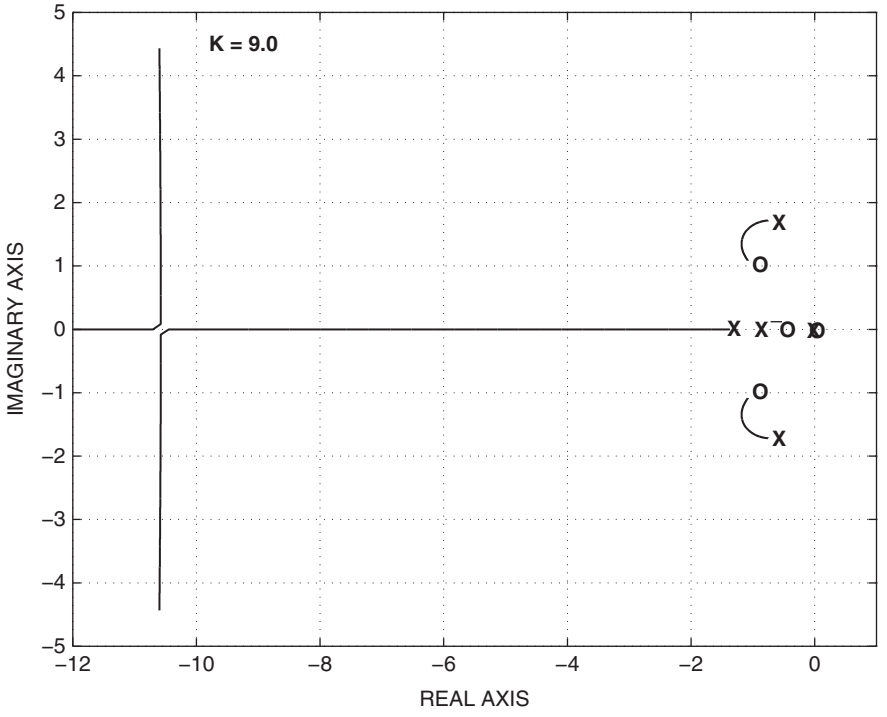

Figure 4.4-7 Root-locus plot for the yaw-rate loop.

move around an arc of constant natural frequency (approximately), and increasing damping ratio, toward the complex zeros. After k_r reaches about 3.5, the natural frequency begins to decrease and the damping ratio tends to remain constant. This feedback gain was considered to be the optimum value for the dutch roll poles, and so the yaw-rate loop was closed:

```
acl2= a - b*[.2 0; 0 3.5]*c;
[z,p,k1]= ss2zp(acl2,b(;,1),c(1,:),0)      % c.l. roll-rate t.f.
```

The principal transfer functions were found to be

$$\frac{p}{r_1} = \frac{119.4(\mathrm{s}+17.4)(\mathrm{s}-0.0502)(\mathrm{s}+3.74)(\mathrm{s}+0.262\pm \mathrm{j}0.557)}{(\mathrm{s}+18.7)(\mathrm{s}+17.7)(\mathrm{s}+0.0174)(\mathrm{s}+3.29)(\mathrm{s}+0.861)(\mathrm{s}+1.18\pm \mathrm{j}1.33)} \quad (2)$$

$$\frac{r}{r_2} = \frac{12.4(s+18.8)(s+1.00)(s+0.760)(s+0.961\pm j0.947)}{(s+17.7)(s+18.7)(s+3.29)(s+0.861)(s+0.0174)(s+1.18\pm j1.33)}, \quad (3)$$

where r_1 and r_2 are the roll-rate and yaw-rate reference inputs, as shown in Figure 4.4-4.

Transfer functions (2) and (3) show that the dutch roll poles and the washout pole (at $s = -0.861$) do not cancel out of the p/r_1 transfer function, so there is still strong coupling between the roll and yaw channels. The dutch roll natural frequency and damping ($\omega_n = 1.78$ rad/s, $\zeta = 0.67$) are now satisfactory, but the appearance of the relatively slow washout pole in the lateral dynamics may mean that the roll response is not much improved. Since we no longer have a simple dominant poles situation, a time response simulation is needed to assess the design. Before this is undertaken, the effect of a higher gain in the roll-rate loop will be considered.

If the roll-rate loop is closed, with $k_p = 0.4$, the roll subsidence pole moves out to $s = -3.08$, and the zero in the yaw-rate loop transfer function (1) moves from $s = -0.76$ to $s = -3.40$. This causes different behavior in the root-locus plot for the yaw-rate loop, as shown in Figure 4.4-8. The washout pole now moves to the left instead of the right. A comparison of Figures 4.4-7 and 4.4-8 shows that the price paid for this potential improvement in roll response is that the maximum dutch roll frequency is reduced. If the yaw-rate loop is closed with $k_r = 1.3$, to obtain the highest possible damped frequency for the dutch roll poles, the closed-loop transfer functions are

$$\frac{p}{r_1} = \frac{119.4(s+19.27)(s+1.74)(s-0.0507)(s+0.334\pm j0.787)}{(s+19.25)(s+17.4)(s+0.00767)(s+2.82)(s+1.57)(s+0.987\pm j0.984)} \quad (4)$$

$$\frac{r}{r_2} = \frac{12.40(s+1.00)(s+17.1)(s+3.40)(s+0.486\pm j0.459)}{(s+19.25)(s+17.4)(s+0.00767)(s+2.82)(s+1.57)(s+0.987\pm j0.984)} \quad (5)$$

The dutch roll frequency has decreased to $\omega_n = 1.39$ rad/s, and the damping has increased to $\zeta = 0.71$; these values still represent good flying qualities (see Table 4.3-6). An improvement in the roll response should have been obtained since the slow washout pole is nearly canceled by the zero at $s = -1.74$, and the roll

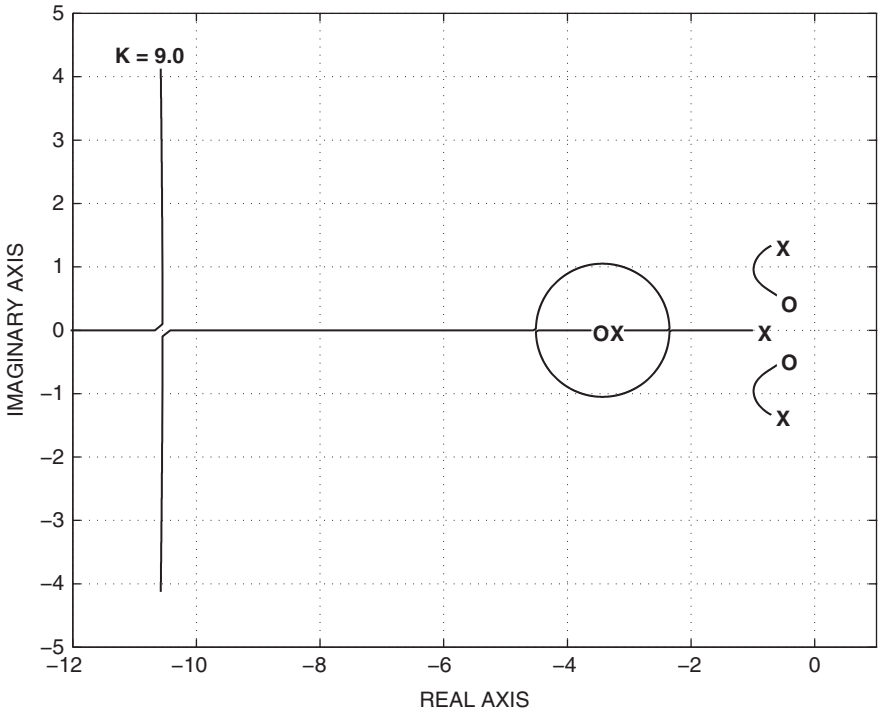

Figure 4.4-8 Alternate yaw-rate root locus.

subsidence pole (at $s = -2.82$) may now dominate the roll response. Note the way in which one actuator pole almost cancels out of each transfer function. Also, in the yaw-rate response, note the zero at $s = -1$ that originally canceled the washout pole. The transfer functions still show significant roll-yaw coupling.

The roll response of this design can only be assessed with a simulation, and because of the presence of the slow spiral pole in the transfer functions, a doublet pulse should be used as the input. The time responses were obtained by closing the yaw-rate and roll-rate loops with the feedback gains above ($k_p = 0.4, k_r = 1.3$) and using the following commands:

```
acl2= a - b*[.4 0; 0 1.3]*c;                % Close roll & yaw
t= [0:.02:10];                              % 501 points for plot
u= [-1.8*ones(1,51),1.8*ones(1,50),zeros(1,400)]'; % Doublet
[y,x]= lsim(acl2,b(:,1),c(1,:),0,u,t);      % Linear simulation
plot(t,y,t,u)
grid on
```

Figure 4.4-9 compares the roll-rate response of the open-loop dynamics (augmented with the actuators) with the closed-loop response. The doublet input is negative for 1 s, positive for 1 s, then zero, with unit amplitude in the open-loop case. In the

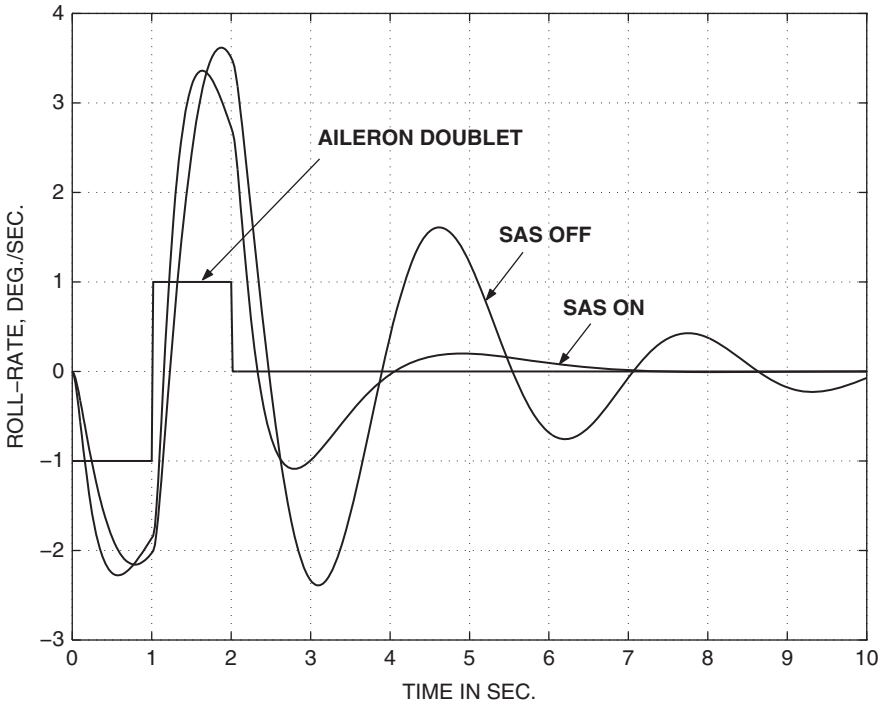

Figure 4.4-9 Roll-rate response to an aileron doublet.

closed-loop case the overall gain is different, and the doublet was adjusted to 1.8° so that the responses were of similar amplitude. The figure exhibits the major improvement in the dutch roll damping and the small but significant improvement in the roll-rate speed of response. ■

This example indicates the difficulties of multivariable design when significant cross-coupling is present in the dynamics. It also shows the difficulty of obtaining a good roll response at low dynamic pressure and high alpha. The design could be pursued further by investigating the effect of changing the washout time constant and using compensation networks, such as a phase lead, in the yaw-rate feedback loop. As pointed out earlier, increasing the bandwidth of the control loops may simply lead to saturation of the control surface actuators, and the limitations of the basic aircraft must be considered first.

4.5 CONTROL AUGMENTATION SYSTEMS

When an aircraft is under manual control (as opposed to autopilot control), the stability augmentation systems of the preceding section are, in most cases, the only automatic flight control systems needed. But in the case of high-performance military

aircraft, where the pilot may have to maneuver the aircraft to its performance limits and perform tasks such as precision tracking of targets, specialized CASs are needed. Flight control technology has advanced to the point where the flight control system (FCS) can provide the pilot with selectable "task-tailored control laws." For example, although the role of a fighter aircraft has changed to include launching missiles from long range, the importance of the classical dogfight is still recognized. A dogfight places a premium on high maneuverabilty and "agility" (ability to change maneuvers quickly) in the aircraft and a control system that allows the pilot to take advantage of this maneuverability. In this situation a suitable controlled variable for the pitch axis is the *normal acceleration* of the aircraft. This is the component of acceleration in the negative direction of the body-fixed z-axis. It is directly relevant to performing a maximum-rate turn and must be controllable up to the structural limits of the airframe or the pilot's physical limits. Therefore, for a dogfight, a "g-command" control system is an appropriate mode of operation of the flight control system. Other reasons for using this type of system will be described when we come to consider an example.

Another common mode of operation for a pitch-axis control augmentation system is as a pitch-rate command system. When a situation requires precise tracking of a target, by means of a sighting device, it has been found that a deadbeat response to pitch-rate commands is well suited to the task. Control of pitch rate is also the preferred system for approach and landing. Systems have been designed (Toles, 1985) which blend together the control of pitch rate and normal acceleration.

With respect to lateral-directional control, the most prevalent control augmentation system is a roll-rate command system. This system may be designed to roll the aircraft around its own velocity vector rather than the body axis. The reasons for this are described in the following sections.

Pitch-Rate Control Augmentation Systems

Figure 4.5-1 is a block diagram of a pitch-rate CAS. Type-0 control is not very satisfactory because the control inputs to the plant may be quite large (e.g., several degrees of elevator deflection) while the gains in the error channel are not usually very high

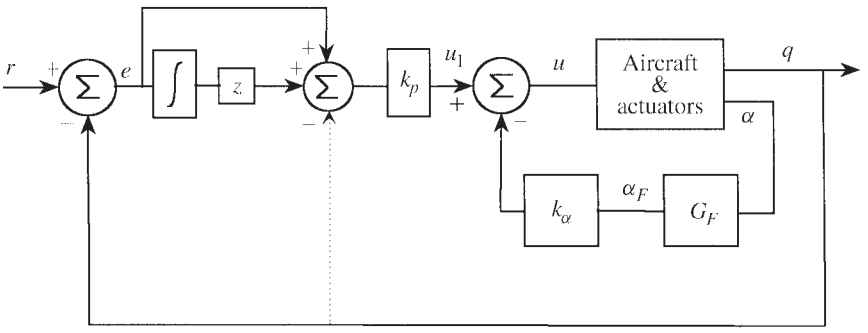

Figure 4.5-1 Pitch-rate control augmentation.

and entail large control errors. Therefore, proportional-plus-integral compensation is used to provide more precise control. Inner-loop alpha feedback is used, as in Example 4.4-1, when the pitch stiffness is inadequate.

The proportional path of the PI compensator can be replaced by an equivalent inner-loop pitch-rate feedback shown as a dotted line. This leaves the closed-loop poles unchanged but removes the PI zero from the closed-loop transfer function, thus reducing step-response overshoot [see Equation (3.9-24)]. It will be shown to be convenient to keep the PI zero while performing root-locus design.

The design of the pitch-rate CAS will now be illustrated by an example. It will be shown that the design can be performed on the short-period dynamics, but some caution must be used.

Example 4.5-1: A Pitch-Rate CAS Design The F-16 longitudinal dynamics corresponding to the nominal flight condition in Table 3.6-3 will be used once again. The A, B, C coefficient matrices are given in Example 4.4-1. These equations do not exhibit a short-period mode, but the α and q equations are only loosely coupled to v_T and θ and can be extracted as in Section 4.2. The final design will be verified on the complete dynamics. The elevator actuator and α-filter dynamics will be those used in Section 4.4, and a sign change will be incorporated at the actuator output.

The design procedure will be to close the alpha loop, then inspect the actuator to pitch-rate transfer function and choose a position for the PI zero that is likely to yield a satisfactory root-locus plot. This procedure will be illustrated by MATLAB statements.

We first define the plant matrices, cascade the actuator and filter, and close the alpha feedback loop:

```
ap=[-1.0189  0.90506; 0.82225   -1.0774];  % x1= alpha x2=q
bp=[-2.1499E-3; -1.7555E-1];               % Elevator input
cp=[57.29578 0;  0 57.29578];              % y1= alpha, y2= q
dp=[0 0];
sysp= ss(ap,bp,cp,dp);                     % Plant
sysa= ss(-20.2, 20.2, -1, 0);              % Actuator & SIGN CHANGE
[sys1]= series(sysa,sysp);                 % Actuator then Plant
sysf= ss(-10,[10 0],[1; 0],[0 0; 0 1]);    % Alpha Filter
[sys2]= series(sys1,sysf);                 % Actuator+Plant+Filter
[a b c d]= ssdata(sys2);                   % Extract a,b,c,d
acl= a - b*[kα 0]*c;                       % Close Alpha-loop
[z,p,k]= ss2zp(acl,b,c(2,:),0)             % q/u1 transf. fn.
```

The filter has been defined with two inputs and two outputs, and one input-output pair is a direct connection so that q is available as output 2. When the inner-loop feedback gain k_α is chosen, the zeros, poles, and gain of the q/u_1 transfer function will be calculated.

The final design will be relatively slow unless the integrator pole can be moved well to the left or made to coincide with a zero. Some trial designs show that this demands a smaller amount of alpha feedback than that used in Example 4.4-1; this will be demonstrated by comparing two different values of k_α.

Consider first the situation with $k_\alpha = 0.20$. The q/u_1 transfer function is then given by

$$\frac{q}{u_1} = \frac{203.2(s + 10.0)(s + 1.029)}{(s + 10.38)(s + 20.13)(s + 0.8957 \pm j1.152)}$$

The behavior of the outer-loop root locus with the added PI compensator can now be anticipated. As k_p is varied, the integrator pole will move toward the zero at –1.029; the compensator zero should be placed to the left of this zero, and the short-period poles will circle around the compensator zero. The following commands will add the PI compensator and plot the root loci:

```
sys3= ss(acl,b,c,[0;0]);              % Alpha-loop closed
sysi= ss(0,3,1,1);                    % PI= (s+3)/s
sys4= series(sysi,sys3);              % x1=alpha-f,,,x5= PI
[aa,bb,cc,dd]= ssdata(sys4);
k= linspace(0,.9,1000);
r= rlocus(aa,bb,cc(2,:),0,k);
plot(r)
axis=([-16,0,-8,8])
grid on
```

The root locus is shown in Figure 4.5-2 for a compensator zero at $s = -3.0$. When k_p reaches about 0.5, the filter and actuator poles form a second complex pair, the integrator pole has moved to $s = -0.91$, and the short-period poles are at $s = -3.2 \pm j3.4$. Increasing k_p causes the second complex pair to quickly become less damped, while the integrator pole moves only slightly farther left. If the amount of alpha feedback is reduced, the integrator pole can be moved closer to the zero at $s = -1.029$ before the second complex pole pair appears, while maintaining a satisfactory short-period pair.

The alpha feedback was eventually reduced to $k_\alpha = 0.08$, and the compensator zero was retained at $s = -3.0$ with the intention of causing the short-period poles to pass near $s = -4 \pm j3$ ($\omega_n = 5, \zeta = 0.8$). The root-locus plot was the same shape as Figure 4.5-2. With $k_p = 0.5$ the slow integrator pole reached $s = -1.02$ and stopped moving left, the short-period poles reached $s = -3.4 \pm j3$, and the actuator and filter poles were still short of combining to form a complex pair. The closed-loop (unity-feedback) transfer function was

$$\frac{q}{r} = \frac{101.6(s + 3.00)(s + 10.0)(s + 1.029)}{(s + 10.7)(s + 13.7)(s + 1.02)(s + 3.43 \pm j3.03)}$$

This was considered to be a promising design and the closed-loop step response was simulated with the following code:

```
acl2= aa- bb*0.5*cc(2,:);             % close outer loop
sys= ss(acl2,0.5*bb,cc(2,:),0);       % unity feedback
step(sys,3)
```

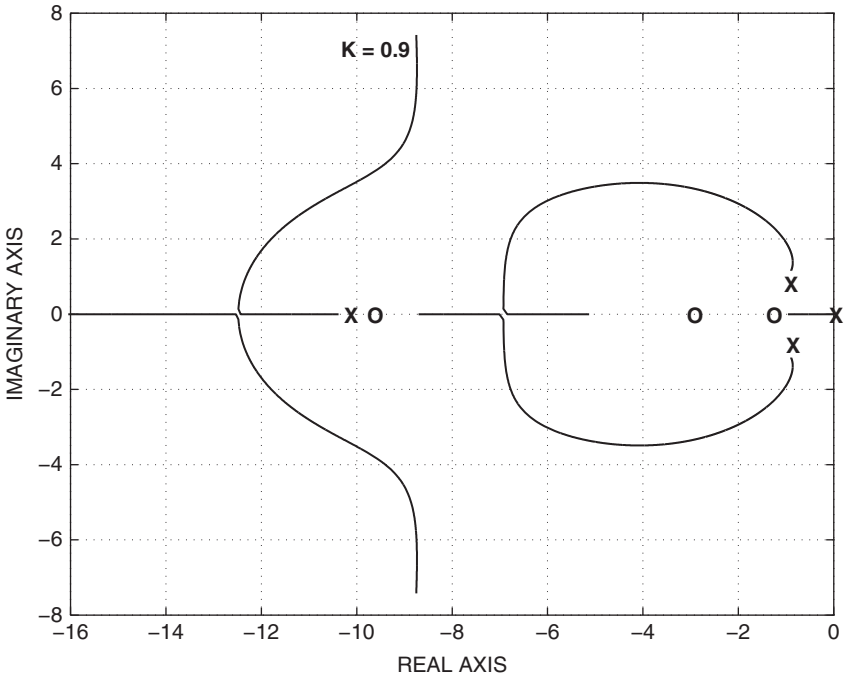

Figure 4.5-2 Root-locus plot for the pitch-rate CAS.

Figure 4.5-3 shows the step response. This response has a fast rise time and a large overshoot (almost 20%) and does not satisfy the "deadbeat" requirement. The other curve shows the pitch-rate step response when the compensator zero is removed. The rise time is now longer, but the settling time is about the same and the overshoot is only about 2%. This is potentially a good design, and we will move on to apply the same feedback gains to the complete longitudinal dynamics.

When the feedback gains $k_\alpha = 0.08$ and $k_p = 0.5$ are used on the full dynamics given in Example 4.4-1, the closed-loop transfer function is

$$\frac{q}{r} = \frac{304.8(s + 10.0)(s + 1.027)(s + 0.02174)s}{(s + 10.75)(s + 13.67)(s + 1.016)(s + 3.430 \pm j3.032)(s + 0.02173)s}$$

Observe that this transfer function contains the subset of poles and zeros given by the short-period approximation and the phugoid mode has degenerated to two real poles with this small amount of alpha feedback. Also, the phugoid poles are canceled by zeros and so would play no part in the pitch-rate response in this case.

This example illustrates some of the features of a pitch-rate CAS. An actual design can only be optimized by careful comparison with the flying qualities

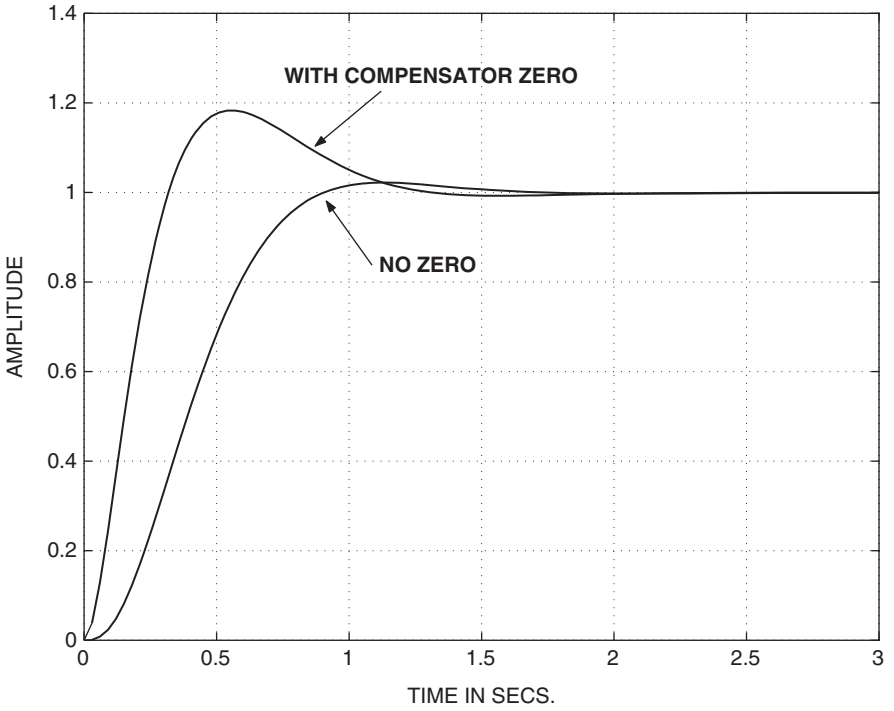

Figure 4.5-3 Step response of the pitch-rate CAS.

requirements, piloted simulation, and flight test. During the design process nominal designs must be performed at several points throughout the speed-altitude envelope, and the feedback gains will be a function of some "scheduling" parameters, such as dynamic pressure. ■

Normal Acceleration Control Augmentation Systems

In a fighter aircraft, if an accelerometer is placed close to the pilot's station, aligned along the body z-axis, and used as the feedback sensor for control of the elevator, the pilot has precise control over his z-axis g-load during high-g maneuvers. If 1 g is subtracted from the accelerometer output, the control system will hold the aircraft approximately in level flight with no control input from the pilot. If the pilot blacks out from the g-load and relaxes any force on the control stick, the aircraft will return to 1 g flight. Other useful features of this system are that the accelerometer output contains a component proportional to alpha and can inherently stabilize an unstable short-period mode, and the accelerometer is an internal sensor that is less noisy and more reliable than an alpha sensor.

Section 1.5 shows that the acceleration at a position P (the pilot's station here) is related to the acceleration at another fixed point (the aircraft cm) in the rigid aircraft, frame b, by a transport acceleration equation:

$$\mathbf{a}_{p/i} = \mathbf{a}_{cm/i} + \dot{\boldsymbol{\omega}}_{b/i} \times \mathbf{r}_{p/cm} + \boldsymbol{\omega}_{b/i} \times (\boldsymbol{\omega}_{b/i} \times \mathbf{r}_{p/cm})$$

where $\mathbf{r}_{P/cm}$ is the accelerometer position vector from the cm. If the accelerometer is on the aircraft longitudinal axis (x-axis) and aligned parallel to the z-axis, "positive up," then the *normal acceleration* is

$$a_n \equiv -\mathbf{a}^z_{P/i} = -(\mathbf{a}^z_{cm/i} - \dot{Q}x_a + PRx_a) \tag{4.5-1a}$$

where the z superscript indicates the *frd* z-component and x_a is the *frd* x-position of the accelerometer. In a wings-level pull-up only the first two terms on the right-hand side are nonzero. In turning flight, the next subsection shows that a fighter aircraft control system should be designed to roll the aircraft around the x stability axis, and then $PR{=}P^2 \tan \alpha$. Therefore, if the aircraft is rolled rapidly at high alpha, the PR term can be quite large and contributes negatively to the normal acceleration, as the aircraft nose moves along a circular arc around the x stability axis. Here, we will only illustrate the wings-level case.

In the real aircraft a_n must be obtained from the specific force sensed by an accelerometer, and is given by (see Chapter 1 Section Geodesy, Coordinate Systems, Gravity)

$$a_n = f_n + (-G_D^{ned} \cos\theta \cos\phi) \tag{4.5-1b}$$

If we define $n_z{=}\, a_n/g_D$ as the normal acceleration in g units, the ratio $|\mathbf{G}|/g_D$ is very close to unity, and

$$n_z \approx f_n - \cos\theta \cos\phi \qquad g - \text{units} \tag{4.5-1c}$$

In level flight, at small angles of attack, the feedback signal for the control system is

$$n_z \approx f_n - 1.0 \qquad g - \text{units} \tag{4.5-1d}$$

so this normal acceleration is approximately zero in steady level flight; it is often called the "incremental" normal acceleration.

If Equation (4.5-1a) is included in the nonlinear aircraft model, numerical linearization will yield a linear equation for a_n as a perturbation from its near-zero steady level flight value. A linear equation can also be obtained algebraically by finding the increment in the aerodynamic and thrust forces due to perturbations in the state and control variables, and this involves the Z-derivatives (see, for example, McRuer et al., 1973). For the nonlinear F-16 model numerically linearized at the nominal level flight condition in Table 3.6-3, the output equation for normal acceleration at the cg ($x_a = 0$) is found to be

$$a_n = 0.003981 v_T + 15.88\alpha + 1.481 q + 0.03333\delta_e, \tag{4.5-2}$$

where α and q are in radians and δ_e is in degrees.

The normal acceleration in (4.5-2) depends on v_T, α, and q (the quantities that define the longitudinal aerodynamic forces) and on elevator deflection, which produces aerodynamic forces directly. This direct-feed term was also noted in Example 3.7-2 and leads to a transfer function of relative degree zero. Note that a_n is insensitive to the pitch attitude when θ is small.

The elevator-to-normal-acceleration transfer function corresponding to (4.5-2) can be found from the Jacobian matrices and is

$$\frac{a_n}{\delta_e} = \frac{0.03333(s - 0.003038)(s + 0.01675)(s + 6.432)(s - 13.14)}{(s - 0.09756)(s + 1.912)(s + 0.1507 \pm j0.1153)} \tag{4.5-3}$$

This transfer function has the same poles that were noted in Example 4.4-1. Because of the NMP zero at $s = 13.14$, the normal acceleration response to a negative step elevator command (aircraft nose-up) will be an initial negative acceleration, quickly followed by the expected positive normal acceleration.

The physical explanation for the NMP behavior is that when the elevator control surface is deflected trailing edge upward to produce a positive normal acceleration, this creates a downward increment of force on the tail. The result is that the cg of the aircraft may drop momentarily during the pitch-up, so the normal acceleration may briefly become negative before it builds up positively. At the pilot's station ahead of the cg, the normal acceleration also depends on the pitch angular acceleration about the cg, so only a positive normal acceleration may be felt in a pitch-up. Table 4.5-1 shows the elevator-to-normal-acceleration transfer function zeros for a range of accelerometer positions, from the cg forward. The zeros close to the origin do not change significantly from the positions given in (4.5-3), and only the static loop sensitivity and the remaining zeros are shown.

Table 4.5-1 shows that as the accelerometer position is moved forward, the NMP zero moves out toward infinity and the static loop sensitivity decreases, thus keeping the transfer function dc gain constant. Eventually the static loop sensitivity changes sign and a zero comes in from infinity along the negative real axis, finally combining with the other real zero to form a complex pair. At a position near 6.1 ft forward of the cg the NMP effect disappears, and this point corresponds to an "instantaneous center of rotation" when an elevator input is suddenly applied. Note that in the case

TABLE 4.5-1 Transfer Function Zeros versus Accelerometer Position

x_a (ft)	Static Loop Sensitivity and Numerator Factors
0	0.03333 $(s + 6.432)$ $(s - 13.14)$
5	0.006042 $(s + 9.171)$ $(s - 50.82)$
6	0.0005847 $(s + 10.68)$ $(s - 450.7)$
6.1	0.00004005 $(s + 10.90)$ $(s - 6448.2)$
7	−0.004872 $(s + 14.73)$ $(s + 39.23)$
15	−0.04852 $(s + 3.175 \pm j6.925)$

of the real F-16 aircraft, the pilot's station is approximately 15 ft ahead of the cg and is therefore not close to the instantaneous center of rotation.

It is also important to place the accelerometer close to a node of the most important fuselage bending mode. If this is not done, structural oscillations will be coupled into the rigid-body control system and may degrade the handling qualities or even lead to an "aeroservoelastic" limit cycle oscillation (see, e.g., AFWAL-TR-84-3105). Inevitably, the design of a normal acceleration control system to achieve good handling qualities is difficult and can require a good deal of refinement based on flight test results. A control system that has a good normal acceleration step response may have a pitch-rate response with a very large overshoot, and conversely, a reduction in the pitch-rate overshoot may lead to a sluggish normal acceleration response. The C^* criterion is appropriate for initial evaluation of the control system, since it is based on a blend of normal acceleration at the pilot's station and pitch rate.

Finally, note that an accelerometer is an internal (within the fuselage) sensor, with higher reliability and lower noise than the external alpha sensor. However, both accelerometers and alpha sensors are typically employed on modern fighter aircraft, and this reduces the dependence on the alpha sensor. A disadvantage of normal acceleration feedback is that the gain of the transfer function (4.5-3) varies widely with dynamic pressure. Accelerometer noise may become a problem if, at low dynamic pressure, the gain has to be greatly boosted to achieve a desirable closed-loop response. We will now investigate the features of the normal acceleration CAS by means of a design example.

Example 4.5-2: A Normal Acceleration CAS Design The configuration shown in Figure 4.5-4 will be used. The dynamics will be the same as Example 4.5-1, but an output equation for normal acceleration must be determined. Therefore, using numerical linearization of the F-16 model with the accelerometer 15 ft forward of the cg (i.e., at the pilot's station) and the nominal flight condition from Table 3.6-3, the output equation is found to be

$$a_n = 0.0039813v_T + 16.262\alpha + 0.97877q - 0.048523\delta_e \tag{1}$$

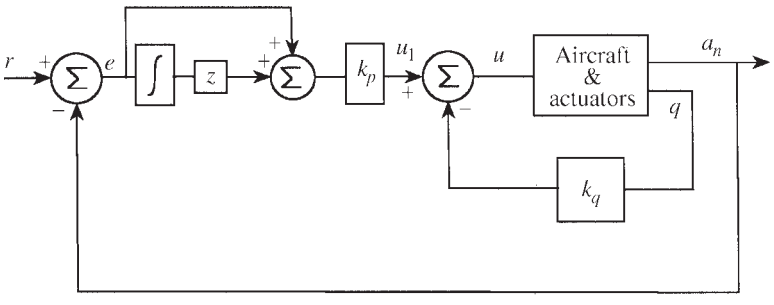

Figure 4.5-4 Normal acceleration control augmentation.

In (1) the dependence on v_T is quite weak, so the states V_T and θ will be dropped, with the final results checked on the complete dynamics. The MATLAB commands to cascade the actuator with the plant and close the pitch-rate loop are:

```
ap=[-1.0189  0.90506;  0.82225  -1.0774];  % x1= alpha x2=q
bp=[-2.1499E-3; -1.7555E-1];               % Elevator input
cp=[0  57.29578; 16.262  0.97877];         % y1=q y2= an
dp=[0; -0.048523];
sysp= ss(ap,bp,cp,dp);                     % Plant
sysa= ss(-20.2, 20.2, -1,0);               % Actuator, SIGN CHANGE
[sys1]= series(sysa,sysp);                 % Actuator then Plant
[a,b,c,d]= ssdata(sys1);                   % a_n/u transfer fn.
acl= a - b*[0.4 0]*c;                      % Close q loop
[z,p,k]= ss2zp(acl,b,c(2,:),d)             % a_n/u_1 transfer fn.
```

The plant transfer function from elevator actuator input to normal acceleration is found to be

$$\frac{a_n}{u} = \frac{.9802(s + 3.179 \pm j6.922)}{(s + 20.20)(s + 1.911)(s + 0.1850)} \tag{2}$$

The effect of the inner-loop pitch-rate feedback is to speed up the two slow poles, and at quite low gain the pole from $s = -1.911$ combines with the actuator pole to form a complex pair. Speeding up these poles is desirable for a fast time response, but as noted previously, the amount of pitch-rate feedback is limited by practical considerations (pickup of structural noise). The value $k_q = 0.4$ (degrees of elevator deflection per degree per second of pitch rate) is in line with our past experience (0.25 to 0.5) and leads to the following closed-loop transfer function:

$$\frac{a_n}{u_1} = \frac{0.9802(s + 3.179 \pm j6.922)}{(s + 13.78)(s + 7.661)(s + 0.8601)} \tag{3}$$

The outer-loop root locus with the added PI compensator can now be anticipated. The compensator pole (at $s = 0$) will combine with the pole at $s = -0.8601$ to form a complex pair, and these poles will move toward the complex zeros of (3). This behavior will be modified depending on the position of the compensator zero. If the compensator zero is well to the left of $s = -0.8601$, these branches will be deflected only slightly to the left before landing on the complex zeros. At the same time the pole at $s = -7.661$ will move toward the compensator zero, creating a potential slow-pole problem. The complex zeros are not well damped and it is difficult to achieve fast, well-damped, complex poles together with a fast real pole.

The alternative is to place the compensator zero close to the pole at $s = -0.8601$ so that this pole is effectively canceled. The loci for the short-period poles will then break away from the real axis somewhere closer to the pole at $s = -7.661$ before proceeding to the complex zeros. Some trial and error shows that this approach leads to a better time response, and it will be followed here. In practice, the sensitivity of the poles to gain variations, noise pickup, and possible advantages of additional compensator poles and zeros would have to be considered.

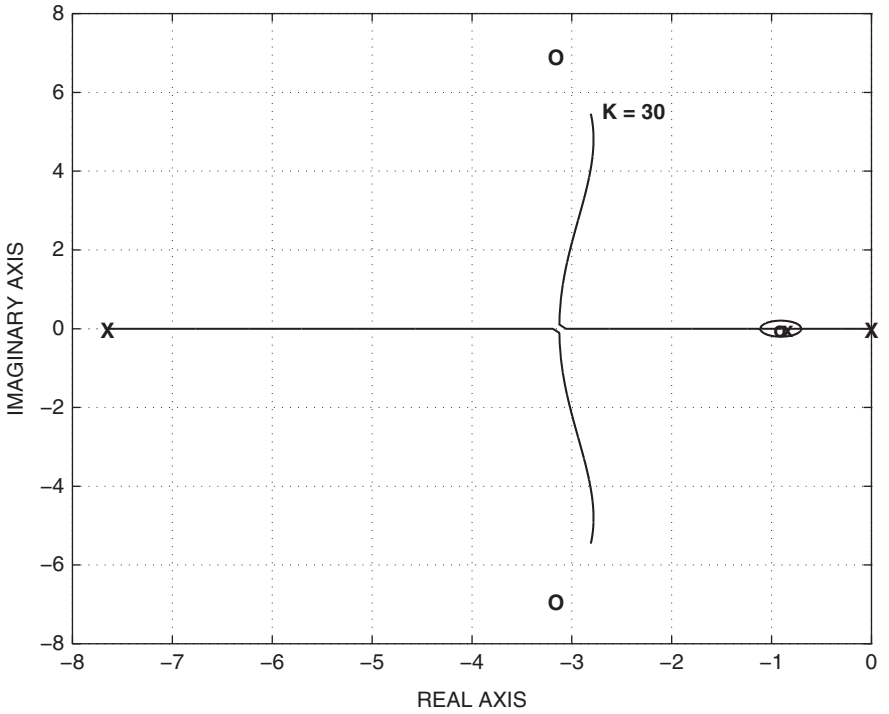

Figure 4.5-5 Root-locus plot for the normal acceleration CAS.

Figure 4.5-5 shows the outer-loop root locus (i.e., k_p varied) when the PI compensator zero is placed at $s = -0.9$ (to demonstrate that exact cancellation is not required). The effect of the imperfect cancellation is visible near $s = -0.9$, and the locus of the short-period poles shows that satisfactory damping and natural frequency can be achieved without the use of an additional lead compensator.

The short-period poles should be made well damped because the compensator zero can be anticipated to cause an overshoot in the closed-loop step response. When the root locus is calibrated with a few values of k_p, a value $k_p = 5$ puts the short-period poles at $s = -3.00 \pm j2.18$ ($\omega_n = 3.7, \varsigma = 0.81$). The closed-loop transfer function is then

$$\frac{a_n}{r} = \frac{4.901(s + 0.9000)(s + 3.179 \pm j6.922)}{(s + 20.28)(s + 0.9176)(s + 3.000 \pm j2.180)} \tag{4}$$

Figure 4.5-6 shows the closed-loop step response corresponding to this transfer function and the normalized C^* response. The a_n response is fast and well damped; the initial rate of rise is particularly fast because of the pitch acceleration component of the response. The rate limitations of the elevator actuator would modify this response slightly. The associated pitch-rate response (not illustrated) shows an overshoot of approximately 100%, but the C^* response falls almost exactly in the middle

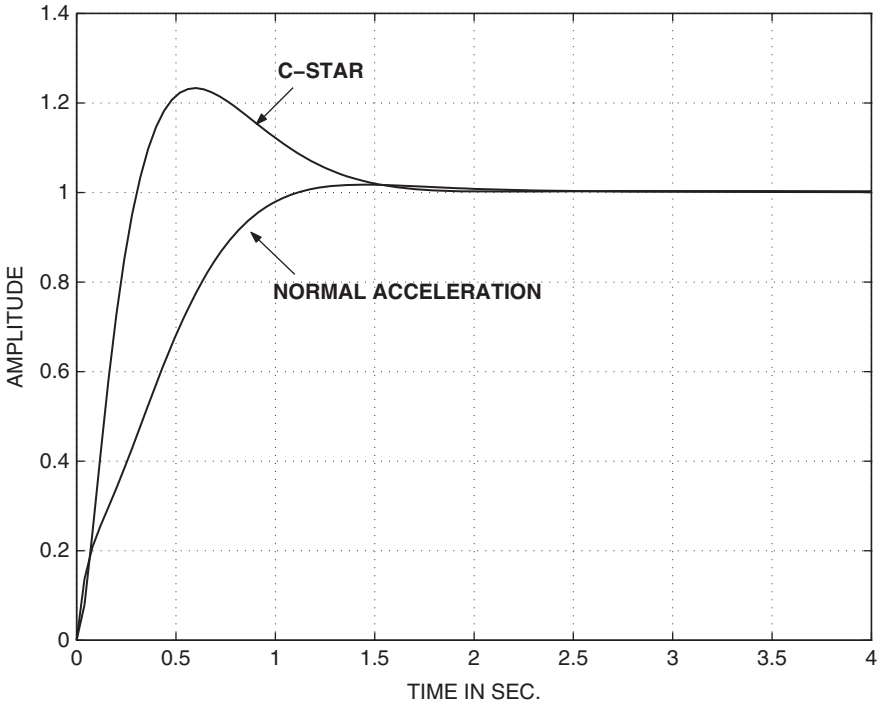

Figure 4.5-6 Normal acceleration CAS; step and C-star responses.

of the level-1 envelope (see Section The Handling Qualities Requirements). The C^* values were computed by adding the component $12.4q$ to the normal acceleration output equation in the closed-loop Jacobian matrices. An initial time-response run was performed so that the steady-state value of C^* could be determined for use in normalizing the response.

The closed-loop transfer function obtained by applying the same feedback gains to the complete longitudinal dynamics (i.e., phugoid included) is

$$\frac{a_n}{r} = \frac{4.901(s+0.900)(s+3.175 \pm j6.925)(s+0.01685)(s-0.003139)}{(s+20.28)(s+0.9194)(s+3.000 \pm j2.186)(s+0.01637)(s-0.003219)} \tag{5}$$

Notice that this transfer function contains, to a very good approximation, the poles and zeros of (4), thereby justifying the use of the short-period approximation. In (5) the phugoid mode is degenerate (two real poles) and one pole is unstable, whereas in Section 4.4 a stable phugoid was achieved with the basic stability augmentation system. This is because the normal acceleration equation (1) contains a component due to v_T, and this component is being fed back in a positive sense (positive δ_e gives positive v_T). The phugoid mode is almost canceled by the transfer function zeros in this case, and the unstable pole is very slow. An unstable phugoid pole is probably immaterial in this flight control (dogfight) mode, but the instability could

be avoided by retaining some inner-loop alpha feedback and using less gain in the normal acceleration loop. An alternative possibility is to modify the feedback signal by subtracting $\cos\theta\cos\phi$ from the accelerometer output, as in (4.5-1*b*), to remove the gravity component. If this is done, the feedback signal will contain a θ-component that will be in the correct sense to provide a stabilizing effect on the phugoid mode. This control system would hold a steady climb or dive with no control stick deflection and needs little input in a coordinated turn. It would probably prove objectionable to pilots. ■

Lateral-Directional Control Augmentation

The roll/yaw stability augmentation system described in Section 4.4 is adequate for most aircraft, but for aircraft that must maneuver rapidly at high angles of attack, a more refined lateral-directional control augmentation system is required. The lateral aerodynamic control surfaces (ailerons and differential elevator) tend to cause the aircraft to roll about its longitudinal axis, and at high alpha, this can lead to some highly undesirable effects.

Consider the effect of a rapid 90° body-axis roll at high alpha. It is easy to visualize that the angle of attack will be converted immediately, and almost entirely, to a sideslip angle. This is referred to as *kinematic coupling* of alpha and beta. Because of this rapid elimination of the angle of attack, the body-axis roll is counterproductive. The most important purpose of a roll is to initiate a turn, which is then achieved by using angle of attack to produce the lift that will subsequently generate the required centripetal acceleration.

The sideslip created by kinematic coupling is referred to as *adverse sideslip* because it will tend to oppose the roll (remember that C_{l_β} is normally negative; a right roll will generate positive beta through kinematic coupling and hence a negative rolling moment). The sideslip will exist until the aircraft has yawed into the wind once more, and then if the angle of attack must be reestablished, the result will be an inefficient turn entry. Most modern fighters therefore use automatic control systems designed to roll the aircraft about the stability x-axis, thus maintaining the initial angle of attack.

Finally, large sideslip angles are undesirable for several important reasons. The effectiveness of the aerodynamic control surfaces may be greatly reduced; directional stability may be lost so that, in some cases, aircraft have been known to "swap ends" in flight. Even if directional stability is maintained, a large sideforce can be developed that may possibly break the vertical tail.

Another important effect that occurs during a roll is *inertia coupling*. Suppose that the aircraft has been designed to roll around the stability x-axis with no sideslip. Then the transformations in Section 2.3 can be used to determine the body-axes roll and yaw rates that result in a stability-axes roll rate P_s with zero yaw rate R_s. The relevant equations are

$$P_s = P\cos\alpha + R\sin\alpha \tag{4.5-4a}$$

$$0 = R_s = -P\sin\alpha + R\cos\alpha \tag{4.5-4b}$$

or

$$R = P \tan \alpha \tag{4.5-4c}$$

When alpha is positive, R and P must have the same sign, and if alpha is large, body-axes yaw rates comparable to the body-axes roll rate must be generated. Therefore, in a rapid high-alpha roll, gyroscopic (inertia coupling) effects will generate a significant body-axes pitching moment. Euler's equations of motion (1.5-6) illustrate the inertia coupling effects when the cross-products of inertia can be neglected. Using these equations, the pitching moment, M_{IC}, due to inertia coupling is given by

$$M_{IC} = \dot{Q} J_Y = (J_Z - J_X) PR \tag{4.5-5}$$

For modern fighter aircraft with stubby wings and engine(s) on or near the longitudinal axis, the moment of inertia, J_X, is usually small compared to J_Z (while J_Z and J_Y are comparable in magnitude). Therefore, a rapid roll (right or left) about the stability x-axis, at large positive alpha, can produce a strong nose-up pitching moment. To avoid a "pitch departure," the pitch-axis control augmentation system must cause the horizontal tail to generate an opposing aerodynamic moment. At high alpha it may be difficult to obtain the neccessary aerodynamic pitching moment because of the horizontal-tail stalling. Even when adequate pitching moment is available, the required yawing moment may be unachievable because the rudder is blanketed by the wings. Conventional aircraft therefore have greatly degraded roll response at high alpha, and furthermore, the control systems must often be designed to limit the commanded roll rate to avoid a pitch departure.

Figure 4.5-7 illustrates the essential features of a lateral-directional CAS for a modern fighter aircraft; compensation networks, limiters, and so on, are added as necessary. The aileron control channel is the same as that shown in Figure 4.4-4 for the lateral-directional SAS, except that the aileron-actuator input now has a cross-connection to the rudder actuator via an alpha-dependent gain (also Mach dependent in general). This cross-connection, known as the *aileron-rudder interconnect* (ARI), may be implemented hydromechanically on some aircraft or electrically on others. Its purpose is to provide the component of yaw rate necessary to achieve a stability-axis roll.

The ARI gain must be determined, as a function of alpha and Mach number, to achieve the exact amount of yaw rate required to satisfy the constraint equation (4.5-4c). The gain is typically estimated from the known aerodynamic data and adjusted using nonlinear simulation. We can avoid this by incorporating the constraint $R = P \tan \alpha$ in our steady-state trim program and trimming the aircraft for a "steady-state" roll (see Chapter 3 Section Steady-State Flight). Table 4.5-2 shows an abridged set of trim data for different roll rates and two different pitch rates; the angular units are all in degrees. The trim program has driven the lateral acceleration a_y (along the body y-axis) to essentially zero (about $10^{-6} g$s) with a small sideslip angle.

The table shows that angle of attack is almost independent of the roll rate, but it is dependent on pitch rate. Therefore, the second half of the table is for a pitch

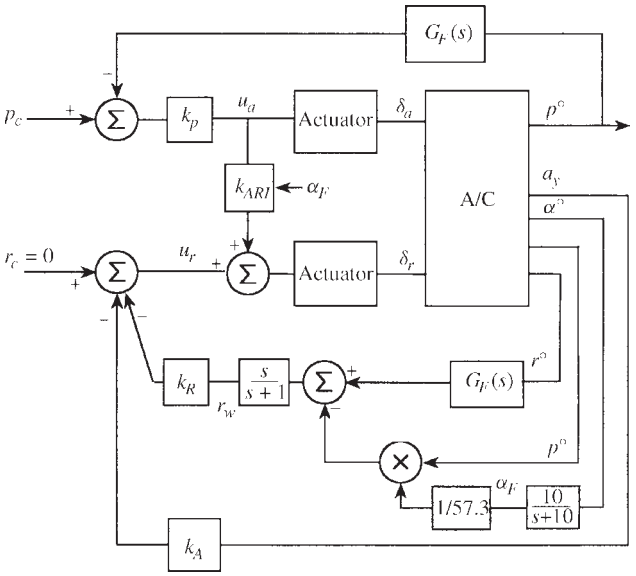

Figure 4.5-7 A lateral-directional CAS.

TABLE 4.5-2 Trim Conditions for Determining ARI Gain

$cg = 0.35\overline{c}$, $V_T = 502$, $h = 0$, $\overline{q} = 300$, $M = 0.450$

	P	α	β	a_y	aileron	rudder	rdr/ail
	10	2.12	−0.012	0	−0.813	0.269	−0.331
	20	2.12	−0.023	0	−1.63	0.537	−0.329
	45	2.15	−0.050	0	−3.66	1.20	−0.328
$Q = 0$	60	2.17	−0.065	0	−4.88	1.60	−0.328
	90	2.22	−0.091	0	−7.32	2.38	−0.325
	120	2.28	−0.112	0	−9.76	3.14	−0.322
	180	2.39	−0.139	0	−14.6	4.63	−0.317
	10	6.53	0.012	0	−0.835	−0.0948	0.114
	20	6.52	0.022	0	−1.67	−0.195	0.117
$Q = 5$	45	6.46	0.046	0	−3.76	−0.445	0.118
	60	6.41	0.058	0	−5.01	−0.595	0.119
	90	6.28	0.071	0	−7.52	−0.897	0.119
	180	5.87	0.048	0	−15.0	−1.83	0.122

rate of 5 deg/s and serves to provide data for a higher alpha condition (6.5°). Pitch rates of 10, 15, and 20 deg/s were used to provide additional data; maximum engine thrust is reached in between the last two conditions. The table indicates that for a stability-axis roll under the conditions shown (i.e., $M = 0.45$, etc.), the required ratio of rudder deflection to aileron deflection is −0.33 at $\alpha = 2.2°$ and 0.12 at $\alpha = 6.5°$.

Using the additional data for other angles of attack showed that the ratio of rudder to aileron deflection, k_{ARI}, was a good fit to the straight line:

$$k_{ARI} = 0.13\alpha - 0.7, \quad (\alpha \text{ in degrees}) \tag{4.5-6}$$

In a practical design the effect of Mach number must also be determined, and a two-dimensional lookup table might be constructed for k_{ARI}. Because of time and space limitations, (4.5-6) will be used here, and the design example will not involve large variations of Mach number.

The ARI alone would be an open-loop attempt to achieve a stability-axis roll and, to improve on this, feedback control is used to drive the lateral acceleration to zero (as in Table 4.5-2). Figure 4.5-7 shows how lateral acceleration is fed back and compared with a null reference input, and the error signal is used to drive the rudder actuator. This is also known as a *turn coordination* scheme and can be used in autopilot systems to respond to radio navigation steering signals or relieve the pilot of the need to coordinate turns.

Like the normal acceleration CAS, lateral acceleration feedback suffers from a wide variation of sensitivity. High values of feedback gain are needed at low speed, and this may cause problems with accelerometer noise. At low speed ($M < 0.3$) sideslip angle feedback is normally used instead of lateral acceleration but has the disadvantage that a beta sensor is less reliable than an accelerometer.

The inner feedback loop in the rudder channel provides dutch roll damping by feeding back an approximation to the stability-axis yaw rate [Equation (4.5-4*b*)] to the rudder. Thus, the filtered alpha signal, converted to radians (as necessary), is used as an approximation to $\sin\alpha$ multiplied by the roll rate and subtracted from the yaw rate. The stability-axis yaw rate is washed out so that it operates only transiently and does not contribute to a control error when a steady yaw rate is present. Note that, according to (2.5-29), the yaw-rate feedback is equivalent to a combination of beta and beta-dot feedback.

When necessary the pilot can still sideslip the airplane, because rudder inputs are applied directly to the rudder actuator. The control system will tend to reject this disturbance input, so the desirable effect of limiting the sideslipping capability will be achieved.

A practical lateral-directional CAS, based on the concept above, will be a complex system involving gain scheduling (with angle of attack and dynamic pressure or Mach), multipliers and limiters, and discrete switching (to change the control laws automatically at the alpha limits). It is a particularly good illustration of the fact that aircraft control systems incorporate many nonlinear and time-varying effects and the "tuning" of a design is often done by trial and error using computer simulation as a tool together with piloted simulation and flight tests. An example of a lateral-directional CAS design based on Figure 4.5-7 will now be given.

Example 4.5-3: A Lateral-Directional CAS Design This design will be performed on the F-16 model in the nominal flight condition of Table 3.6-3 (level flight at sea level, $\alpha = 2.115°$) and will follow Figure 4.5-7. The lateral accelerometer is at

the aircraft cg, and the coefficient matrices found by linearizing the aircraft model lateral-directional dynamics are, in MATLAB format,

```
ap= [-3.2201E-01  6.4040E-02  3.6382E-02  -9.9167E-01;   % x1=β
      0.0         0.0         1.0          3.6928E-02;   % x2=φ
     -3.0649E+01  0.0        -3.6784E+00   6.6461E-01;   % x3=p
      8.5395E+00  0.0        -2.5435E-02  -4.7637E-01 ]; % x4=r
bp= [ 2.9506E-04    8.0557E-04;
      0.0           0.0;                        % input-1 = δa
     -7.3331E-01    1.3154E-01;                 % input-2 = δr
     -3.1865E-02   -6.2017E-02 ];
cp= [-5.0249E+00  0.0    -8.1179E-03   1.1932E-01;    % y1= ay
      0.0         0.0     5.7296E+01   0.0;           % y2= p
      0.0         0.0     0.0          5.7296E+01 ];  % y3= r
dp= [ 4.6043E-03  1.2571E-02;
      0.0         0.0;
      0.0         0.0 ];
```

The control surface actuator dynamics will be the same as Example 4.4-3. The filtered alpha signal is fixed at the trim value, and ARI and roll-rate feedback equations are linearized around this value:

```
kari=.13*2.115 -0.7;
aa= [-20.2 0; 0 -20.2];             % Two Actuators
ba= [20.2 0; 20.2*kari 20.2];       % Inp-1= Ail., Inp-2=ARI & rdr
ca= [-1 0; 0 -1]; da= [0 0; 0 0];   % SIGN CHANGE in C
actua= ss(aa,ba,ca,da);
plant= ss(ap,bp,cp,dp);             % x1=beta, x2=phi, x3=p, x4=r
sys1 = series(actua,plant);         % x5= aileron x6= rudder
```

The washout filter has a time constant of 1 s and is included in a three-input, three-output state-space model with direct connections for the p and a_y signals. This model is cascaded at the output of the plant:

```
km= 2.115/57.3;                 % Multiply p by alpha in rads.
aw= [-1]; bw= [0 -km 1];        % Washout filter
cw= [0; 0;-1];                  % outputs ay,p,rw
dw= [1 0 0; 0 1 0; 0 -km 1];    % inputs ay,p,r
wash= ss(aw,bw,cw,dw);
sys2= series(sys1,wash);        % x1=wash x2=beta, etc
[a,b,c,d]= ssdata(sys2);        % Complete augmented system
```

The ARI affects only the B-matrix, and when the poles and zeros of the principal transfer functions are checked, it is found, as expected, that the effect of the ARI is to move only the zeros of transfer functions from the u_a input. The open-loop transfer function from actuator input to roll rate, with the ARI connected, is given by

$$\frac{p}{u_a} = \frac{913.4(s + 0.4018 \pm j2.945)(s - 0.002343)}{(s + 0.4235 \pm j3.064)(s + 3.616)(s + 0.01433)(s + 20.20)} \tag{1}$$

The roll subsidence pole is at $s = -3.615$, the spiral pole is stable at $s = -0.01433$, and the dutch roll poles are lightly damped and almost cancel out of this transfer function. Positive u_a inputs ($-\delta_a$) will initially produce a positive roll rate, and the "slow" NMP zero indicates that this will disappear as the spiral trajectory becomes established.

A root-locus plot for the roll-rate loop showed that the dutch roll poles moved toward the canceling zeros. The spiral pole moved toward the NMP zero at $s = 0.0023$, and the roll subsidence pole joined with the actuator pole to form a high-frequency complex pair whose damping decreased as the feedback gain was increased. A fast roll-rate response was desired so it was decided to allow this complex pair but keep them well damped. Roll-rate gains close to those used in Example 4.4-3 were tried and the gain $k_p = 0.2$ was chosen, which produced a damping ratio of about 0.7 for the complex pair and a stable spiral mode. The roll-rate loop was closed and the transfer function r_w/u_r was found with the following commands:

```
acl= a - b*[0  0.2  0; 0  0  0]*c;   % close roll loop
[z,p,k]= ss2zp(acl,b(:,2),c(3,:),0)  % rw/ur transf. fn.
```

giving

$$\frac{r_w}{u_r} = \frac{77.40s(s + 0.1030 \pm j0.2272)(s + 11.84 \pm j10.10)}{(s + 1)(s + 20.2)(s + 0.0027)(s + 0.4323 \pm j2.976)(s + 11.90 \pm j10.70)} \tag{2}$$

A root-locus plot for this loop shows that the dutch roll poles have their highest natural frequency and good damping when $k_r = 0.8$, and this gain was used as the initial gain for investigating the lateral acceleration feedback loop:

```
acl= a- b*[0  0.2  0;  0  0  0.8]*c;       % Close roll & yaw loops
[z,p,k]= ss2zp(acl,b(:,2),c(1,:),0)  % ay/uy transfer fn.
```

After removing an approximate cancellation of two complex pairs of poles and zeros, the lateral acceleration transfer function is

$$\frac{a_y}{r_c} = \frac{-0.2539(s + 1)(s - 4.157)(s + 4.00)(s - 0.0002)}{(s + 16.54)(s + 2.168)(s + 0.0026)(s + 1.701 \pm j1.486)} \tag{3}$$

The NMP zero at $s = 4.157$ is analogous to the NMP zero in the elevator-to-normal-acceleration transfer function. Ignoring for the moment the "slow" NMP zero at $s = 0.0002$, the Laplace transform final-value theorem shows that a positive-step r_c (negative rudder deflection) produces positive lateral acceleration, but the NMP zero at $s = 4.157$ indicates that this acceleration will initially be negative. The explanation is that negative rudder deflection immediately produces a negative sideforce contribution from the tail, but then, as negative sideslip builds up, the sideforce at the cg will become positive.

If the dihedral derivative is negative (positive stiffness), the aircraft will next begin to roll right, and negative sideforce will again occur as its weight starts a positive sideslipping motion. This is the cause of the "slow" NMP zero at $s = 0.0002$. The

purpose of the lateral acceleration feedback is to cancel the sideslip that is causing the short-term lateral acceleration, so lateral acceleration must be fed back negatively to u_r. The following commands will give the root-locus plot for the lateral acceleration feedback, with the roll- and yaw-rate loops closed:

```
k= linspace(0,100,2000);
r= rlocus(acl,b(:,2),c(1,:),0,k);
plot(r)
grid on
axis([-23.5,.5,-12,12)
```

The root-locus plot, Figure 4.5-8, shows that increasing the lateral acceleration feedback causes the dutch roll poles to circle around in the left-half s-plane, before terminating in the right-half plane on the NMP zero and at infinity. Increasing the inner-loop yaw-rate feedback causes the dutch roll poles to circle farther to the left in the s-plane and allows more lateral acceleration feedback to be used. However, using large amounts of lateral acceleration feedback creates a slow real pole by pulling the washout pole back to the right (it was moved left by the rate feedback) and makes the dutch roll pole positions quite sensitive to gain changes.

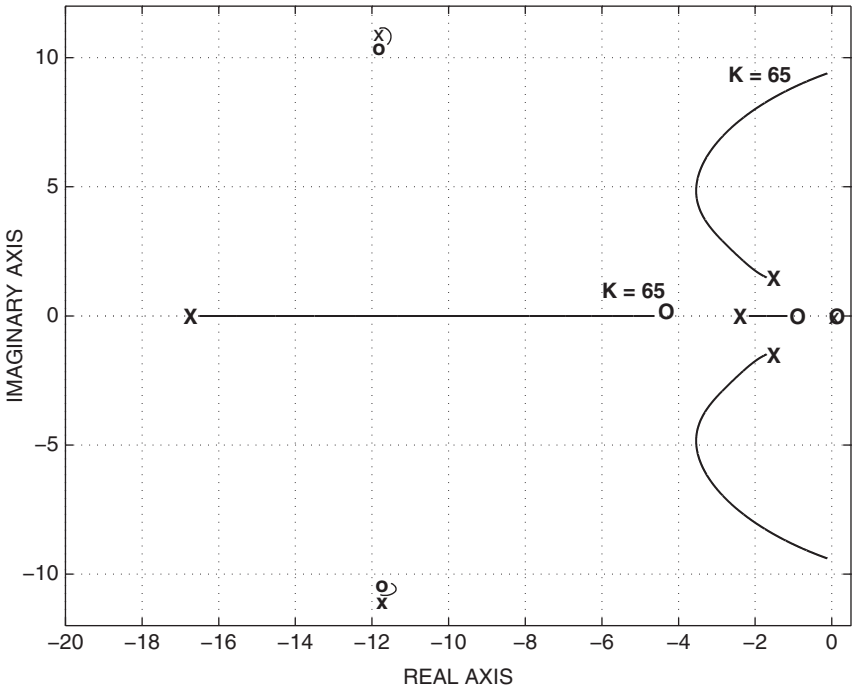

Figure 4.5-8 Root-locus plot for lateral acceleration feedback.

A conservative choice, $k_r = 0.8$, $k_a = 10$, was made for the yaw rate and acceleration feedback gains. The relevant closed-loop transfer functions are

$$\frac{p}{p_C} = \frac{182.7(s + 13.10)(s + 2.428 \pm j2.243)(s + 1.538)(s - 0.002347)}{(s + 13.42)(s + 2.386 \pm j2.231)(s + 1.575)(s + 0.002116)(s + 11.78 \pm j10.96)} \quad (4)$$

$$\frac{a_y}{r_C} = \frac{-0.2539(s - 4.157)(s + 4.00)(s + 11.92 \pm j10.58)(s + 1.00)(s - 0.0001965)}{(s + 13.42)(s + 2.386 \pm j2.231)(s + 1.575)(s + 0.002116)(s + 11.78 \pm j10.96)} \quad (5)$$

A number of poles and zeros can be canceled out of the transfer functions, and there is good decoupling between the two channels. The static loop sensitivity of the first transfer function has changed because the feedback gain k_p has been moved into the forward path, as shown in Figure 4.5-6. Note that the dutch roll mode is satisfactory, and the spiral mode is stable but with an increased time constant. ■

4.6 AUTOPILOTS

Most of the flying qualities specifications do not apply directly to autopilot design. In the case of pilot relief autopilot modes, the autopilot must be designed to meet specifications on steady-state error and disturbance rejection, with less emphasis on dynamic response. In addition, special consideration must be given to the way in which the autopilot is engaged and disengaged, so that uncomfortable or dangerous transient motions are not produced. For example, the altitude-hold autopilot that we will design could not be engaged directly at a few hundred feet below the commanded altitude. Otherwise the result would be a very steep climb, possibly leading to a stall if the engine thrust was not increased.

On the other hand, navigation-coupled autopilot modes must be designed to have a dynamic response that is appropriate to their function. For example, in an automatic terrain-following mode an autopilot must track a randomly changing input of quite wide bandwidth, without significant overshoots in its response. A number of autopilot designs will now be illustrated using the transport aircraft and F-16 dynamic models.

Pitch-Attitude Hold

This autopilot is normally used only when the aircraft is in wings-level flight. The controlled variable is θ ($\theta = \gamma + \alpha$) and the sensor is an attitude reference gyro (which provides an error signal proportional to the deviation from a preset orientation in inertial space). The controller does not hold the flight-path angle, γ, constant because the angle of attack changes with flight conditions. Thus, if thrust is increased, alpha will tend to decrease and the aircraft will climb, and as aircraft weight decreases (as fuel is burned), alpha will decrease, also causing a gradual climb. Similarly, a preset climb will gradually level out as decreasing air density causes alpha to increase. Because of these characteristics the pitch-attitude-hold autopilot is not very important in its own right. However, the same feedback configuration is used in the inner loops of other autopilots, such as altitude hold and automatic landing.

The block diagram of an attitude-hold autopilot is shown in Figure 4.6-1. Dynamic compensation, $G_c(s)$, is necessary if a small steady-state error and good transient

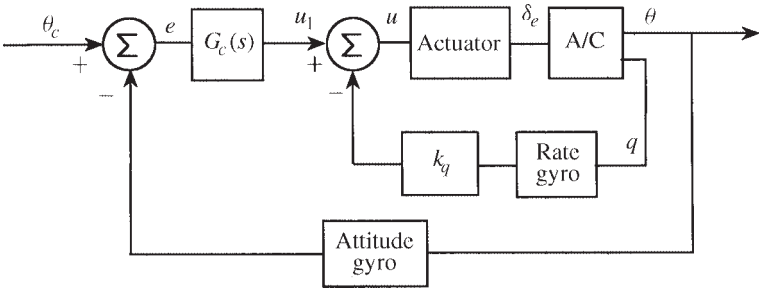

Figure 4.6-1 A pitch-attitude autopilot.

response are required. Inner-loop rate feedback is used to provide additional design freedom and to promote good short-period damping. If the principles are investigated by using only the short-period approximation for the aircraft dynamics, adding an integrator to obtain pitch from pitch rate and a lag model for the elevator actuator, some root-locus sketches will show that the pitch-attitude feedback reduces the damping of the short-period mode and eventually makes it unstable. Pitch attitude is one of the variables involved in the phugoid mode, and an analysis using the complete pitch dynamics will show that the pitch-attitude feedback increases the phugoid damping and eventually produces two stable real poles. An accurate analysis of the effect on the phugoid mode requires that the altitude state also be included in the plant dynamics.

Two design examples will be given, with and without a dynamic compensator, and these designs will be used later as parts of more complex autopilots. The first example will be for a high-altitude cruise condition and the second for a landing condition.

Example 4.6-1: A Simple Pitch-Attitude-Hold Autopilot This example will demonstrate the basic characteristics with no dynamic compensation, so G_c will be simply a gain k_θ. We will also neglect the dynamics of the gyros. The dynamics of the transport aircraft model in a level flight cruise condition at 25,000 ft, 500 ft/s true airspeed, and $x_{cg} = 0.25\overline{c}$ are given by

$$A = \begin{array}{c} \begin{matrix} v_T & \alpha & \theta & q & h \end{matrix} \\ \begin{bmatrix} -0.0082354 & 18.938 & -32.170 & 0.0 & 5.9022E-05 \\ -0.00025617 & -0.56761 & 0.0 & 1.0 & 2.2633E-06 \\ 0.0 & 0.0 & 0.0 & 1.0 & 0.0 \\ 1.3114E-05 & -1.4847 & 0.0 & -0.47599 & -1.4947E-07 \\ 0.0 & -500.00 & 500.00 & 0.0 & 0.0 \end{bmatrix} \end{array} \quad (1)$$

$$B^T = \begin{bmatrix} 0 & 0 & 0 & -0.019781 & 0 \end{bmatrix} \quad \text{(single input } \delta_e\text{)}$$

$$C = \begin{bmatrix} 0 & 0 & 57.296 & 0 & 0 \\ 0 & 0 & 0 & 57.296 & 0 \end{bmatrix} \begin{matrix} \theta \\ q \end{matrix} \qquad D = \begin{bmatrix} 0 \\ 0 \end{bmatrix}$$

These plant matrices will be renamed *ap*, *bp*, and so on and augmented with a simple-lag elevator-actuator model of time constant 0.1 s. The plant sign change

needed to make positive pitch rate correspond to positive elevator deflection will be incorporated in the actuator dynamics. The design procedure will yield values for k_q and k_θ. The MATLAB commands are:

```
plant= ss(ap,bp,cp,dp);
aa= [-10]; ba= [10];              % Actuator
ca= [-1]; da= [0];                % sign change for plant
actua= ss(aa,ba,ca,da);
sys1 = series(actua,plant);
[a,b,c,d]= ssdata(sys1);
```

The transfer function from δ_e to θ is found to be

$$\frac{\theta}{\delta_e} = \frac{-1.133(s+0.5567)(s+0.01897)(s+1.666E-4)}{(s+0.5234\pm j1.217)(s+0.002471\pm j0.08988)(s+1.892E-4)} \tag{2}$$

All of the modes are stable, but the complex modes are quite lightly damped ($\zeta_{sp} = 0.395, \zeta_p = 0.027$) in this flight condition. The altitude pole is almost canceled by a zero, but omitting the altitude state will cause a noticeable error in the phugoid parameters. The effect of pitch-attitude feedback on this transfer function can be deduced from the root-locus rules. The altitude pole will move to the nearby zero, and the phugoid poles will move to the real axis and eventually terminate on the two remaining zeros. When the effect of the actuator pole is accounted for, the short-period poles must move toward the right-half plane (approaching 60° asymptotes). Thus, the short-period mode becomes less well damped as the phugoid damping increases.

The steady-state pitch-attitude error can be minimized by making the compensator gain as large as possible. A simple design procedure is to fix k_θ and then use a root-locus plot to adjust k_q for best short-period damping. If the damping is more than adequate, then k_θ can be increased further. The MATLAB commands are:

```
acl= a - b*[k_θ 0]*c;             % Choose k_θ
k= linspace(0,10,1000);
r= rlocus(acl,b,c(2,:),0,k)       % Root locus for k_q
plot(r)
```

Figure 4.6-2 shows the root-locus plot for k_q when $k_\theta = 4.0$ (elevator degrees per degree of pitch). All of the poles except the short-period poles are on the real axis, and the damping of the short-period poles passes through a maximum as k_q varies. The upper branch of the loci will move upward and to the right as k_θ is increased, thus reducing the maximum damping that can be attained.

The maximum short-period damping in Figure 4.6-2 is more than adequate, and a gain ($k_q = 2.5$) corresponding to lower damping and reduced natural frequency ($\zeta = 0.64, \omega_n = 3.12$) was selected. The gains $k_q = 2.5$ and $k_\theta = 4.0$ and the following MATLAB commands will give the closed-loop transfer function:

```
acl= a - b*[4 2.5]*c;              % Close both loops
[z,p,k]= ss2zp(acl,4*b,c(1,:),0)   % Closed-loop, Unity fb
```

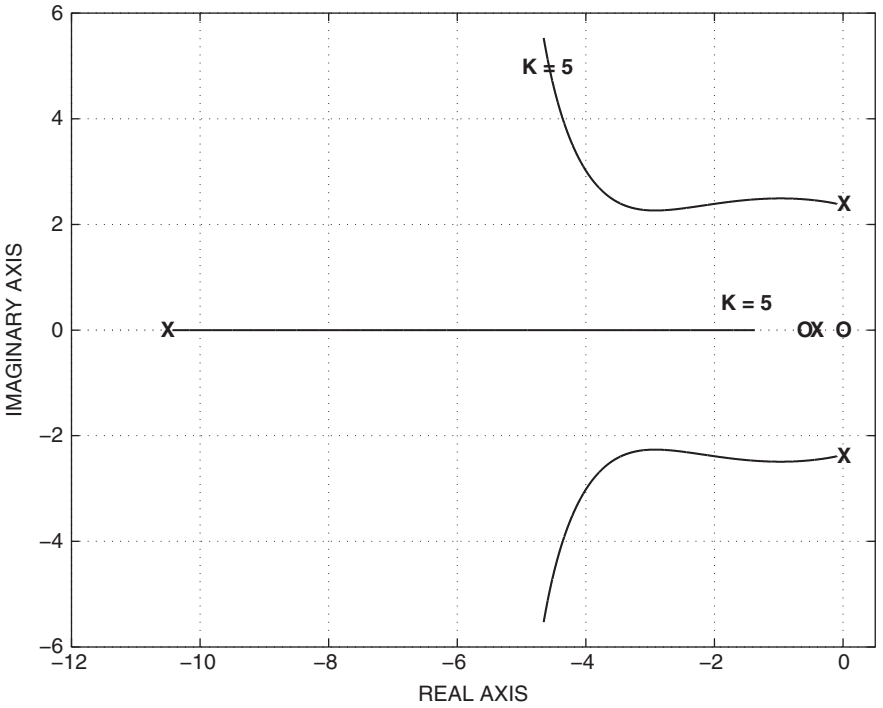

Figure 4.6-2 Root-locus plot for pitch-rate feedback.

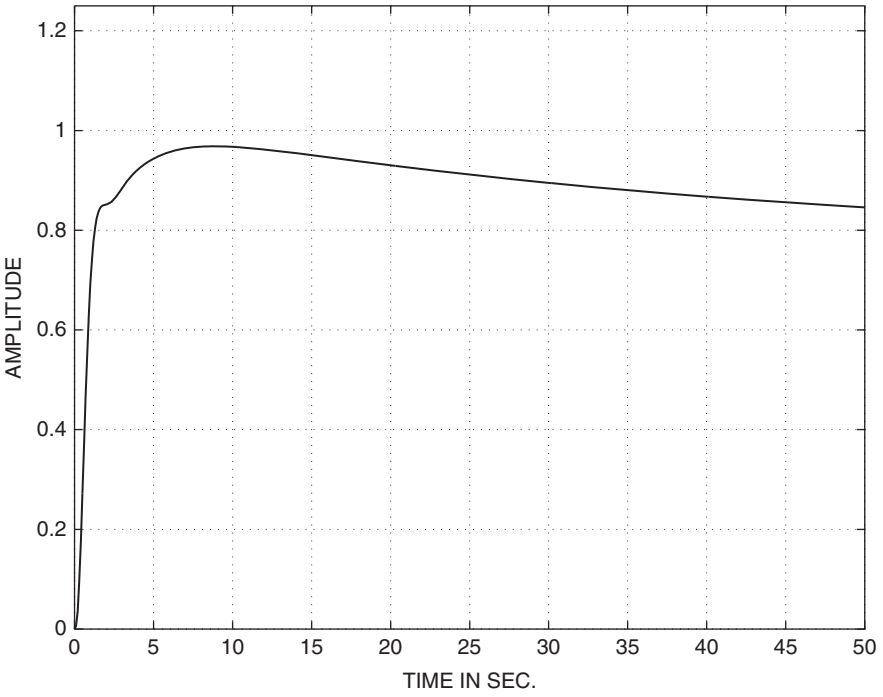

Figure 4.6-3 Step response of the pitch-attitude controller.

The closed-loop transfer function is

$$\frac{\theta}{\theta_c} = \frac{45.33(s+0.5567)(s+0.01897)(s+1.666E-4)}{(s+1.999\pm j2.389)(s+6.646)(s+0.3815)(s+0.02522)(s+1.718E-4)} \tag{3}$$

The altitude pole is almost canceled by a zero, but the cancellation of the degenerate phugoid poles is less exact and they are readily apparent in the step response, shown in Figure 4.6-3. The step response also has a large steady-state error and eventually settles at about 0.77.

This design has the disadvantage that as k_θ is increased to reduce the steady-state error, large values of k_q (i.e., $k_q > 2.5°$ of elevator per degree per second of pitch rate) must be used to obtain adequate damping of the short-period poles. This is likely to cause problems with rate sensor noise or structural-mode feedback. ■

In the next example dynamic compensation will be used to provide fast-responding, more precise control of pitch attitude, so that the controller can be used for the flare and touchdown of an automatic landing system.

Example 4.6-2: A Pitch-Attitude Hold with Dynamic Compensation When the transport aircraft model is trimmed with landing gear and flaps deployed, at $V_T = 250$ ft/s, $h = 50$ ft, $\gamma = -2.5°$, and $x_{cg} = 0.25\bar{c}$, the dynamics are described by

$$A = \begin{array}{c} \begin{matrix} v_T & \alpha & \theta & q \end{matrix} \\ \begin{bmatrix} -3.8916E-02 & 1.8992E+01 & -3.2139E+01 & 0.0000E+00 \\ -1.0285E-03 & -6.4537E-01 & 5.6129E-03 & 1.0000E+00 \\ 0.0000E+00 & 0.0000E+00 & 0.0000E+00 & 1.0000E+00 \\ 8.0847E-05 & -7.7287E-01 & -8.0979E-04 & -5.2900E-01 \end{bmatrix} \end{array} \tag{1}$$

$$B^T = \begin{bmatrix} 0 & 0 & 0 & -0.010992 \end{bmatrix} (\delta_e)$$

$$C = \begin{array}{c} \begin{matrix} & & & \end{matrix} \\ \begin{bmatrix} 0 & 0 & 57.296 & 0 \\ 0 & 0 & 0 & 57.296 \end{bmatrix} \end{array} \begin{matrix} \theta \\ q \end{matrix} \qquad D = \begin{bmatrix} 0 \\ 0 \end{bmatrix}$$

For simplicity the altitude state has been omitted, since its effect on the design is negligible. Once again the plant matrices will be renamed *ap, bp*, and so on, and the same actuator dynamics as Example 4.6-1 will be used:

```
plant= ss(ap,bp,cp,dp);
aa= [-10]; ba= [10];                % Actuator
ca= [-1]; da= [0];                  % sign change for plant
actua= ss(aa,ba,ca,da);
sys1 = series(actua,plant);         % Actuator & Plant
[a,b,c,d]= ssdata(sys1);
acl= a- b*[0 k_q]*c;                % Close Pitch-rate fb
%[z,p,k]= ss2zp(acl,b,c(1,:),0)
qclosed= ss(acl,b,c(1,:),0);        % SISO system for theta
```

The pitch-rate feedback gain, k_q, will be limited to a smaller value than Example 4.6-1 for the reasons mentioned there. A gain $k_q = 1.0$ results in a short-period damping ratio of $\zeta_{sp} = 0.74$; the elevator-input-to-pitch-attitude transfer function is then

$$\frac{\theta}{u_1} = \frac{6.298(s + 0.6112)(s + 0.07305)}{(s + 0.9442 \pm j0.8674)(s + 0.01836 \pm j0.1328)(s + 9.288)} \tag{2}$$

and this value of k_q will be used for the rest of the design. A PI compensator will be used to remove the steady-state pitch error. The PI zero will be placed between the zeros at $s = -0.07$ and $s = -0.6$, so that the PI pole will move toward $s = -0.07$. The phugoid poles will move toward the real axis between the other two zeros and become heavily damped. The following commands can be used to add the PI compensator, determine the gain and phase margins, close the pitch attitude loop, and test the step response:

```
zero= ?                                % Choose a PI zero position
picomp= ss([0],[zero],[1],[1]);        % PI Compensator
syspi = series(picomp,qclosed);        % PI comp & system
[a,b,c,d]= ssdata(syspi);
k1= ?                                  % Choose Proportional Gain
% margin(a,k1*b,c,0);                  % Gain & Phase Margins
acl= a - b*k1*c;                       % Close Pitch Loop
closd= ss(acl,k1*b,c,0);               % Scale b for unity feedback
step(closd,50)                         % Cl.-loop step response
```

Some trial and error with the step response led to a PI zero at $s = -0.2$ and $k_1 \approx 2$. The resulting step response still exhibits an overshoot with a small short-period oscillation superimposed on a well-damped phugoid oscillation, which takes a long time to settle. A large increase in loop gain should reduce the residues in the slow poles but will degrade the short-period damping unless an additional compensator is used.

A root-locus sketch using transfer function (2), with the PI pole and zero added, shows that a phase-lead zero to the left of the short-period poles should pull the poles to the left and allow higher loop gain for a given damping. The phase-lead compensator was given a pole-to-zero ratio of 10 (the maximum recommended), and the pole frequency was adjusted to maximize the gain and phase margins while progressively raising the loop gain. The relevant code is:

```
pole= ?                              % Choose a pole position
lead= ss(-pole,pole,-.9,1);          % Lead compensator
sysall= series(lead,syspi);          % PI + Lead + Plant
[a,b,c,d]= ssdata(sysall);
k1= ?                                % Choose Proportional Gain
margin(a,k1*b,c,0);                  % Gain & Phase Margins
```

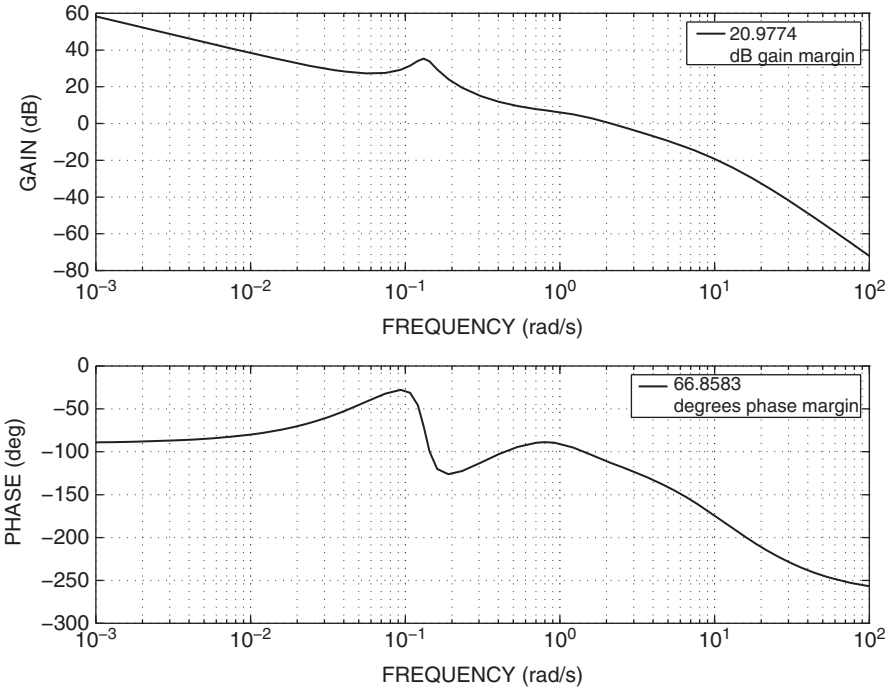

Figure 4.6-4 Bode plots for the pitch-attitude controller.

The compensator

$$G_c = 40\,\frac{s+0.2}{s}\,\frac{s+1.4}{s+14} \tag{3}$$

gives a phase margin of 66.8° at 0.33 Hz and a gain margin of 21 dB at 1.75 Hz. The phase and gain margin plots with this compensator are shown in Figure 4.6-4. The closed-loop pitch attitude transfer function, with unity feedback, is given by

$$\frac{\theta}{\theta_c} = \frac{251.9(s+0.6112)(s+0.07305)(s+1.40)(s+0.20)}{(s+2.121\pm j1.762)(s+0.2717\pm j0.1516)(s+0.06335)(s+4.170)(s+16.19)} \tag{4}$$

In the transfer function (4) the short-period mode has increased in frequency [compared to (2)], and the phugoid mode has increased in frequency and become more damped. The step response, shown in Figure 4.6-5, has a fast rise time but is slow to settle and contains an undesirable undershoot at about 2 s. If the PI compensator closed-loop zero is removed, by the modification shown in Figure 3.9-9, the rise time will be slower but a response that resembles that of a dominant complex pair can be obtained. This is also shown in Figure 4.6-5.

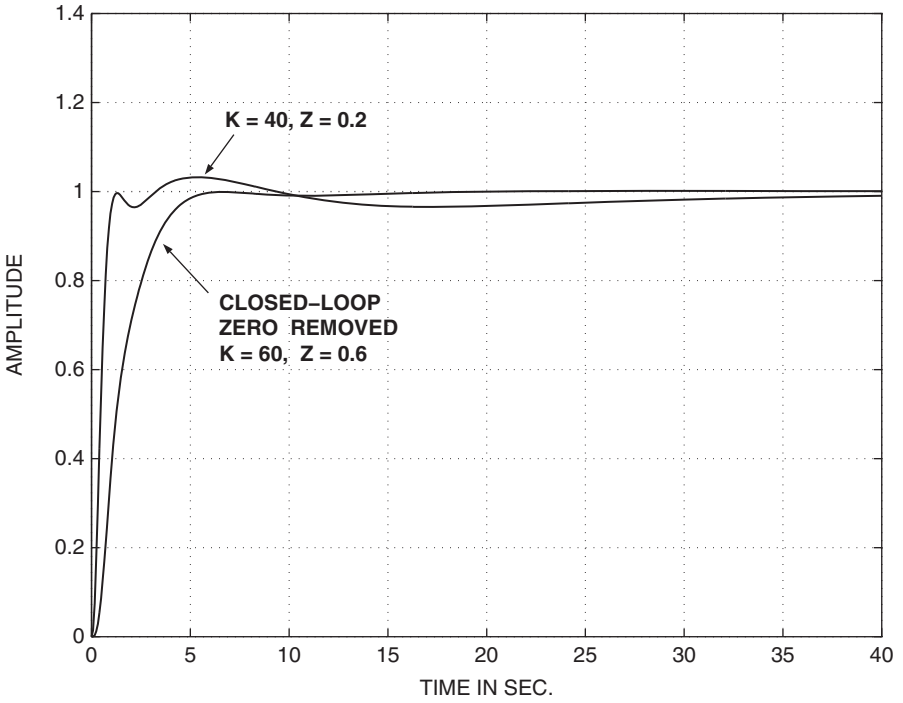

Figure 4.6-5 Step response of the pitch-attitude controller.

■

Altitude Hold/Mach Hold

Altitude hold is an important pilot relief mode; it allows an aircraft to be held at a fixed altitude in an air route corridor to meet air traffic control requirements. The sensed altitude is normally the *pressure altitude*, that is, altitude computed in the air data computer from external pressure measurements. In a modern passenger aircraft the altitude hold will typically hold the aircraft well within ±200 ft and provide a warning signal if the deviation exceeds ±100 ft. The system will have *limited authority* over the horizontal control surfaces and will again warn the pilot if the control limits have been reached. These situations will often occur, for example, in rapidly rising air currents deflected upward by mountain ranges ("mountain waves"). A modern system may also have an "easy-on" or "fly-up, fly-down" feature that allows the autopilot to take the aircraft to an assigned altitude without exceeding certain rate-of-climb and pitch-attitude limits (e.g., 2000 to 3000 ft/min, 20° pitch attitude).

The Mach-hold autopilot is chiefly used on commercial passenger jets during climb and descent. During a climb the throttles may be set at a fairly high power level, and feedback of Mach number to the elevator will be used to achieve a constant-Mach climb. The speed will vary over the range of altitude, but the constant Mach number will provide the best fuel efficiency. Similarly, a descent will be flown at constant Mach with the throttles near idle. At the cruising altitude, control of both the throttle

and elevator will be used to provide altitude hold and speed hold for pilot relief and efficient cruising. In the following example an altitude-hold design will be illustrated.

Example 4.6-3: An Altitude-Hold Autopilot Design The altitude-hold configuration is shown in Figure 4.6-6, where G_c is a compensator and G_F is the effective lag of the pressure-altitude measurement. In the interest of simplicity the altitude sensor lag will be omitted from this example. Again for simplicity, the basic pitch-attitude autopilot from Example 4.6-1 will be used to provide the inner loops of the design, and the compensator G_c will still allow good altitude control to be achieved. The first design goal will be to achieve a high loop gain for good rejection of low-frequency (lf) altitude disturbances and small altitude error. Second, an altitude response that is deadbeat and relatively slow will be required for energy efficiency and passenger comfort.

Altitude is one of the state variables, and by adding an appropriate row to the C-matrix in Example 4.6-1, the transfer function from the pitch-attitude command to altitude can be determined. The altitude feedback has a strong effect on the phugoid poles and a relatively weak effect on the short-period poles. Therefore, the damping of the short-period mode will initially be set close to the desired final value. Thus, based on the experience of Example 4.6-1, the pitch-rate and pitch-attitude feedback loops will be closed by gains $k_q = 2.5$ and $k_p = 3.0$. Starting from "sys1" in Example 4.6-1, we have

```
[a b c d]= ssdata(sys1)              % Actuators & Plant
acl= a- b*[3 2.5]*c;                 % Close k_p and k_q loops
ch= [0 0 0 0 1 0]                    % C matrix for Altitude
[z,p,k]= ss2zp(acl,3*b,ch,0)         % Transfer fn. h/θ_c
```

The transfer function from θ_c to h, with unity feedback of θ, is

$$\frac{h}{\theta_c} = \frac{168.4(s + 0.002264)}{(s + 2.261 \pm j1.936)(s + 6.170)(s + 0.3333)(s + 0.02750)(s + 1.731E - 4)} \tag{1}$$

with a short-period damping ratio of 0.76.

A root-locus sketch shows that the poles from $s = -0.028$ and $s = -0.333$ will break away from the real axis to form phugoid poles. The phugoid poles will move toward the right-half plane, while the short-period poles and the pole from $s = -6.17$

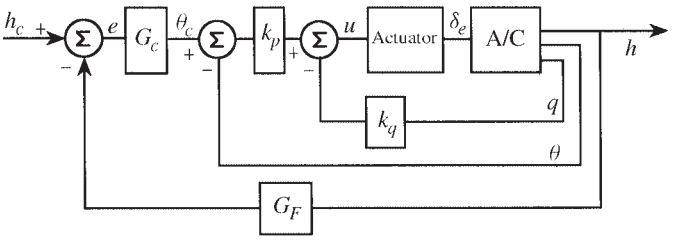

Figure 4.6-6 An altitude-hold autopilot.

move left. A phase-lead compensator with its zero close to $s = -0.333$ will improve the gain and phase margins. A compensator pole-to-zero ratio of 8 was chosen (a compromise between noise accentuation and too little phase lead), and the pole frequency was adjusted for the best margins each time the gain was raised. A deadbeat step response was found to require a large phase margin ($\approx 70°$). The commands were:

```
sys2= ss(acl,3*b,ch,0);
pole= ?                                  % Choose Lead-Comp. Pole
lead= ss(-pole,pole,-.875,1);            % Lead-compensator
sys3= series(lead,sys2);                 % Cascade with c.l. system
[a,b,c,d]= ssdata(sys3);
k= ?                                     % Choose loop gain
margin(a,k*b,c,0)                        % Check Margins
```

and the lead compensator

$$G_c = \frac{s + 0.3}{3(s + 2.4)} \tag{2}$$

gives gain and phase margins of 13.3 dB and 71.2°, respectively. Unfortunately, the lead compensator reduces the lf loop gain. The transfer function (1) has an lf gain of about 72.8 dB (or 4380) and the compensator (2) reduces this by 27.6 dB (i.e., 1/24). The final loop gain of 45.2 dB (or 182) would allow a steady-state altitude error of 1 ft per 183 ft, a rather poor performance. The performance can be improved by adding a lag compensator that boosts the lf gain, while adding negligible phase lag in the frequency range of the lead compensator. The same effect can be achieved by using a PI compensator to make the altitude control loop type 1 and placing the PI zero close to the origin. A simple lag compensator has the advantage that it can be implemented with passive components (see Table 3.3-1), provided that the time constant is not too large. Modern electronics has diminished this advantage but, for an analog design, a lag compensator is still simpler and more reliable than a PI compensator, and its use will be illustrated here.

Practical considerations limit the maximum time constant of an analog lag compensator to about 100 s (pole at $s = -0.01$). If the compensator zero is chosen to give a large lf gain increase, then it will be found that in the closed-loop transfer function the slow poles (from $s = -0.0275$ and $s = -0.01$) have relatively large residues (i.e., do not cancel with zeros). If the lag compensator zero is placed near $s = -0.05$ (i.e., an lf gain increase of 5) these slow poles will have a relatively small effect on the closed-loop time response. There will also be less phase lag in the frequency range where the lead compensator is to be added. Therefore, the lag compensator zero was placed at $s = -0.05$. The commands were:

```
lag= ss(-.01,.01,4,1);
sys4= series(lag,sys3);
[a,b,c,d]= ssdata(sys4);
margin(a,.3333*b,c,0);
acl= a-.3333*b*c;
closed= ss(acl,.3333*b,c,0);
step(closed,30)
```

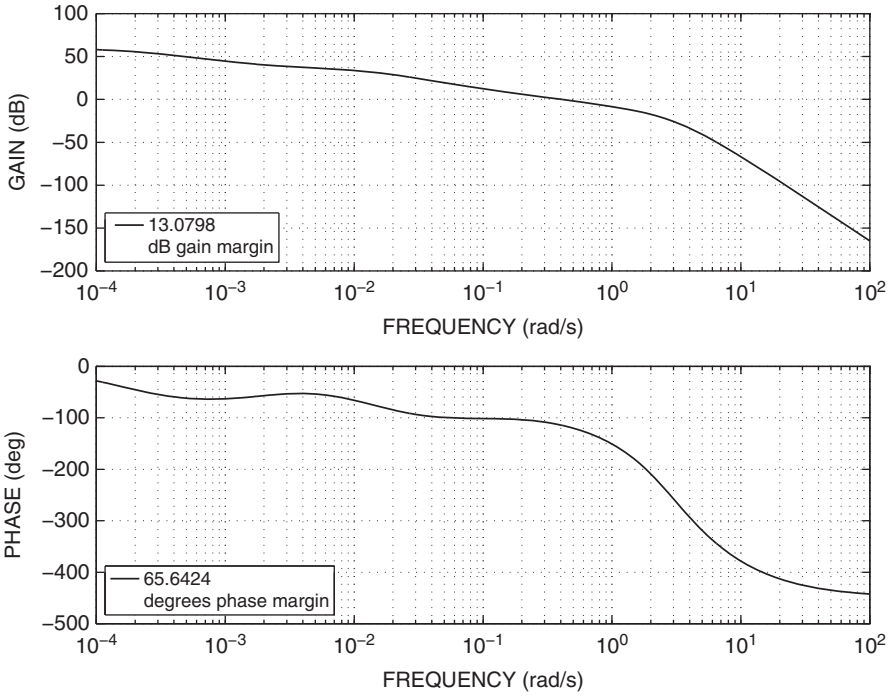

Figure 4.6-7 Bode plots for the altitude-hold controller.

The gain and phase margins with both compensators are 13.1 dB and 65.7°, respectively. The lf loop gain is 913, which is adequate. Figure 4.6-7 shows the phase and gain margin Bode plots.

The closed-loop altitude transfer function is

$$\frac{h}{h_c} = \frac{56.14(s+0.30)(s+0.050)(s+0.002264)}{(s+6.29)(s+2.75 \pm j2.03)(s+0.673 \pm j0.604)(s+0.267)(s+0.053)(s+0.00224)} \tag{3}$$

A comparison with transfer function (1) shows that the fast poles have not moved significantly, the three slowest poles essentially cancel out of the transfer function, and a new complex pair has been created.

The step response is shown in Figure 4.6-8. The effect of the slow poles is visible as a small, slowly decaying displacement from the final value. The steady-state error will be negligible because of the high value of the lf loop gain. The response is essentially deadbeat and is considerably slower than a pitch-axis response. It could be slowed down further by reduction of the loop gain or by using additional lag compensation but is considered to be satisfactory. As pointed out earlier, it is obvious that this autopilot would not normally be directly engaged with a large altitude error.

The reader may wish to consider repeating this design for cruising conditions at, say, 35,000 ft, to determine the need for scheduling of the controller gains.

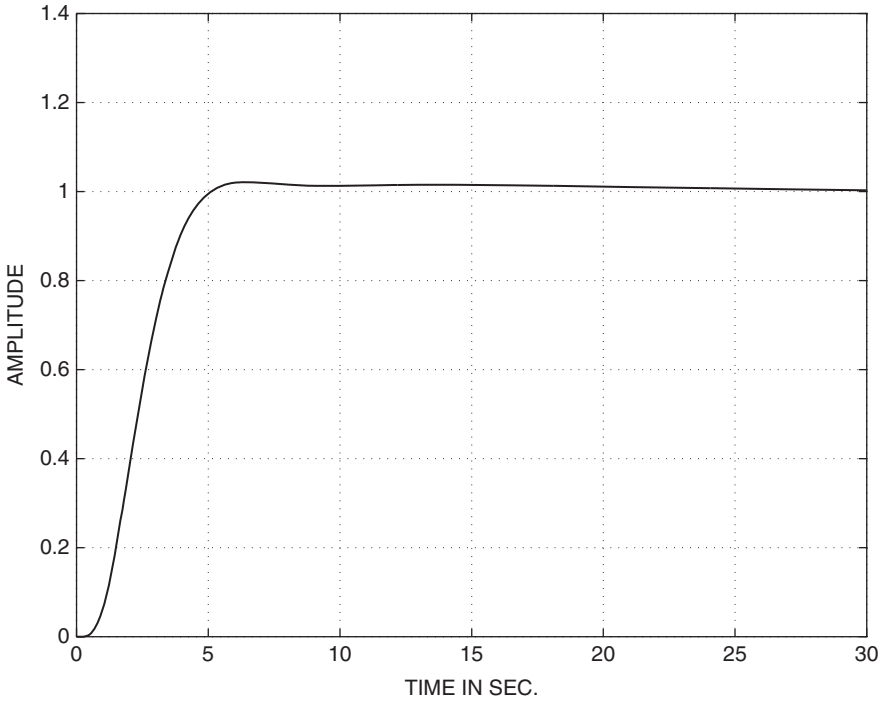

Figure 4.6-8 Step-response of the altitude-hold controller.

■

Automatic Landing Systems

In Section 4.1 we referred to the need for automatic control in situations where controlling the trajectory of an air vehicle was too difficult a task for a human pilot. A particular case of this is the landing phase in conditions such as bad weather or limited visibility. Landing in limited visibility may be achieved by providing the pilot with instruments to determine the aircraft's position relative to a reference trajectory, but a landing in more difficult conditions requires full automatic control with the pilot playing only a supervisory role.

Automatic control of the longitudinal trajectory requires simultaneous control of engine thrust and pitch attitude because, for example, using only the elevator to attempt to gain altitude may result in a loss of speed and an eventual stall. If the landing speed is such that the aircraft is on the "back side" of the power curve (see Chapter 3 Section Steady-State Flight), the throttle controls altitude and the elevator controls airspeed (increased power causes a gain in altitude, down elevator causes a gain in speed).

An aircraft is normally *reconfigured* for landing and takeoff by deploying wing leading- and trailing-edge devices (slats, flaps) so that the wing effectively has more camber and area. This provides more lift at low speed and increased drag; the wing is thereby optimized for a low-speed landing. The reconfiguration has the effect of

moving the minimum of the power curve to lower speed. Thus, most aircraft do not operate on the back side of the power curve, although naval aviators are routinely taught to fly in this regime for aircraft carrier operations. The reconfigured wing and extended landing gear produce a strong nose-down moment, which in turn leads to a trim with a large amount of "up" elevator. We will see this effect in our transport aircraft model in the following example, and these conditions play a role in determining the elevator size and deflection limit during the aircraft design.

A typical automatic landing system uses a radio beam directed upward from the ground at 3°, with equipment onboard the aircraft to measure the angular deviation from the beam and compute the perpendicular displacement of the aircraft from the *glide path*. Additional equipment is used to provide azimuth information, so that the aircraft can be lined up with the runway. The glide path must usually be intercepted at, at least, 3000 ft altitude (over the outer marker), and the aircraft will descend with an airspeed of 130 to 150 knots (220 to 253 ft/s) under automatic control.

Figure 4.6-9 shows an elevation view of a descending trajectory with velocity V_A (in tangent-plane coordinates) and flight-path angle γ. The reference trajectory has an angle γ_R, and the radio beam equipment is at the position Q. Assume that the aircraft passes through the radio beam at point P and time t_1 and the descent is too gradual (as shown). The resulting positive glide-path deviation that builds up is denoted by d. The automatic landing equipment measures the angular deviation δ and the range R and calculates d from

$$d = R \sin \delta \tag{4.6-1}$$

An onboard automatic control system is used to maneuver the aircraft so that d is driven back to zero.

To design a control system we must relate d to the aircraft trajectory. The geometry of the figure shows that the derivative of d is given by

$$\dot{d} = V_A \sin(\gamma - \gamma_R) \tag{4.6-2}$$

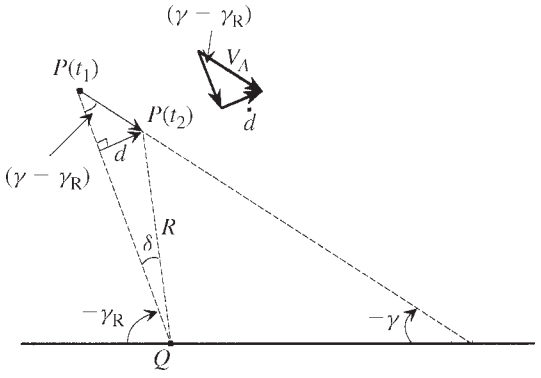

Figure 4.6-9 Glide-slope geometry for autoland.

Therefore, $d(t)$ can be derived by integrating this equation with the aircraft state equations, with the initial condition $d(t_1) = 0$ applied at the time t_1 at which the aircraft intersects the glide path. Note that when d is computed from (4.6-1), the sensitivity of d to flight-path changes will depend on the range R. This effect will be assumed to be compensated for in the onboard computer, so that an automatic control system can be designed for some nominal value of the range. The design of the longitudinal control system for automatic landing will now be presented as an example.

Example 4.6-4: Longitudinal Control for Automatic Landing. Figure 4.6-10 is a block diagram of the autoland control system. The transport aircraft model in the landing configuration will be used. The throttle servo and engine response will be modeled by a single 5-s lag and the elevator servo by a 0.1-s lag, as shown; sensor lags have been neglected. The compensators that must be designed are G_1 and G_2, and the pitch-attitude controller will be taken from Example 4.6-2.

Equation (4.6-2) was added to the transport aircraft model, with γ_R as a model input and d as an additional state. The model was trimmed with gear down and landing flap settings for the conditions $V_T = 250$ ft/s, $\gamma = -2.5°$, $x_{cg} = 0.25\,\bar{c}$, and $h = 750$ ft. The A and B Jacobian matrices for this flight condition are

$$ap = \begin{array}{c} \begin{matrix} v_T & \alpha & \theta & q & h & d \end{matrix} \\ \begin{bmatrix} -0.038580 & 18.984 & -32.139 & 0 & 1.3233E-4 & 0 \\ -0.0010280 & -0.63253 & 0.0056129 & 1.0 & 3.7553E-6 & 0 \\ 0 & 0 & 0 & 1.0 & 0 & 0 \\ 7.8601E-5 & -0.75905 & -0.00079341 & -0.51830 & -3.0808E-7 & 0 \\ -0.043620 & -249.76 & 249.76 & 0 & 0 & 0 \\ 0 & -250.00 & 250.00 & 0 & 0 & 0 \end{bmatrix} \end{array};$$

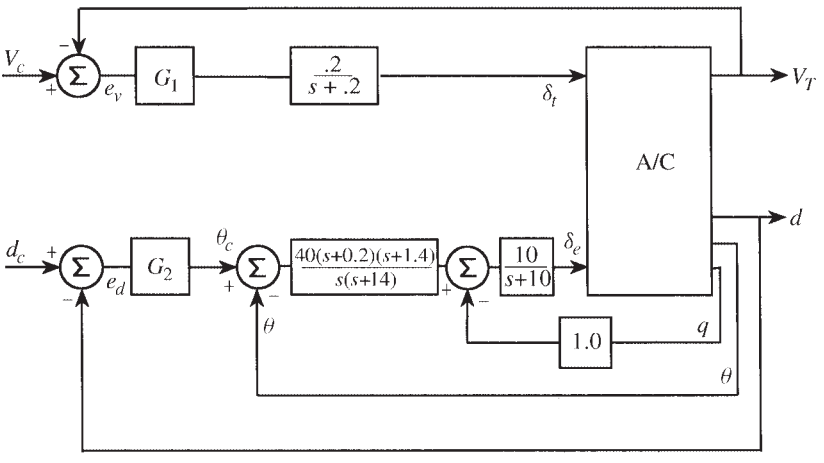

Figure 4.6-10 Control system for automatic landing.

$$bp = \begin{array}{c} \begin{matrix} \delta_t & \delta_e \end{matrix} \\ \begin{bmatrix} 10.100 & 0 \\ -1.5446E-4 & 0 \\ 0 & 0 \\ 0.024656 & -0.010770 \\ 0 & 0 \\ 0 & 0 \end{bmatrix} \end{array}$$

The classical design procedure will be, as usual, to close one loop at a time. In this example there are four loops to be closed. Each loop closure changes both the poles and zeros for the other loop transfer functions. Preferably, the loops should be closed in a sequence that minimizes the number of design iterations. The pitch-attitude control loops are inner loops that we might logically expect to close first. If the effects of thrust and speed on pitching moment are not strong, then the pitch-attitude loops will be affected only by the change in angle of attack with speed. When the pitch-attitude loop is closed, changes in speed will cause changes in the angle of attack and therefore in the flight-path angle and $\dot{d}$. The pitch-attitude control thus determines the interaction of the speed loop on the d-loop. We will close the pitch-attitude loops first using the controller from Example 4.6-2. The d control loop cannot hold the required trajectory without closing the speed (auto-throttle) loop, but the speed loop can function independently of the d-loop. Therefore, the speed loop should logically be closed next.

Following Example 4.6-2, the pitch-attitude controller can be applied with the following commands:

```
cp= [ 0 0 57.29578 0 0 0; 0 0 0 57.29578 0 0];   % theta & q
dp= [0, 0];
plant= ss(ap,bp(:,2),cp,dp);                    % Elev. input
actua= ss(-10,10,-1,0)                          % Change sign at output
sys1 = series(actua,plant);                     % 1 i/p, 2 o/p
[a,b,c,d]= ssdata(sys1);
acl= a- b*[0 1]*c;                              % Close q-loop, k_q=1
qclosed= ss(acl,b,c(1,:),0);                    % SISO
lead= ss(-14,14,-.9,1);                         % Lead compensator
sys2= series(lead,qclosed);
picomp = ss(0,0.2,1,1);                         % PI compensator
sys3= series(picomp,sys2);
[a,bt,c,d]= ssdata(sys3);
acl= a- bt*40*c(1,:);                           % Close theta loop
```

The closed-loop zero of the PI compensator has been retained because additional zeros provide more phase lead when compensating the outer loops. The transfer function from throttle to speed can now be found:

```
cvt= [1 0 0 0 0 0 0 0 0];              % C-matrix for VT
bth= [bp(:,1);0;0;0];                  % B-matrix for Throttle i/p
[z,p,k]= ss2zp(acl,bth,cvt,0);         % Get poles and zeros
```

After canceling some very close pole-zero pairs, the throttle-to-speed transfer function is

$$\frac{v_t}{\delta_t} \approx \frac{10.10(s + 0.2736 \pm j0.1116)(s + 0.001484)}{(s + 0.2674 \pm j0.1552)(s + 0.0002005)(s + 0.06449)} \tag{1}$$

A root-locus sketch of transfer function (1) (not shown) shows that the pole from $s = -0.06$ will move left to meet the pole from the throttle servo (when added), and they will break away from the real axis to approach 90° asymptotes. Given the slow response of the throttle servo and engine lag, we may try to speed up the auto-throttle loop with a phase-lead compensator, although this may cause the throttle servo to saturate frequently. Adding the throttle servo and closing the loop with no additional gain show an infinite gain margin and a phase margin of about 10°. The low-frequency loop gain is about 60 dB and the resulting small steady-state error will be acceptable. Therefore, a lead compensator was chosen to improve the phase margin of this loop.

The compensator

$$G_1(s) = \frac{10(s + 1)}{s + 10} \tag{2}$$

gives a phase margin of about 60° and retains the same lf loop gain. The speed control loop can now be closed:

```
th2vt = ss(acl,bth,cvt,0);              % SISO, throttle to speed
servo = ss(-.2,.2,1,0);                 % Throttle servo & Eng. lag
ut2vt = series(servo,th2vt);
splead= ss(-10,10,-.9,1);               % Phase lead
compsp= series(splead,ut2vt);           % Compensator & plant
[a,b,c,d]= ssdata(compsp);
acl= a- b*10*c;                         % Close auto-throttle loop
```

With the speed loop closed, the d/θ_c transfer function for the final loop closure is found from:

```
btheta= [40*bt; 0; 0];       % B-matrix for unity f.b. theta-loop
cd = [0 0 0 0 0 1 0 0 0 0 0];     % C-matrix for d output
[z,p,k]= ss2zp(acl,btheta,cd,0)   % d/θc transfer fn.
```

After removing some canceling pole-zero pairs, the transfer function reduces to

$$\frac{d}{\theta_c} = \frac{675.2(s + 1.40)(s + 0.20)}{(s + 2.021 \pm j1.770)(s + 0.2725 \pm j0.1114)(s + 4.409)(s + 16.16)(s + 0.001475)} \tag{3}$$

Notice that the zeros were created by the compensators in the pitch-attitude controller. A sketch of the root-locus plot will show that the poles at $s \approx (-0.27 \pm j0.11)$ move into the right-half plane as the loop gain is increased, and the margin command shows that with unity feedback the gain and phase margins would be negative. In addition, a Bode plot shows that the lf gain levels out at 69 dB (2818). Using the margin command to optimize a phase-lead compensator, we find that $2(s + 0.6)/(s + 6)$

will provide a phase margin of 58.4° and a gain margin of 11.1 dB, but the lf gain is then reduced to 2818/5, or 563. It is desirable to follow the glide slope closely when near the ground; therefore, we will make the controller type 1 by adding a PI compensator, as well as the phase lead.

When a PI controller and lead compensator are cascaded with transfer function (3), a root-locus sketch shows that the integrator pole and the pole from $s = -0.0015$ will circle to the left in the s-plane to terminate eventually on the PI zero and the zero at $s = -0.20$. By placing the PI zero near the zero at $s = -0.2$ and, using high gain, we will hope to get small residues in these slow poles and avoid a very sluggish closed-loop response. Note that the zero at $s = -0.20$ from the pitch-attitude controller is now partly responsible for determining the speed of response of the d loop.

The compensator

$$G_2(s) = 1.0 \times \frac{(s + 0.18)(s + 0.5)}{s(s + 5)} \tag{4}$$

was derived by examining the effect of the PI zero on the closed-loop poles and zeros and the step response. The lead compensator was adjusted to obtain a compromise between the gain and phase margins, and these were, respectively, 14.7 dB and 51.6°. Figures 4.6-11*a* and *b* show the Bode plots; note that the pole at $s = -0.0015$

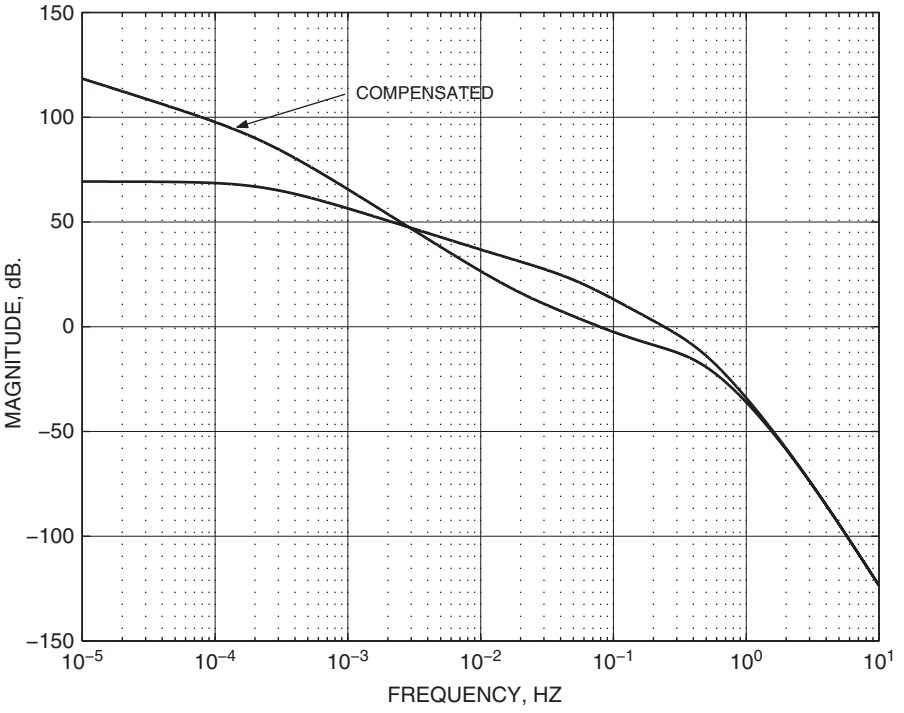

Figure 4.6-11*a* Bode gain plot for the automatic-landing *d*-loop.

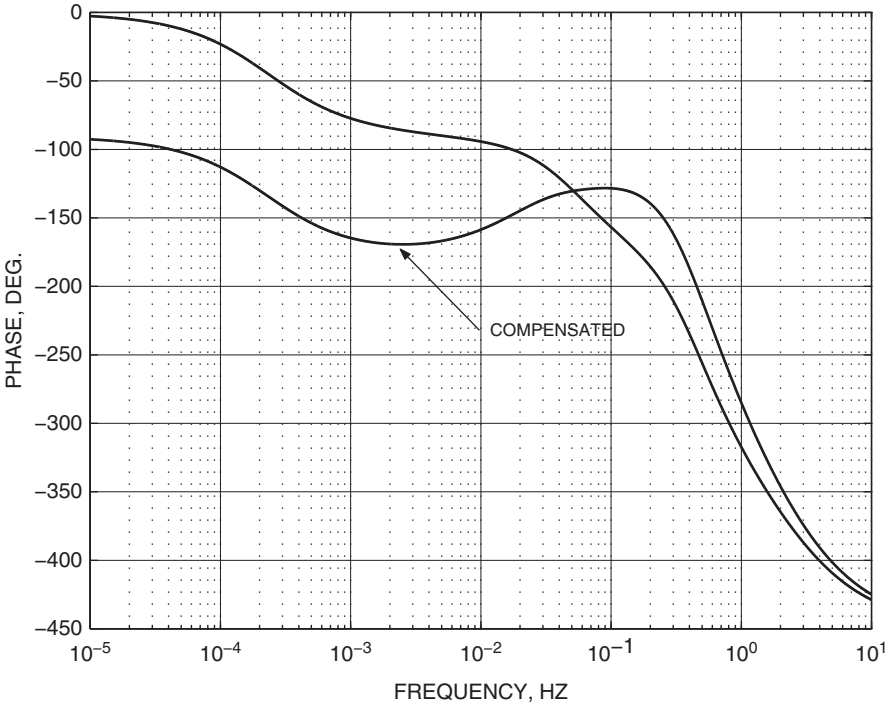

Figure 4.6-11*b* Bode phase plot for the automatic-landing *d*-loop.

causes the low-frequency phase lag to approach $-180°$ (like a type-2 system) before the lead compensation begins to take effect.

When some close poles and zeros are canceled, the principal closed-loop transfer functions are

$$\frac{v_T}{v_c} \approx \frac{20.20(s+1)}{(s+7.627)(s+1.280 \pm j0.9480)} \tag{5}$$

$$\frac{d}{d_c} \approx \frac{677.0(s+1.40)(s+0.50)(s+0.20)(s+0.180)}{(s+16.2)(s+5.16 \pm j1.65)(s+1.38 \pm j1.69)(s+0.292 \pm j0.348)(s+0.179 \pm j0.0764)} \tag{6}$$

Note that in the *d* transfer function the slowest pair of complex poles is close to terminating on the zeros at $s = -0.18$ and $s = -0.20$. The step responses could be evaluated by a linear simulation using the closed-loop state equations. Instead a nonlinear simulation of the glide-path descent will be illustrated in Section 4.7. ■

Roll-Angle-Hold Autopilots

In its simplest form, as a wing leveler, the roll angle autopilot has a history going back to the experiments of Elmer Sperry (see Section Introduction). A sensor incorporating

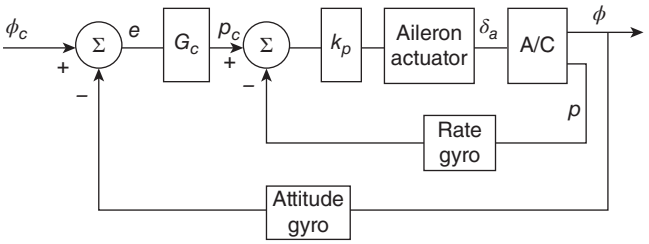

Figure 4.6-12 A roll angle control system.

an attitude reference, such as a gyroscope, is used to sense deviations from the vertical. Feedback of the deviation signal in the aircraft y-z plane to the ailerons can then be used to control the roll angle of the aircraft. The autopilot will hold the wings level and thus provide a pilot relief function for long flights and eliminate the danger of the pilot being caught unaware in a coordinated spiral motion toward the ground.

If the aircraft is held at some attitude other than wings level, additional control systems must be used to control sideslip and pitch rate, so that a coordinated turning motion is produced. Depending on the commanded pitch rate, the aircraft may gain or lose altitude in a turn. If a means of varying the roll reference is provided, the aircraft can be steered in any direction by a single control. These control systems can provide the inner loops for other autopilots that allow an aircraft to fly on a fixed compass heading or follow a radio navigational beam in the presence of cross-winds. Such systems will be described later.

Figure 4.6-12 shows a block diagram of a roll-angle-hold autopilot. High-performance aircraft virtually always have available a roll-rate gyro for use by a SAS or CAS, and this can be used to provide inner-loop rate damping for the autopilot. If the roll-rate gyro is not available, then for good performance, a compensator is needed in the roll angle error path. There is usually no requirement for precise tracking of roll angle commands, so type-0 roll angle control can be used. By the same token, the *velocity error* due to straight roll-rate feedback (i.e., no washout) is not important, particularly since the roll rate is not usually sustained for very long.

If the aircraft has strong roll-yaw coupling, the roll-angle-to-aileron feedback must be considered as part of a multivariable design, as in Sections 4.4 and 4.5. This is often not the case, and in the lateral transfer function, the poles associated with the directional controls are approximately canceled by zeros. The transfer function for the roll angle loop is then determined by the roll subsidence pole, the spiral pole, and the actuator and compensator (if any) poles. If roll-rate feedback is used, in conjunction with the roll angle feedback, there is good control over the position of the closed-loop poles and quite large amounts of feedback can be used. A roll angle autopilot design will now be illustrated.

Example 4.6-5: A Roll Angle-Hold Autopilot This example will use the controller subroutine from the lateral-directional CAS in Example 4.5-3 and with the same flight conditions. In Figure 4.6-12 the dynamics of the gyros will be neglected. With

$k_p = 0.2$, the closed-loop transfer function from the roll-rate command, p_c, to the roll angle in Figure 4.6-12 is found to be

$$\frac{\phi}{p_C} = \frac{182.7(s + 13.09)(s + 2.429 \pm j2.241)(s + 1.540)}{(s + 13.42)(s + 2.386 \pm j2.231)(s + 1.575)(s + 0.002116)(s + 11.78 \pm j10.96)} \quad (1)$$

or, approximately,

$$\frac{\phi}{P_c} = \frac{182.7}{(s + 11.78 \pm j10.96)(s + 0.002116)} \quad (2)$$

In this transfer function the complex pole pair arose from the actuator pole and the roll subsidence pole, and the real pole is the spiral pole. The spiral pole is close to the origin and approximates an integration between the roll rate and the roll angle. When the roll angle feedback loop is closed, the spiral pole moves to the left and the complex poles move to the right. The root-locus plot is shown in Figure 4.6-13.

A proportional gain (for G_c) of $k_\phi = 5.0$ gave the complex poles a damping ratio of $\zeta = 0.71$ (at $s = -8.88 \pm j8.93$), and the real pole was at $s = -5.4$. The roll angle control loop is well damped but unrealistically fast. The commanded attitude will be more tightly controlled in the steady state, but the aileron actuators may be driven

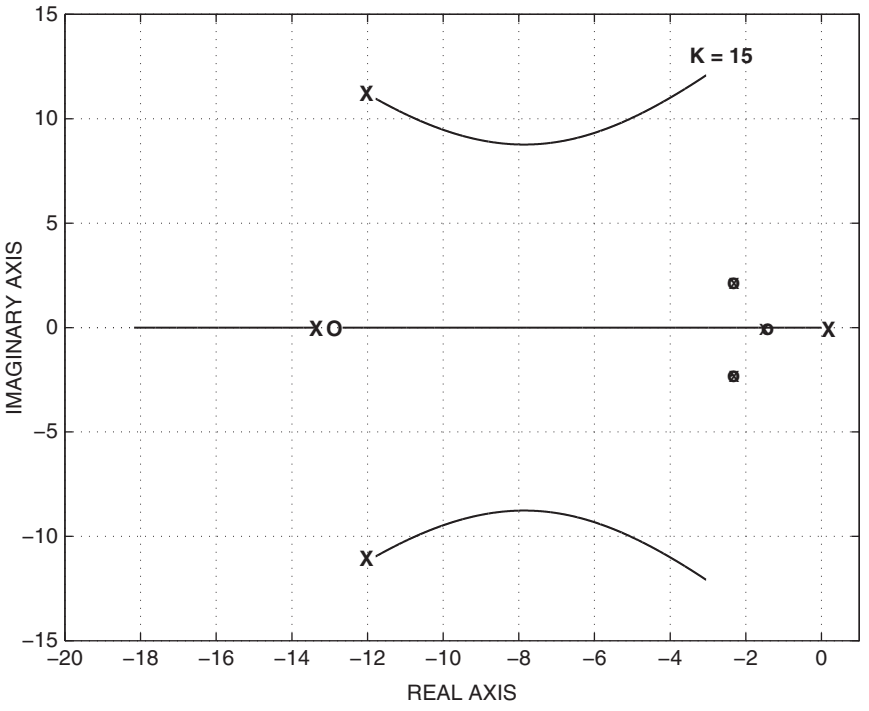

Figure 4.6-13 Root-locus plot for roll-angle-hold controller.

into rate limiting if abrupt roll angle commands are applied. This control system will be used in the next subsection in a nonlinear simulation. ■

Turn Coordination and Turn Compensation

A coordinated turn is defined as zero lateral acceleration of the aircraft cg (i.e., zero component of inertial acceleration on the body y-axis). In a symmetrical aircraft the components of acceleration in the plane of symmetry need not be zero, and so the coordinated turn need not be a steady-state condition. In an asymmetrical aircraft the sideslip angle may not be exactly zero in a coordinated turn because of, for example, asymmetric thrust or the effects of the angular momentum of spinning rotors. Turn coordination is desirable for passenger comfort and, in a fighter aircraft, it allows the pilot to function more effectively. In addition, by minimizing sideslip, it maintains maximum aerodynamic efficiency and also minimizes undesirable aerodynamic loading of the structure. Automatic turn coordination is also useful for a remotely piloted vehicle performing video surveillance or targeting.

In a coordinated turn, level or otherwise, the aircraft maintains the same pitch and roll attitude with respect to the reference coordinate system, but its heading changes continuously at a constant rate. Therefore, the Euler angle rates $\dot{\phi}$ and $\dot{\theta}$ are identically zero, and $\dot{\psi}$ is the turn rate. The Euler kinematical equations (1.3-21) show that, under these conditions, the body-axes components of the angular velocity are

$$\begin{aligned} P &= -\dot{\psi}\sin\theta \\ Q &= \dot{\psi}\sin\phi\cos\theta \\ R &= \dot{\psi}\cos\phi\cos\theta \end{aligned} \tag{4.6-3}$$

If the aircraft is equipped with angular rate control systems on each axis these rates can be computed, and then they can be used as the controller commands to produce a coordinated turn. In level flight, with small sideslip, the turn coordination constraint is given by Equation (3.6-7):

$$\tan\phi = \frac{\dot{\psi}}{g_D}\frac{V_T}{\cos\theta} \tag{4.6-4}$$

If $\cos\theta \approx 1.0$, then, for a specified turn rate $\dot{\psi}$, the required pitch and yaw rates can be calculated and the roll rate can be neglected. This produces a quite satisfactory level turn.

Alternative coordination schemes include feedback of sideslip or lateral acceleration to the rudder or computing just a yaw-rate command as a function of measured roll angle [see Blakelock (1965) for details]. If, in addition, a pitch-rate command is calculated from the above equations as a function of roll angle, the turn can be held level. This is referred to as "turn compensation" (Blakelock, 1965); it can also be achieved by using altitude feedback to the elevator. An example of turn coordination is given in Example 4.7-5.

Autopilot Navigational Modes

Automatic navigation is an important autopilot function for both military and civil aircraft, and the most important systems will be briefly summarized. A *heading-hold* autopilot is designed to hold the aircraft on a given compass heading. The conventional method of implementing this autopilot is to close an additional yaw angle feedback loop around the roll angle control system (including turn compensation) that was illustrated above. Figure 4.6-14 shows the arrangement. The transfer function relating heading angle to roll angle uses the linearized equation obtained from (4.6-4) when ϕ is small and $\cos\theta \approx 1$. Note that the transfer function gain is inversely proportional to speed. An investigation of the root locus for the heading angle loop and the effects of flight conditions will be left to the reader [see also Blakelock (1965) and Roskam (1979)].

A *VOR-hold* (VHF Omni Range) autopilot is an autopilot designed to home on an omnidirectional radio beacon. The heading-angle-hold system (including, e.g., turn compensation) is used to implement this autopilot, and Figure 4.6-15 shows how this is done. The transfer function derived from the geometry of the beam following is similar to that derived for the automatic-landing longitudinal control system. The system normally requires proportional-plus-integral compensation and possibly lead compensation also. Again, it is left to the reader to investigate further (Blakelock, 1965; Roskam, 1979).

A specialized military autopilot that is particularly interesting is a *terrain-following, terrain avoidance* (TFTA) autopilot. This system uses the aircraft's radar

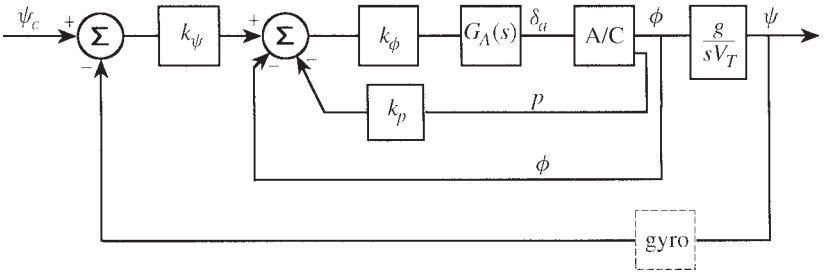

Figure 4.6-14 A heading-hold control system.

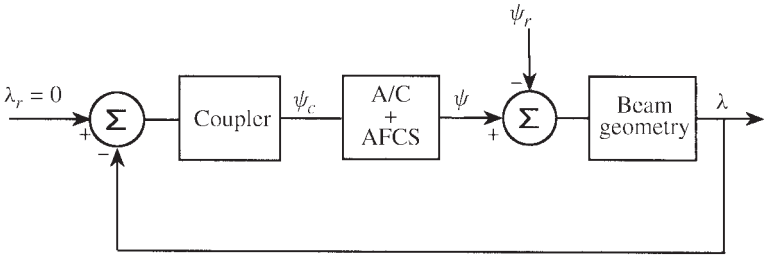

Figure 4.6-15 A VOR-hold autopilot.

or a separate radar carried underneath the aircraft (as in the LANTIRN system). The radar provides guidance commands to fly at constant height (e.g., 100 to 400 ft) above Earth's surface at high speed. The fly-up, fly-down commands are usually applied to a g-command control system as described in Section 4.5, and the lateral-directional guidance commands are applied to a roll angle steering control system as in Example 4.7-5.

4.7 NONLINEAR SIMULATION

The linear designs illustrated in previous sections are only the first stage in the design of complete aircraft control systems. At the second stage the control systems must be evaluated on a nonlinear model of the aircraft, with larger amplitude maneuvers and over a larger portion of the envelope. To perform this evaluation, nonlinear control system elements must be modeled (e.g., any multipliers or nonlinear calculations in the control system equations and rate limiting and deflection limiting in the control surface actuators). Actuator performance will be strongly affected by the aerodynamic loads on the control surface, further complicating the nonlinear behavior. During this second stage the nonlinear simulation can be done with preprogrammed commands or with a desktop flight simulator with no cockpit, rudimentary controls, and limited video display capabilities. At a later stage the nonlinear simulation will be performed with a cockpit mock-up and out-of-the-window video displays and used for piloted evaluation of the aircraft. This will eventually be followed by pilot training in the simulator.

In nonlinear simulation it is highly desirable to separate the control system equations from the equations of motion and from the aerodynamic database. If this is done, errors are easier to find, different controller designs can be substituted easily, there is less chance of corrupting unrelated computer code, and not all of the code has to be recompiled when changes are made. In a big organization different groups of people are responsible for the aerodynamic database and the control systems, and this partitioning of the computer software is very appropriate. The state-space formulation greatly facilitates the achievement of this objective. State variables that are needed for the controllers can be numbered independently of state variables needed for the equations of motion or any other equation set, and at compilation time or during code interpretation, all of the state variables can be placed in one large array for numerical solution purposes. This is like a parallel operation on all of the state variables simultaneously, and there is no question of different variables being of different age. In this section examples of nonlinear simulation will be provided using the transport aircraft in MATLAB code and the F-16 model in Fortran.

Example 4.7-1: Pitch-Rate CAS Nonlinear Simulation In this example the pitch-rate controller designed in Example 4.5-1 will be converted to a subprogram (i.e., a function subprogram or a subroutine subprogram) that can be linked with a nonlinear aircraft model, an integration routine, and a driver program to perform flight simulation. This subprogram must have access to the output variables of the aircraft model and the controller command inputs (e.g., as formal parameters, as "global" variables,

or through a "common" allocation of memory). A set of controller state variables that can be appended to the array of aircraft state variables must be used. The output of this subprogram is an array of derivatives, and they must be appended to the array of derivatives from the aircraft model.

The first statements in the controller subprogram are specific to the programming language and must define the variable types and how they are to be passed to and from the subprogram. The rest of the subprogram is essentially independent of the programming language and consists of the matrix state equations of Example 4.5-1 translated into individual state equations, as in Table 3.3-1. The aircraft model has thirteen state variables so here the controller states will be numbered from fourteen on and appended to the aircraft state vector. In Fortran, the code is:

```
subroutine FC(time,x,xdot)              ! x in, x-dot out
dimension x(*), xdot(*)                 ! assumed-size arrays
common/controls/thtl,el,ail,rdr,qcom    ! controls & commands
common/output/an,alat,ax,qbar,amach,vt,alpha,theta,q ! from a/c
el=-x(14)                               ! actuator state-->elevator
call f16(time,x,xdot)                   ! Aircraft model
xdot(15)= 10.0*(alpha-x(15) )           ! Alpha filter
xdot(16)= qcom - q                      ! PI integrator input
u= 1.5*x(16) - .5*q-.08*x(15)           ! Control law
xdot(14)= 20.2*(u - x(14) )             ! Elevator actuator
return
end
```

Values have already been assigned to the state variables when this subroutine is called, but the longitudinal control inputs must be assigned before the aircraft model equations can be executed. Therefore, the elevator control is assigned to the actuator state before calling the aircraft model. The lateral-directional controls and states will not be changed from their trim values. Throttle commands and the pitch-rate command "qcom" will be assigned in a separate subprogram. Control surface rate and deflection limits are not modeled; this will be done in later examples. Note that this controller and the aircraft model can be numerically linearized when linked together, and the Jacobian matrices will agree very accurately with the closed-loop matrices in Example 4.5-1. This provides a check for correct operation.

Accurate initialization will allow the longitudinal dynamics to be exercised without waiting for an initial transient to die out. The alpha filter state should be initialized with the trim value of alpha and the elevator state with the trim value of elevator deflection (both in degrees). The initial value of the error integrator state can be calculated as follows. From Figure 4.5-1 we see that the steady-state (no integrator input) elevator deflection is given by

$$-\delta_e = k_p z x_i - k_\alpha \alpha$$

When the trim values are inserted in this equation, the trim value of the integrator output is found to be $x_i = 0.6186$. The aircraft trim data file can now be augmented with the initial conditions for the three controller states.

A simulation of the F-16 aircraft model, with this controller, will now be used to illustrate some points about controller design. The following discrete-time subprogram was used to provide simulation commands.

```
subroutine DISCRETE(time,TS,x,xdot,)
dimension x(*), xdot(*)
common/controls/thtl,el,ail,rdr,qcom

if (time.lt. 10.0) then
   qcom= 0.0
else if (time.lt. 20.0) then
   qcom= 8.65
   thtl= 1.0
else if (time.lt. 50.0) then
   qcom= 0.0
else
   qcom= 10.0
end if
return
end
```

Figure 4.7-1 shows the vertical-plane trajectory produced by the commands, and Figure 4.7-2 shows the pitch-rate response. The aircraft is given full throttle and a

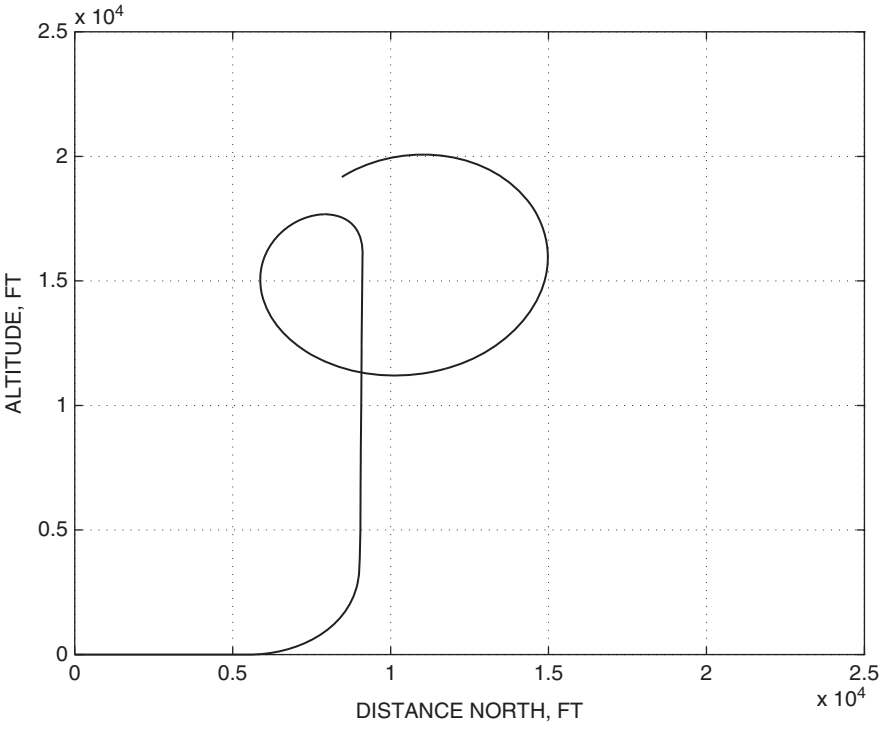

Figure 4.7-1 Aircraft trajectory in the vertical plane.

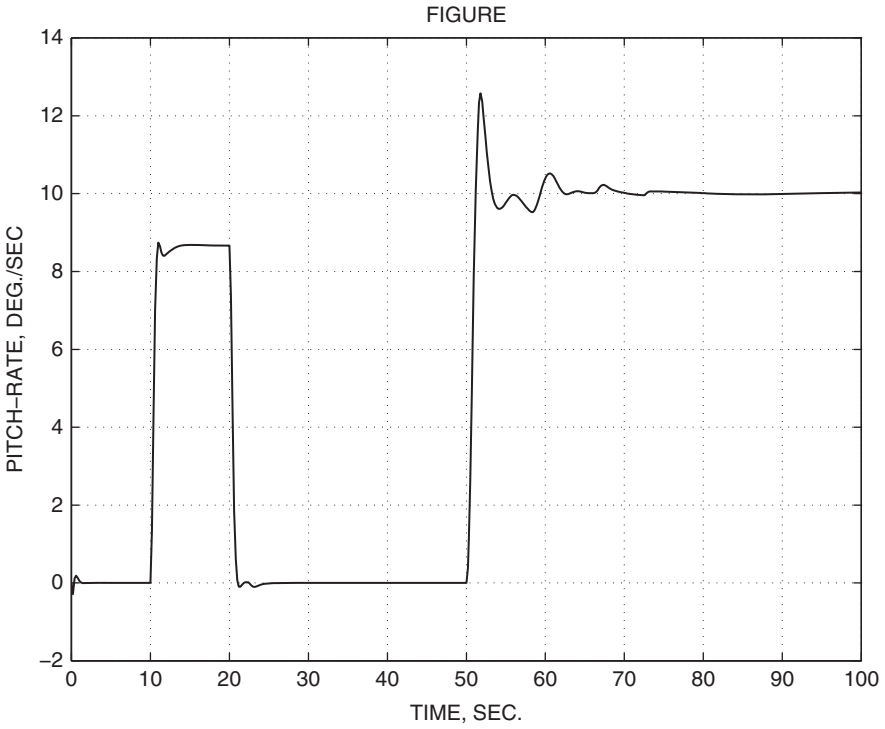

Figure 4.7-2 Aircraft pitch-rate response along the trajectory.

pitch-up command at $t = 10$ s; the pitch-rate command has been adjusted to bring the aircraft vertical at $t = 20$ s. At $t = 50$ s the airspeed has fallen to about 300 ft/s and the altitude is approximately 16,000 ft; therefore, the flight conditions are greatly different from the controller design conditions (sea level and 502 ft/s). The pitch-rate response has a large overshoot at $t = 50$ s because of the off-nominal design conditions. The aircraft dynamics change with flight conditions as described in Section 4.2, and in a practical controller design, the gain coefficients would be "*gain scheduled*" as functions of dynamic pressure and/or Mach number. The time of flight was 100 s for the trajectory shown, and the lateral-directional dynamics did not become significantly involved in the motion. The sideslip angle peaked up to about 0.1° after the pitch-over command at $t = 50$ s but then returned to very small values. The angle of attack reached a peak of approximately 15° at $t = 55$ s. ■

Example 4.7-2: Lateral-Directional CAS Nonlinear Simulation. In this example the lateral-directional controller designed in Example 4.5-3 is programmed for nonlinear simulation and used, together with the pitch-rate controller from Example 4.7-1, to provide complete 6-DoF control. The controller code is:

```
subroutine FC(time,x,xd)
dimension x(*), xd(*)
real m
```

```
common/controls/thtl,el,ail,rdr,pcom,qcom,rcom
common/output/an,ay,ax,qbar,m,alpha,beta,phid,thtad,
  & pd,qd,rd                          ! d means degree units
el =-x(1)                             ! actuator state-> el
ail=-x(4)                             ! : : : : :-> ail
rdr=-x(5)                             ! : : : : :-> rdr
call f16(time,x(7),xd(7))             ! aircraft dynamics
xd(3)= qcom- qd                       ! error integrator
u = 1.5*x(3)-.5*qd-.08*x(2)           ! pitch control law
xd(1)= 20.2*(u-x(1))                  ! elevator actuator
xd(2)= 10.0*( alpha- x(2) )           ! alpha filter
ua = 0.2*(pcom-pd)                    ! roll control law
xd(4)= 20.2*( ua- x(4) )              ! aileron actuators
ari = (0.13*x(2)- 0.7)*ua             ! ARI
rs = rd- pd*x(2)/57.3                 ! yaw-rate feedback
xd(6)= rs- x(6)                       ! washout
err= rcom -.8*xd(6)- 10.0*ay          ! yaw control law
xd(5)= 20.2*( err + ari- x(5) )       ! rudder actuator
return
end
```

This time the controller states are numbered first and the aircraft states are appended to these. The nominal flight condition of Table 3.6-3 was used, and the six compensator states were included in the trim data file. The actuator states must be set to the trimmed values of the corresponding aircraft controls, and the alpha filter state to the value of alpha in degrees. The other controller states can be set to zero since the rest of the controller is linear.

A nonlinear simulation was chosen that would exercise the ARI through high-alpha and fast roll rates yet be easily preprogrammed for non-real-time simulation. The trajectory chosen was a pull-up into a vertical loop, with a 180° roll at the top of the loop and continuing into a second vertical loop. The preprogrammed commands were:

```
subroutine DISCRETE(time,ts,x,xd)
dimension x(*),xd(*)
common/controls/thtl,el,ail,rdr,pcom,qcom,rcom

if (time.lt. 5.0) then
    qcom= 0.0
    pcom= 0.0
    rcom= 0.0
else if (time.lt. 15.0) then
    qcom= 15.0                        ! Pull up at 15 deg/s
    thtl= 1.0                         ! at full throttle
else if (time.lt. 17.0) then
    pcom= 150.0                       ! rolling for 2 sec.
else
    pcom= 0.0
end if
return
end
```

The alpha filter and actuator states were initialized exactly with the correct initial conditions, but the other controller states were left uninitialized, so the first 5 s of the flight was used to let any transients die away. Full throttle and a 15-deg/s pitch-rate command are applied at $t = 5$ s, and then a roll-rate command pulse is applied between 15 s and 17 s. The desired roll rate is therefore 90 deg/s, but because of the finite error of the type-0 roll-rate loop, the rate command had to be adjusted by trial and error to achieve the 180° roll.

An elevation view of the trajectory is shown in Figure 4.7-3*a*. The first loop corresponds to a normal acceleration of about 4 *g*, and the aircraft speed decreases roughly linearly from 500 ft/s at 5.0 s to 270 ft/s at 24 s (near the top of the second loop). Figures 4.7-3*b* and *c* show angle of attack, roll attitude, and pitch attitude. Alpha increases rapidly as the loop is started, remains roughly constant to provide the centripetal acceleration while the pitch attitude is between 45° and 90°, and then starts to fall off as gravity helps to provide the centripetal acceleration. During the second loop alpha rises to a larger peak, because the airspeed has dropped considerably by then.

The roll angle of 0° suddenly becomes a roll angle of 180° as the aircraft passes through the vertical-attitude condition, and this wings-level attitude is held until the roll is started at 15 s. The attitude angles are computed by integrating the angular rates

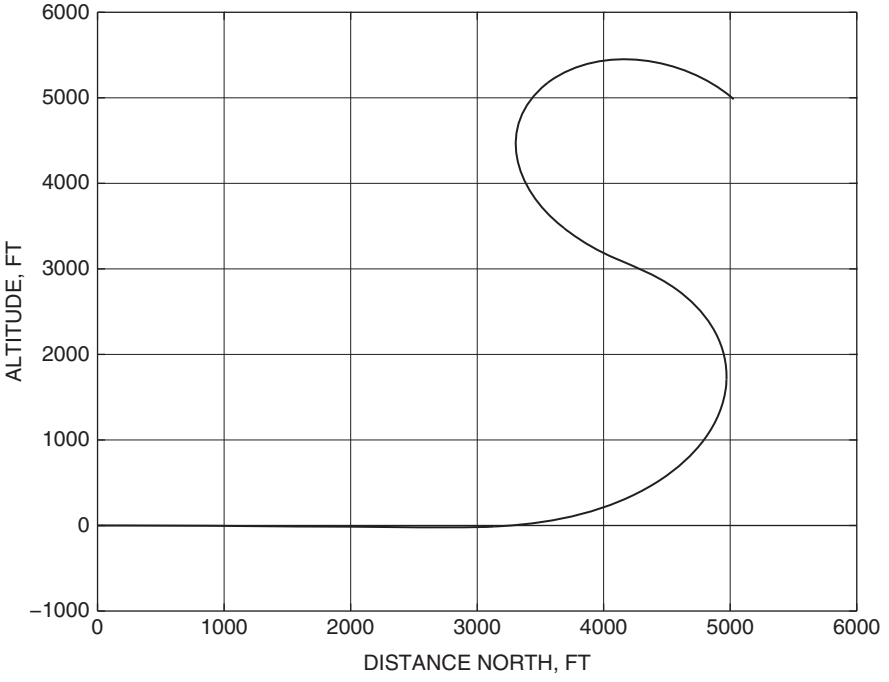

Figure 4.7-3*a* Aircraft trajectory in the vertical plane.

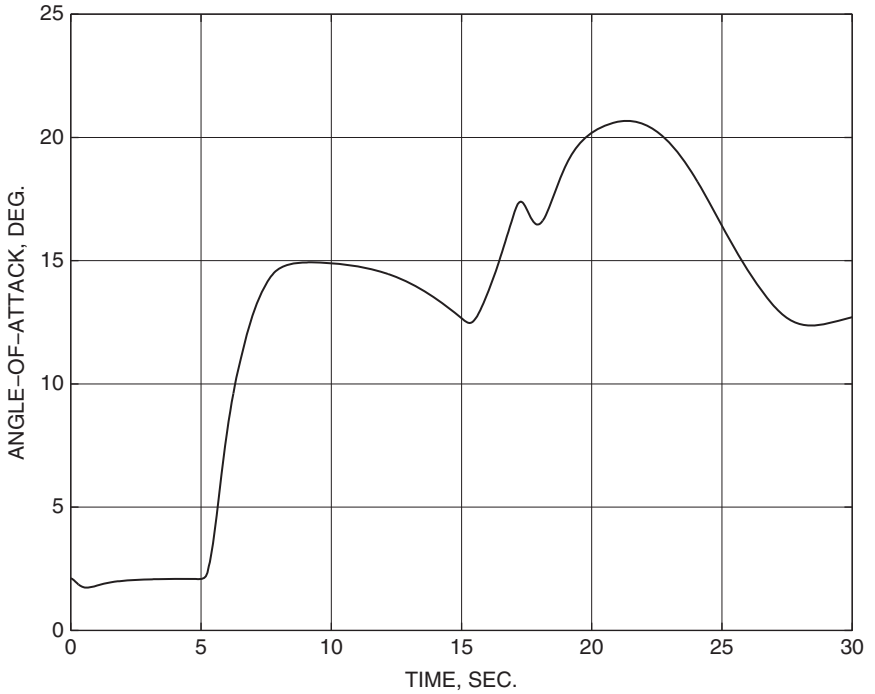

Figure 4.7-3*b* Angle of attack versus time.

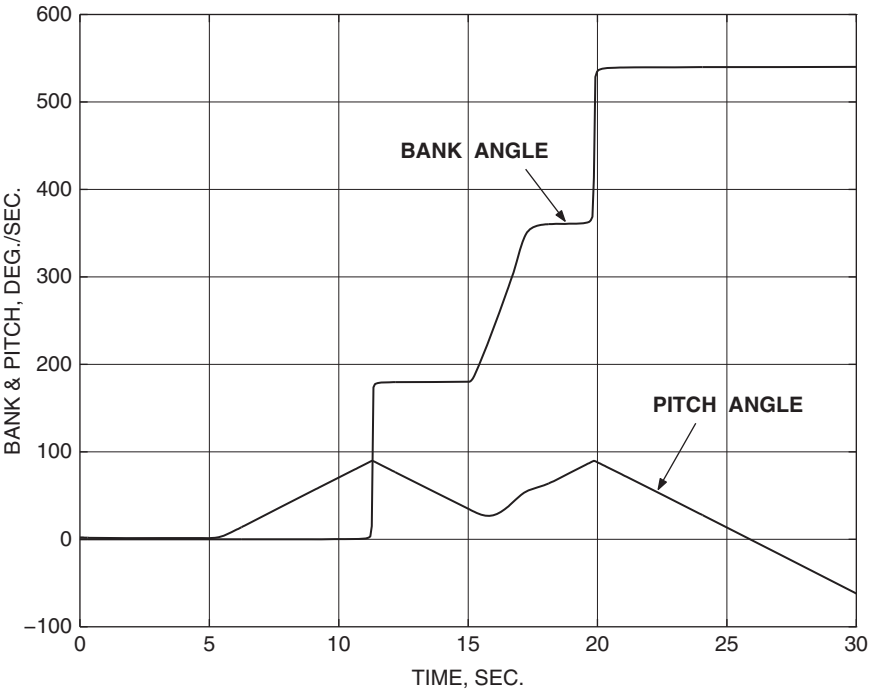

Figure 4.7-3*c* Aircraft roll and pitch angles along trajectory.

(state derivatives), not from trigonometric functions, so the roll angle may contain multiple 360° ambiguities, depending on how the angular rates behave.

Figure 4.7-3*d* shows the fast roll-rate response and the corresponding yaw rate that is generated by the ARI. The pitch rate undergoes a positive perturbation during the roll, and this is due to the nose-up pitching moment generated by inertia coupling. Figure 4.7-3*e* shows the positive increment in elevator deflection that is generated by the longitudinal control system to counteract the inertia-coupling moment. As stated earlier, a major problem when rolling rapidly at still higher angles of attack is that the longitudinal control surfaces may be unable to generate a large enough nose-down moment.

In this example the elevator deflections are quite small, but the aileron and rudder deflections are large. This is due to the combination of high demanded roll rate and low aileron effectiveness (because of the high alpha and relatively low dynamic pressure). It is also partly due to the fact that while the rudder is generating the required yaw rate, it is also generating a rolling moment that opposes the aileron rolling moment. The large peak deflections are due to the instantaneous demand for the high roll rate. Note that the aileron and rudder deflection rates may have reached or exceeded the capabilities of their actuators; this concern is addressed later.

Figure 4.7-3*f* shows that the control system has done an excellent job of keeping the sideslip angle small during this demanding maneuver. The sideslip excursions are

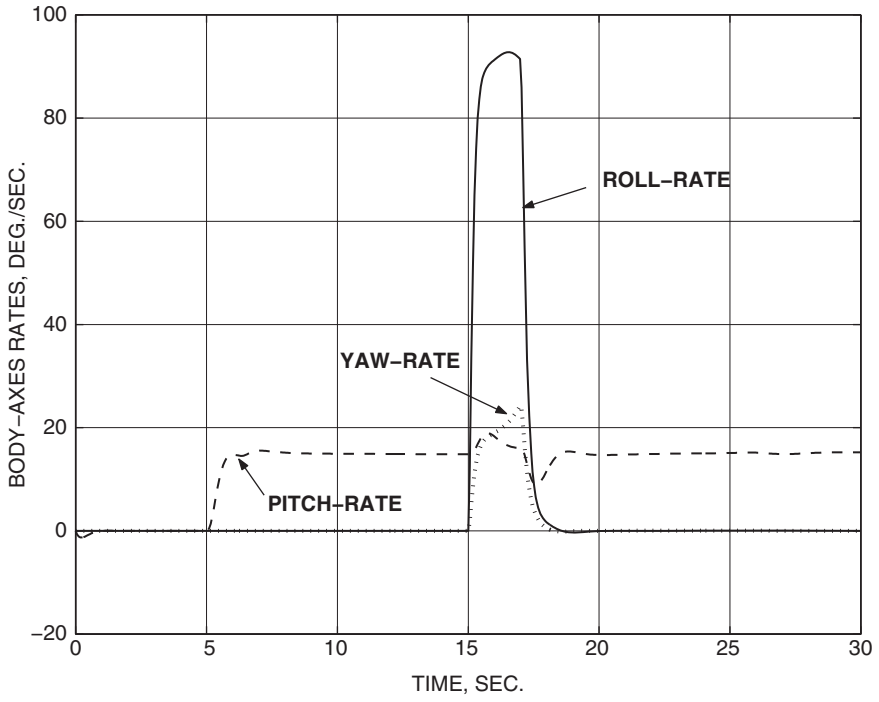

Figure 4.7-3*d* Aircraft body-axes angular rates along trajectory.

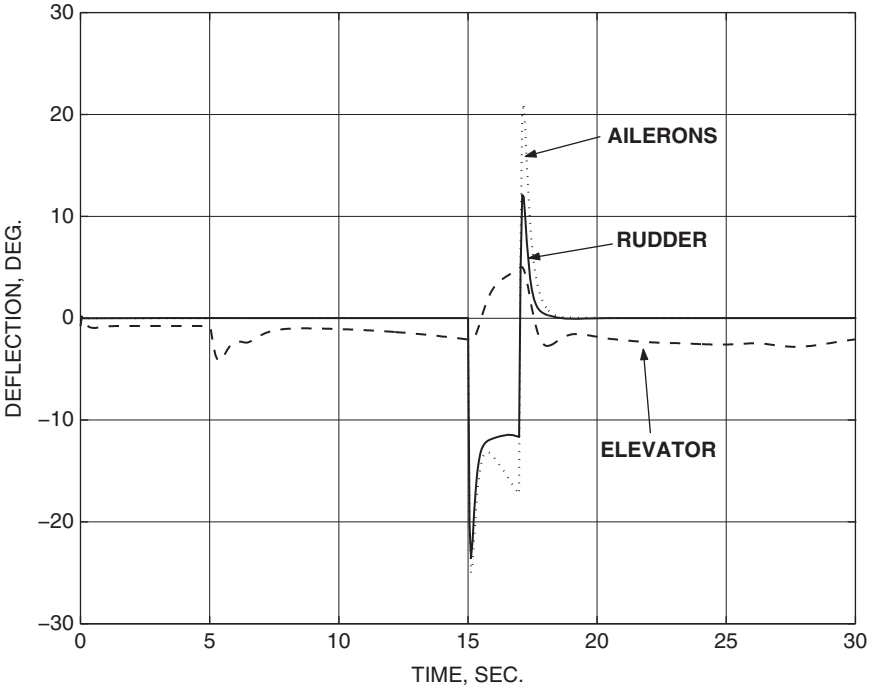

Figure 4.7-3*e* Control surface deflections along trajectory.

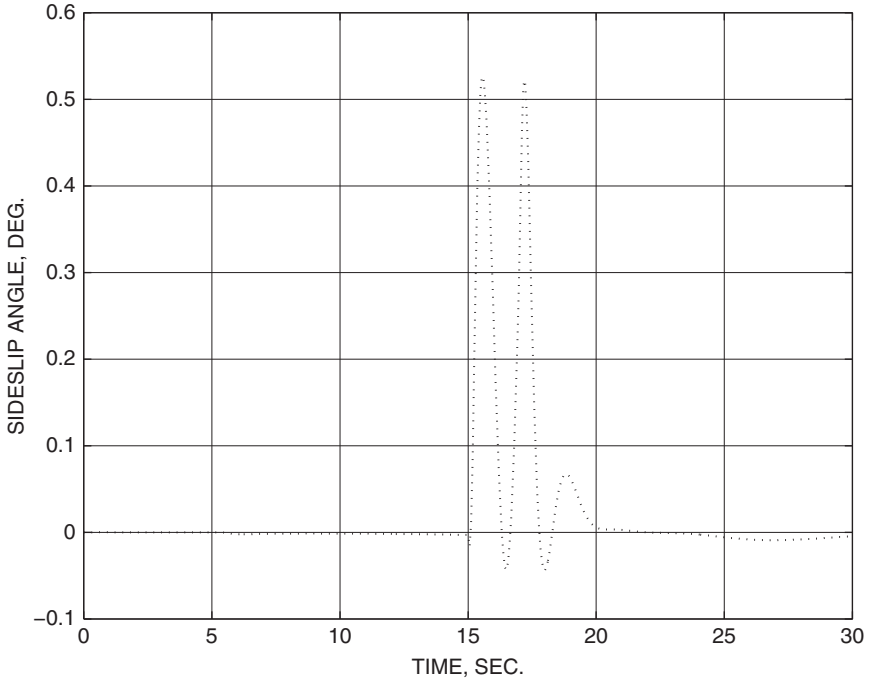

Figure 4.7-3*f* Sideslip angle variation along trajectory.

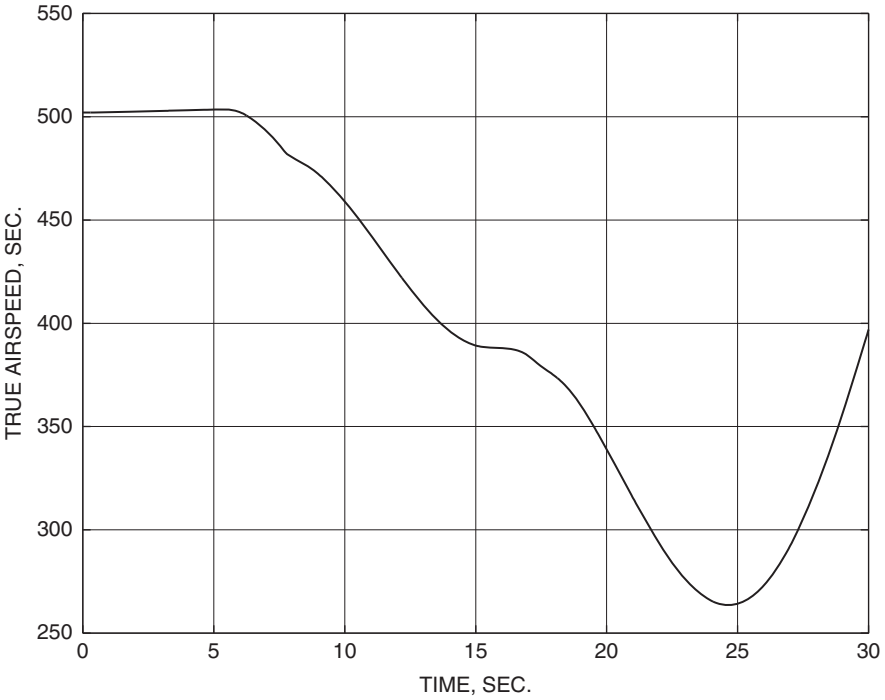

Figure 4.7-3*g* True airspeed variation along trajectory.

biased positively, that is, toward adverse beta. This is desirable in general; a combination of adverse and proverse beta tends to excite the dutch roll mode. The ARI gain is quite critical, and the values used are close to optimal. Larger values will produce a single negative beta excursion and a single positive beta excursion that are more nearly symmetrical about zero but considerably larger in magnitude. Figure 4.7-3*g* shows the variation of airspeed with time. The maneuvers have caused the speed to fall continuously until the top of the second loop is passed, despite full throttle being used throughout. The twofold reduction in speed will cause a fourfold reduction in dynamic pressure.

Finally, note that the performance may appear satisfactory for these flight conditions, but the design must be evaluated at other altitude/speed combinations. Gain scheduling with Mach number will probably be required, and much more comprehensive simulation is necessary before the design can be considered practical. ■

Example 4.7-3: Simulation of Automatic Landing This example will simulate longitudinal control for an automatic landing of the transport aircraft model using the longitudinal controller designed in Example 4.6-4. The MATLAB controller code

can be constructed quite easily from the code in Example 4.6-4 with the help of Figure 4.6-10 and Table 3.3-1:

```
% GLIDE.M Glide-Slope Controller for Ex. 4.7-3
function [xd]= glide(time,x,u)
global xd
u(2) = -x(8);                          % set elevator
u(1) = x(11);                          % set throttle
[xd] = transp(time,x,u);               % call aircraft
xd(14)= 0.0 - x(7);                    % d-loop error
dpi = xd(14) +.18*x(14);               % PI compensation
xd(13)= dpi - 5.0*x(13);               % Phase Lead
thcom = xd(13) + 0.5*x(13);            % theta command

xd(9) = thcom - 57.29578*x(3);         % Pitch error
tpi = xd(9) + 0.2*x(9);                % PI integrator
xd(10)= tpi - 14.0*x(10);              % Phase Lead
qcom = 40.0*(xd(10) + 1.4*x(10));      % Pitch-rate command
qerr = qcom - 57.29578*x(4);           % q error
xd(8) = 10.0*(qerr-x(8));              % El. actuator

ev = 250 - x(1);                       % speed error
xd(12)= ev - 10.0*x(12);               % lead compensator
ut = 10.0*(ev - 9.0*x(12));            % lead comp.
xd(11)= 0.2*(ut - x(11));              % throttle lag
```

and the sequence of .M files involved in the simulation is:

```
NLSIM.M    - Nonlinear simulation from Chap. 3
RK4        - Fourth-order Runge-Kutta from Ch. 3
GLIDE.M    - Controller routine above
TRANSP.M   - Transport-Aircraft model from Ch. 3
ADC.M      - Atmosphere model for Transp. Aircraft
```

The chosen initial conditions were level flight at $V_T = 250$ ft/s, $h = 1500$ ft, with flaps and gear deployed, and $x_{cg} = 0.25$. An initial-condition data file can be obtained by using TRIM.M (Chapter 3), as follows. In the steady state all of the integrator inputs in Figure 4.6-10 are zero, and it is easy to write algebraic equations for all of the controller variables in terms of the aircraft states and controls. When these equations are included in the cost function, the trim program will produce an initial condition file for all fourteen controller and aircraft states (see Example 4.7-4). In the transport aircraft model the reference flight-path angle was programmed to change from zero to $-2.5°$ at $t = 15$ s to represent glide-path capture.

Figure 4.7-4*a* shows the trajectory for 50 s of simulated flight; the aircraft starts out in level flight with no transient because the controller was accurately initialized. Figure 4.7-4*b* shows the deviation from the glide path. Figure 4.7-4*c* shows the

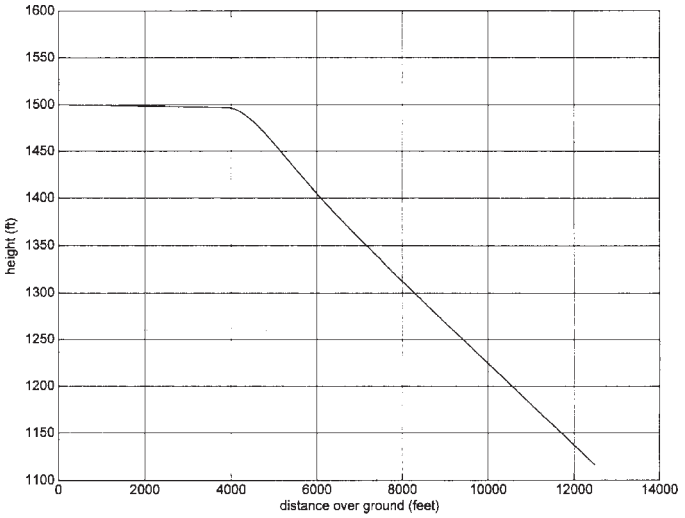

Figure 4.7-4*a* Automatic landing; elevation profile.

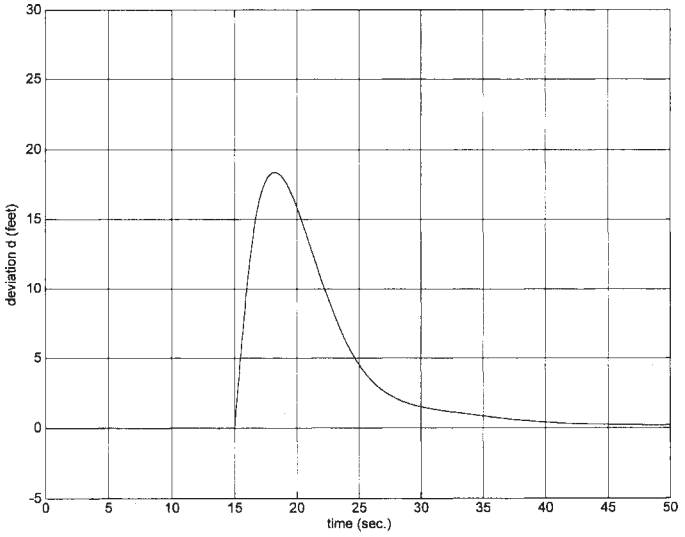

Figure 4.7-4*b* Automatic landing; deviation from glide path.

behavior of alpha, pitch attitude, and elevator deflection, and Figures 4.7-4*d* and *e* show, respectively, the corresponding variation of throttle position and airspeed. It is evident that the airplane is driven onto the glide path quickly and smoothly, without large excursions in pitch attitude. Airspeed is held very nearly constant and the throttle is changed smoothly and gently. Because of the tight control,

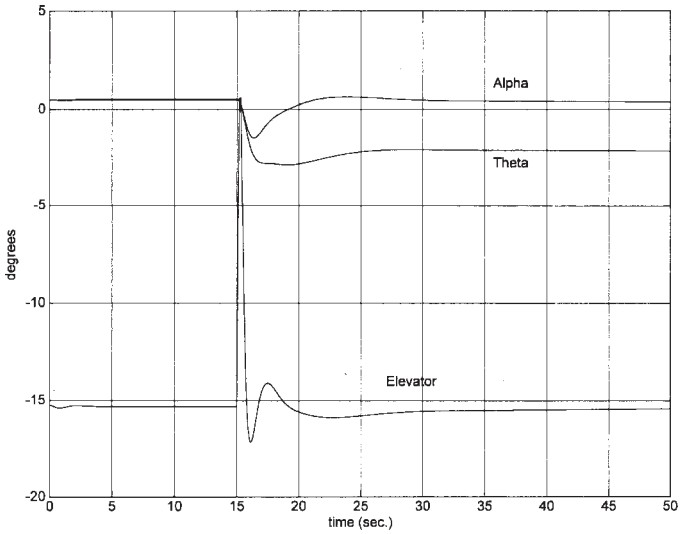

Figure 4.7-4*c* Automatic landing; controlled variables.

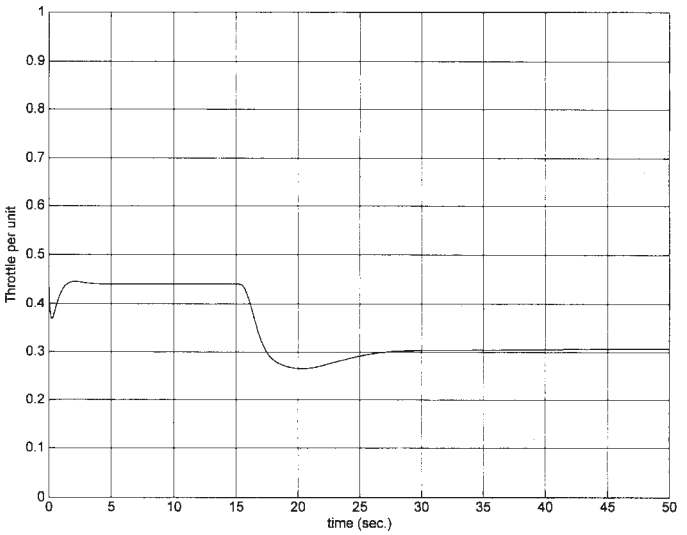

Figure 4.7-4*d* Automatic landing; throttle variation.

the elevator shows some rapid excursions, which could cause rate limiting in a real actuator.

The final component of this design is the automatic "flare" control that makes the aircraft begin to level out as the altitude approaches zero and touch down with an acceptably small rate of descent. This is described in the following subsection.

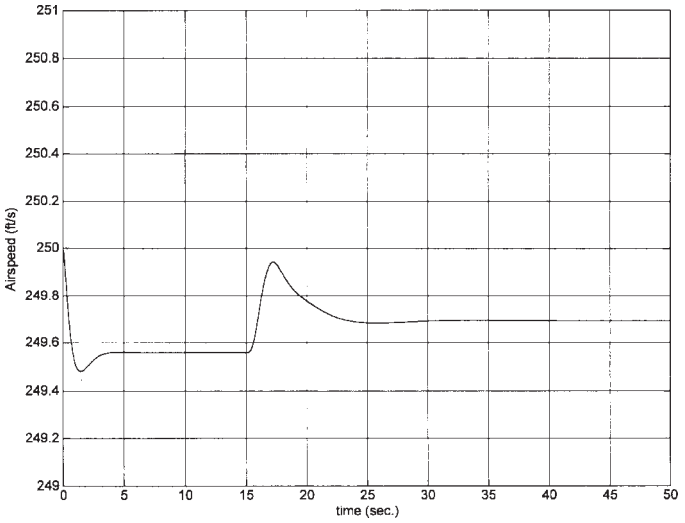

Figure 4.7-4*e* Automatic landing; airspeed variation.

■

Flare Control

At an altitude of about 50 ft above the runway the automatic landing system must start to reduce the rate of descent of the aircraft, achieve the correct pitch attitude for landing, and begin to reduce the airspeed. This portion of the trajectory is called the landing flare, and the geometry of the flare is illustrated in Figure 4.7-5. On the glide path the aircraft is descending at a rate of 10 ft/s or greater and will hit the ground hard if the flare is not executed. The rate of descent must be reduced to less than about 2.0 ft/s by touchdown. The pitch attitude angle will depend on the airspeed and will be only a few degrees for a large jetliner; military aircraft may land with large pitch angles to make use of aerodynamic braking. Altitude rate ($\dot{h} = V_T \sin\gamma$) is a natural choice for the controlled variable since it determines the impact, can be derived in the radar altimeter, makes the control system independent of ground effect and wind disturbances, and involves control of one less plant integration than altitude.

Modern digital-controller-based automatic landing systems can yaw the aircraft to deal with cross-winds while lining up the runway, decrab the aircraft and dip a wing

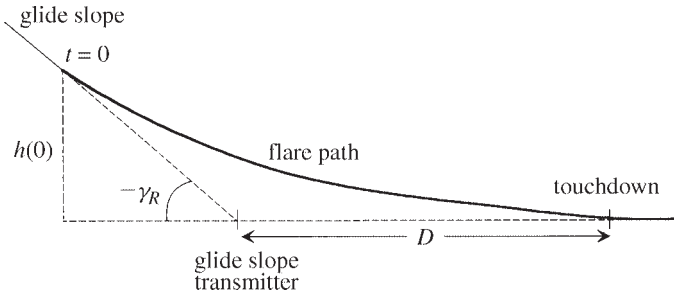

Figure 4.7-5 Landing-flare geometry

to keep the lateral velocity component small, and level the wings immediately before touchdown.

Example 4.7-4: Automatic Flare Control In this example we will use altitude rate from the aircraft model as the controlled variable and switch from the glide-path controller to the flare controller when the altitude reaches 50 ft. The speed loop will continue to operate with the same command input. Switching from one controller to another can cause large transients in the aircraft states, which is disconcerting and dangerous so close to the ground. To avoid this, the flare controller must be initialized with the final conditions on the glide slope and then commanded to go smoothly to the new altitude rate. Here we have used only a simple controller with one additional state, $x(15)$, which is initialized to zero. Thus, the following code shows only a PI compensator and a gain, with a step command of -2 ft/s, for the altitude-rate controller. Some logic (variable "MODE") is used to ensure that control does not momentarily switch back to the glide-path controller if integration errors or transients cause a fluctuation in altitude at changeover. The airspeed on the glide path was chosen to give the aircraft a slightly pitched-up attitude at touchdown and was 235 ft/s (139 knots). The controller code is as follows:

```
          % FLARE.M Glide-Slope & Flare Controller
function [xd]= flare(time,x,u);
global  xd mode
u(2)    = -x(8);                    % set elevator
u(1)    = x(11);                    % set throttle
[xd]    = transp(time,x,u);         % call aircraft
h       = x(5);                     % altitude
vcom=235;                           % commanded speed
if time<1
    mode=0;                         % glideslope mode
end
if h>50 & mode==0                   % d-controller
   xd(14)= 0.0 - x(7);              % integrate d-error
   dpi= xd(14) + .18*x(14);         % PI comp.
   xd(13)= dpi - 5.0*x(13);         % lead compensation
   thcom = xd(13) + 0.5*x(13);      % theta command
   xd(15)=0.;                       % for flare controller
elseif h<=0 | mode==2               % roll-out mode
   mode=2;
   xd=zeros(1,15);
   thcom=0;
elseif h<=50 | mode==1              % flare controller
   mode=1;                          % lock out other modes
   hdot=-2;                         % sink-rate command
   xd(15)= ( hdot - xd(5) );        % PI integrator
   thcom=.1*( xd(15) +.5*x(15) );   % C. L. Zero at-.5
   xd(13)=0;
end
xd(9) = thcom - 57.29578*x(3);      % integrate pitch error
tpi = xd(9) + 0.2*x(9);             % PI compensation
xd(10)= tpi - 14.0*x(10);           % phase-lead comp.
qcom = 40* ( xd(10) + 1.4*x(10) );  % pitch-rate command
```

```
qerr = qcom - 57.29578*x(4);        % pitch-rate error
xd(8) = 10.0 * (qerr - x(8) );      % Elevator actuator

ev = vcom - x(1);                   % Autothrottle code
xd(12)= ev - 10.0*x(12);            % phase-lead pole
ut = 10.0*(ev - 9.0*x(12) );        % phase-lead zero
xd(11)= 0.2*(ut - x(11));           % throttle servo
```

and the cost function used with the trim program was:

```
% Cost Function for 3-DOF Aircraft
function [f]=ssland(s);
global x u gamma
u(1)= s(1);              % throttle
u(2)= s(2);              % elevator
x(2)= s(3);              % alpha
x(3)= x(2) + gamma;      % theta
x(8)= -u(2);
x(10)= x(8)/(40*1.4);
x(9)= 14*x(10)/.2;
x(13)= 57.29578*x(3)/.5;
x(14)= 5*x(13)/.18;
x(11)= u(1);
x(12)= x(11)/10;
x(15)= 0.0;              % flare control state
time= 0.0;
[xd]=transp(time,x,u);
f= xd(1)^2 + 100*xd(2)^2 + 10*xd(4)^2;
```

A nonlinear simulation of the controller, with the transport aircraft model, was started from an initial state corresponding to an altitude of 300 ft on the glide-path simulation of Example 4.7-3. Figures 4.7-6*a* through *c* show the trajectory,

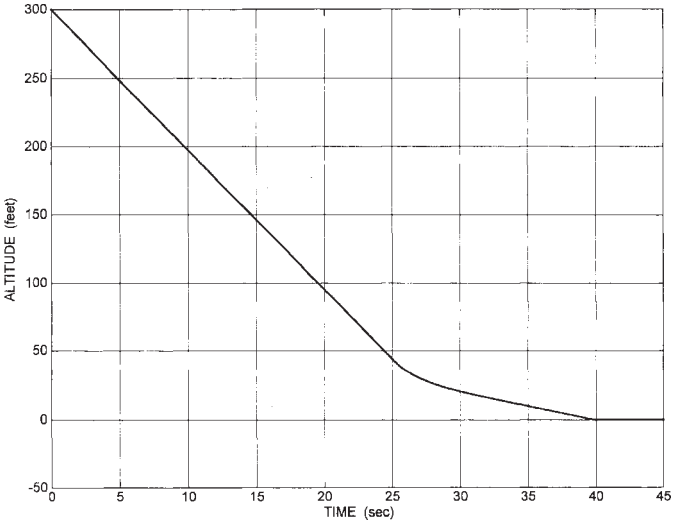

Figure 4.7-6*a* Automatic landing; glide slope and flare trajectory.

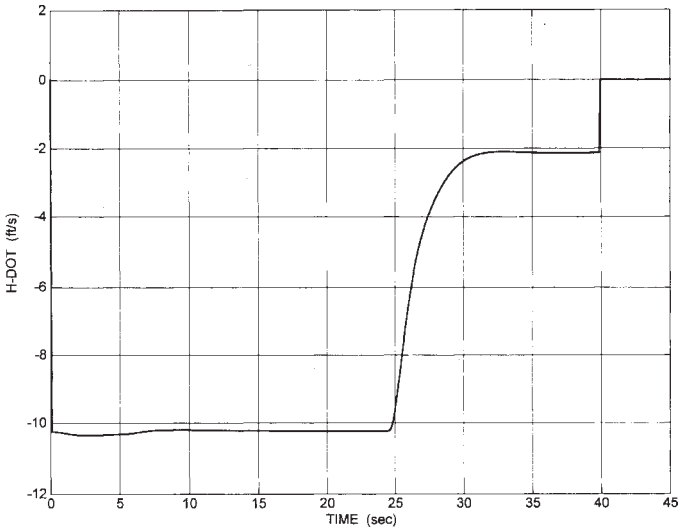

Figure 4.7-6*b* Altitude rate during flare.

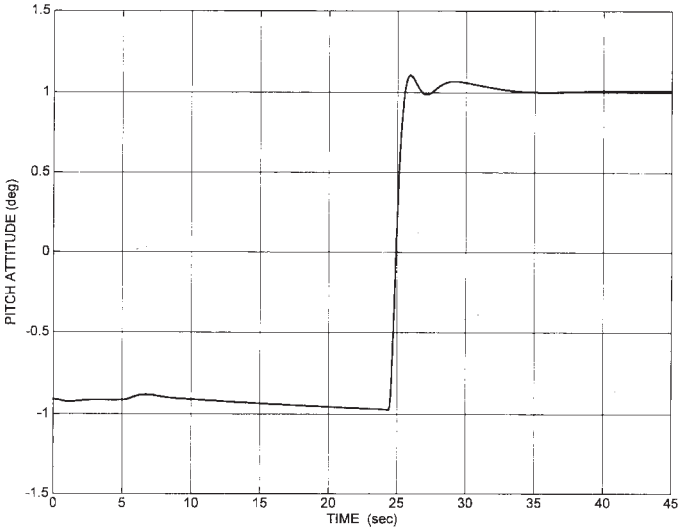

Figure 4.7-6*c* Pitch attitude during flare.

vertical speed, and pitch attitude. The vertical speed and pitch attitude have reached the desired values well before touchdown. The pitch-attitude change is faster than necessary; the small well-damped oscillation in pitch would be barely noticeable to the passengers. ■

Example 4.7-5: A Roll-Angle-Steering Control System The controller routine for the lateral-directional CAS is easily modified to include the roll angle feedback and the turn compensation. The controller and command Fortran routines are shown below.

```
subroutine FC(time,x,xd)
dimension x(*), xd(*)
real m
common/controls/thtl,el,ail,rdr,bank,qcom,rcom
common/output/an,ay,ax,qbar,m,alpha,beta,phid,thtad,
& pd,qd,rd
el = -x(1)
ail= -x(4)
rdr= -x(5)
call f16(time,x(7),xd(7))
qcom= rd*tan(phid/57.29578)      ! turn compensation
xd(3)= qcom - qd
u= 1.5*x(3) - .5*qd - .08*x(2)
xd(1)= 20.2*(u-x(1))
xd(2)= 10.0*( alpha - x(2) )
ua = 1.0*(bank-phid -.2*pd)      ! bank angle control law
xd(4)= 20.2*( ua - x(4) )
ari = (0.13*x(2) - 0.7)*ua
rs = rd - pd*x(2)/57.3
xd(6)= rs - x(6)
err= rcom - .8*xd(6) - 10.0*ay
xd(5)= 20.2*( err + ari - x(5) )
return
end

subroutine DISCRETE(time,ts,x,xd)
dimension x(*),xd(*)
common/controls/thtl,el,ail,rdr,bank,qcom,rcom
if (time.ge. 20.0) Then
  bank= -70.0
else if (time.ge. 5.0) Then
  bank= 70.0
else
  bank = 0.0
  qcom = 0.0
  rcom = 0.0
end if
return
end
```

The same initial-condition data used for the lateral-directional CAS were used with this controller, and a simulation was flown using the discrete-time commands shown above. Figure 4.7-7*a* shows the ground track of the aircraft in response to these commands. The altitude decreased by about 600 ft during the 30-s simulation because of

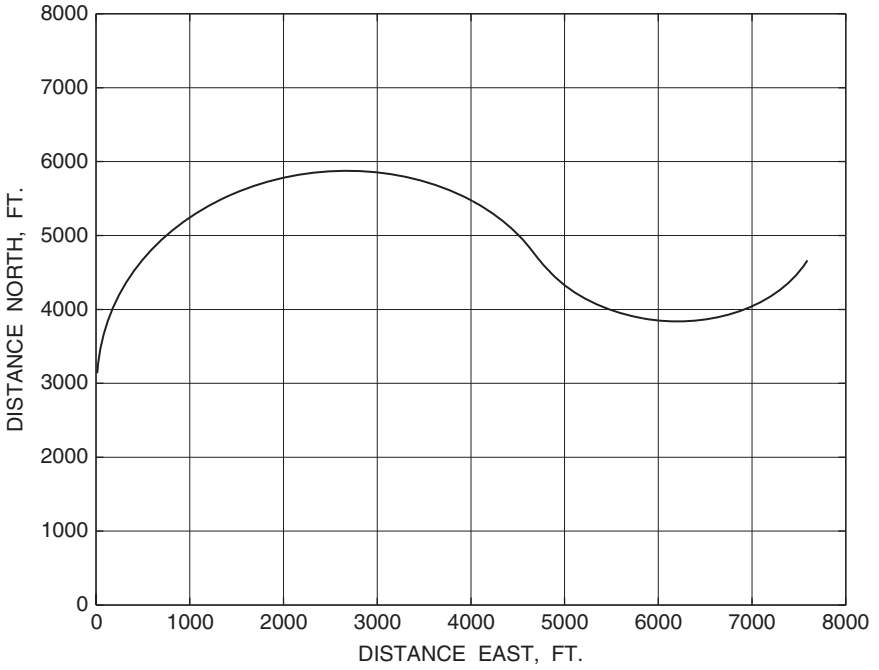

Figure 4.7-7*a* Ground track during roll angle steering.

the open-loop turn compensation and the finite control error of the lateral-directional control systems. The speed decreased by about 200 ft/s during the simulation, because of the maneuvers.

Figures 4.7-7*b*, *c*, and *d* show, respectively, the fast well-damped roll angle response, the angle of attack, and the sideslip angle. The aileron and rudder deflections are shown in Figures 4.7-7*e* and *f*; these show short-duration deflections that are well beyond the limits of the control surfaces and raise the following important points.

First, the simulation results may be unrealistic if the control surface rate and deflection limits are not modeled. Second, control system limiting will be caused by the abrupt large-amplitude commands and the high gains that have been used in the roll angle control. This is not necessarily a problem if the system response is still acceptable, since the fastest possible roll response may be desired, and the high gains also provide a small control error for low-amplitude inputs. Third, the airplane handling qualities are the most important consideration, and in this situation the stick prefilter and the maximum roll rate of the airframe will play a major part in determining the pilot's opinion of the roll performance.

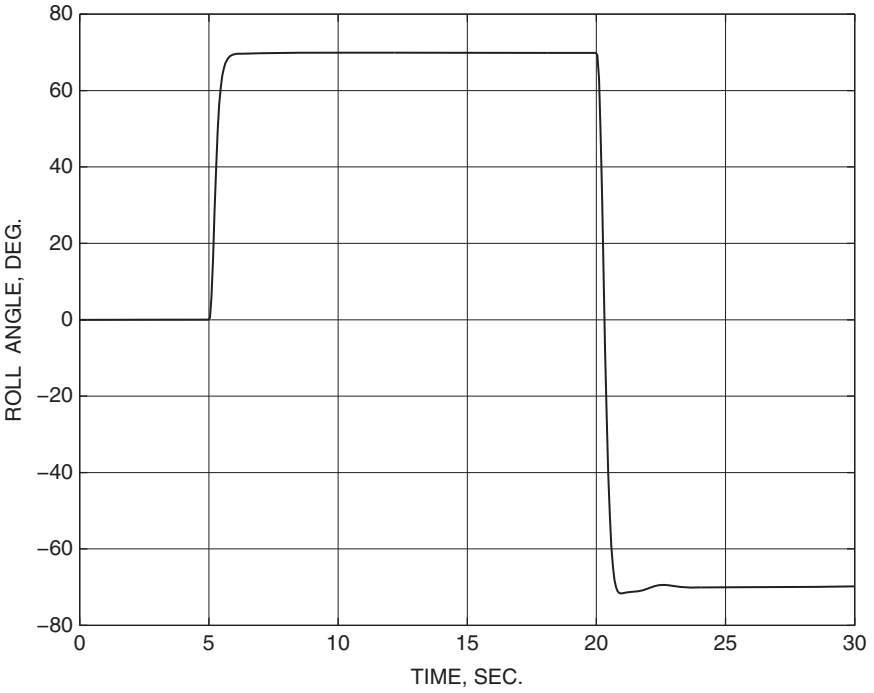

Figure 4.7-7*b* Bank angle during roll angle steering.

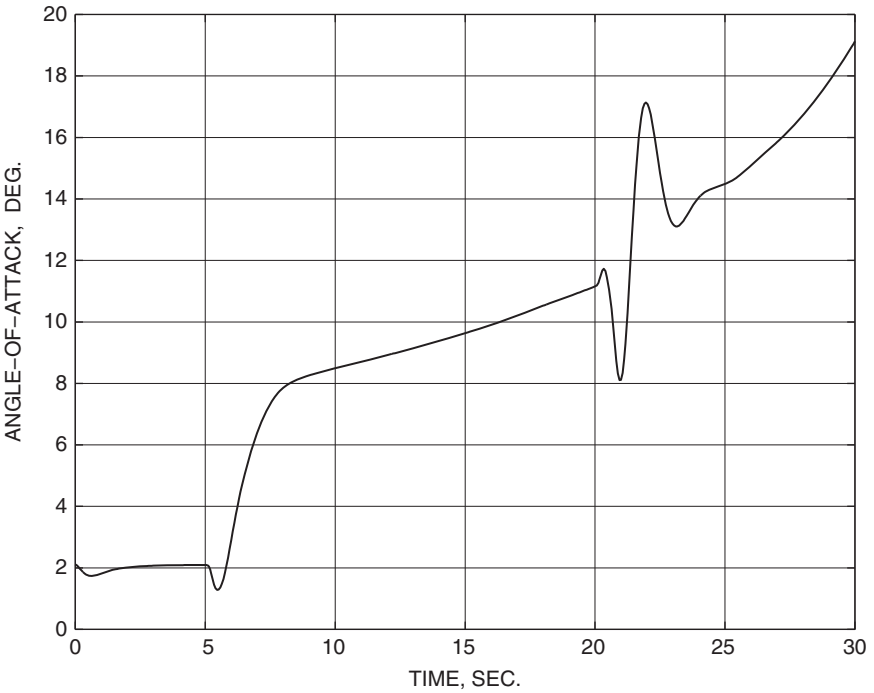

Figure 4.7-7*c* Angle of attack during roll angle steering.

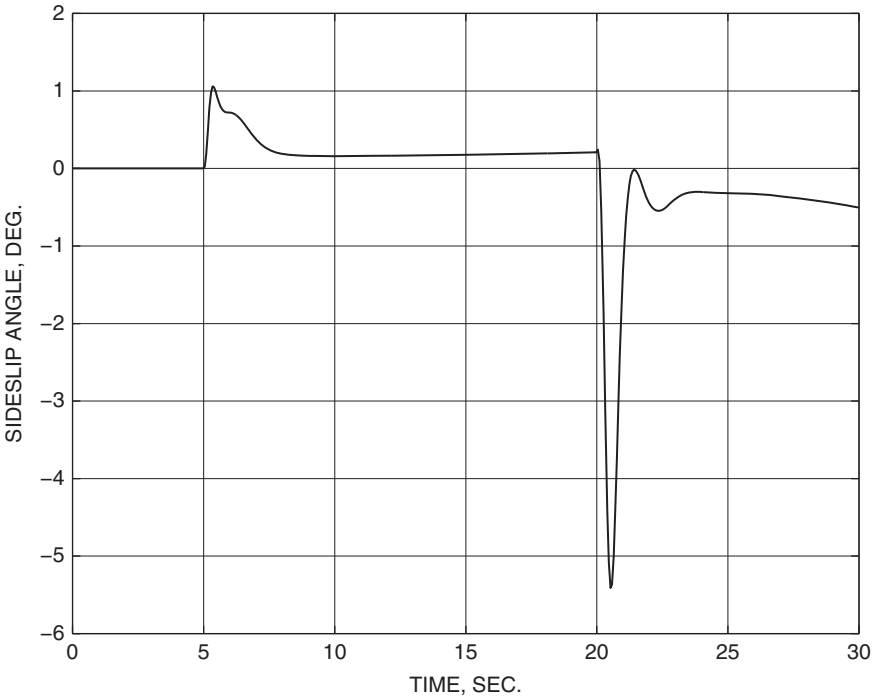

Figure 4.7-7*d* Sideslip angle during roll angle steering.

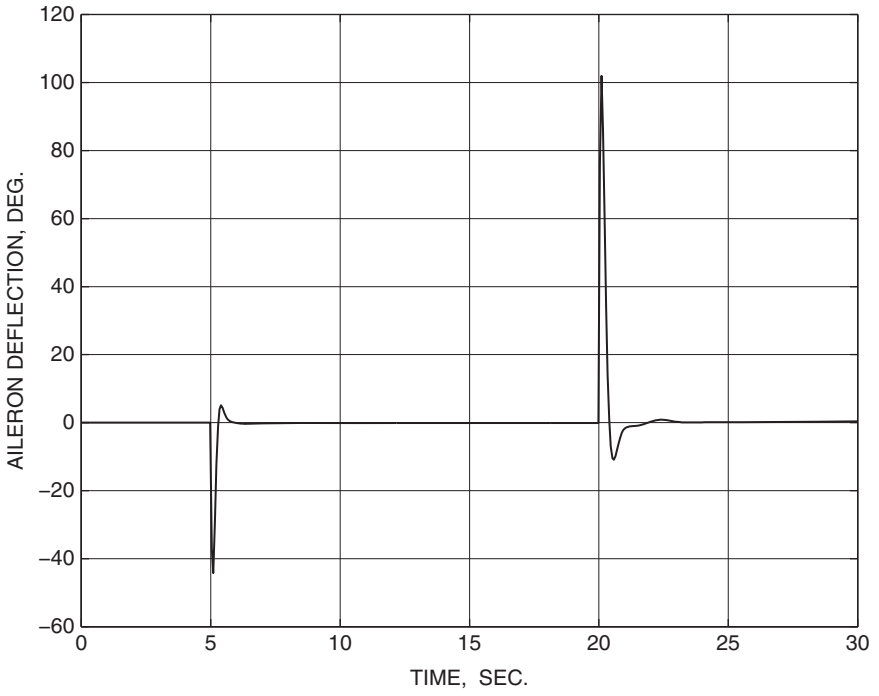

Figure 4.7-7*e* Aileron deflection during roll angle steering.

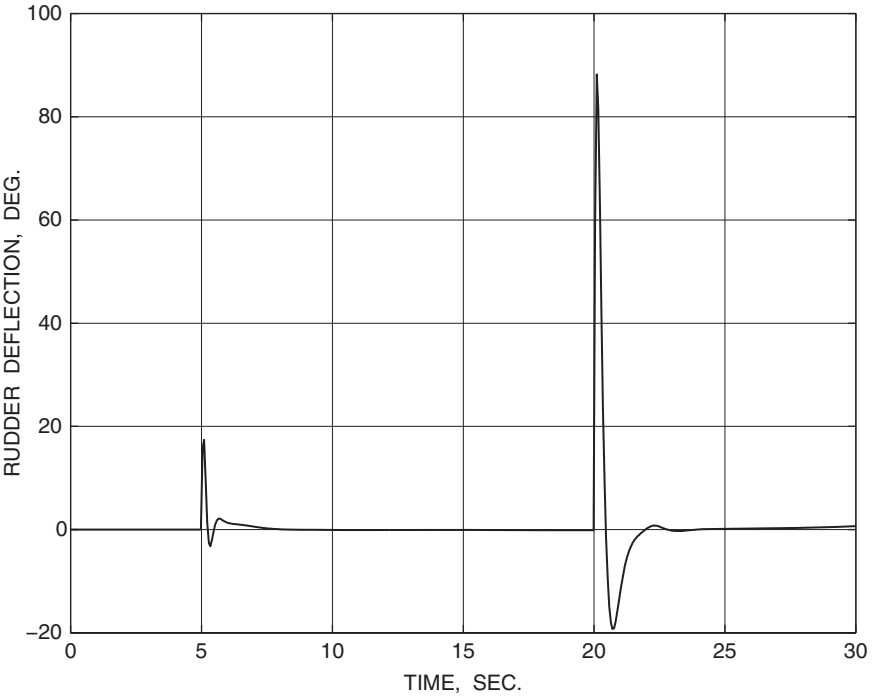

Figure 4.7-7*f* Rudder deflection during roll angle steering.

■

Example 4.7-6: Simulation of a Controller with Limiters Here we deal with "hard limiting" as distinct from merely nonlinear behavior. To simulate limiting behavior the control variables, state variables, and state derivatives must be modified when the limiting occurs. Other variables are essentially dummy variables that are assigned according to the states and controls. Rate limiting can be simulated by simply "clamping" the appropriate state derivative when its maximum value is reached. State-variable limits must be dealt with by modifying their derivatives also. When a state variable reaches a limit, a nonzero derivative is allowed only if it is in the direction that takes the state variable off the limit. This is related to the integrator wind-up problem described in Chapter 3. In this example, the code used for Example 4.7-2 has been modified by the addition of rate and deflection limits and is shown below. In-line comments have been added to explain the details.

The behavior of the controller, with limiters, is illustrated by a time-history simulation similar to that of Example 4.7-2, and the discrete-time commands are shown below. The integration step size was reduced to 1 ms in this simulation to capture the action of the limiters with sufficient accuracy. This can make the execution quite slow.

```
subroutine FC(time,x,xd)
dimension x(*), xd(*)
real m
common/controls/thtl,el,ail,rdr,pcom,qcom,rcom
common/output/an,ay,ax,qbar,m,alpha,beta,phid,thtad,pd,qd,
& rd
data erl,edl,arl,adl,rrl,rdl/60.0,25.0,80.0,21.5,120.0,30.0/
el = -x(1)
ail= -x(4)
rdr= -x(5)
call f16(time,x(7),xd(7))
xd(2)= 10.0*( alpha - x(2) )
xd(3)= qcom - qd
u= 1.5*x(3) - .5*qd - .08*x(2)
xd(1)= 20.2*(u-x(1))

if( abs(xd(1)) .gt. erl) then
   xd(1)= sign(erl, xd(1))            ! Elevator rate limit
end if
if(x(1) .gt. edl) then
 x(1)= edl                            ! Elevator + deflection limit
 if(xd(1) .gt. 0.0) xd(1)= 0.0        ! Stop integrating positively
 if(xd(3) .lt. 0.0) xd(3)= 0.0        ! clamp error integrator
else if (x(1) .lt. -edl) then
  x(1)= -edl                          ! Elevator - deflection limit
  if(xd(1) .lt. 0.0) xd(1)= 0.0       ! stop integrating negatively
  If(xd(3) .gt. 0.0) xd(3)= 0.0       ! clamp error integrator
else
  continue
end if

ua   = 0.2*(pcom-pd)
xd(4)= 20.2*( ua - x(4) )
if( abs(xd(4)) .gt. arl) then
   xd(4)= sign(arl, xd(4))            ! Aileron rate limit
end if
if(x(4) .gt. adl) then
   x(4)= adl                          ! Aileron deflection limit
   if(xd(4).gt. 0.0) xd(4)= 0.0
else if (x(4) .lt. -adl) then
   x(4)= -adl
   if(xd(4) .lt. 0.0) xd(4)= 0.0
else
   continue
end if

temp= ua
if (abs(temp).gt. adl) then
    temp= sign(adl,temp)              ! limit ARI to aileron limit
end if
ari = (0.13*x(2) - 0.7)*temp
rs  = rd - pd*x(2)/57.3
xd(6)= rs - x(6)
```

```
err= rcom - .8*xd(6) - 10.0*ay
xd(5)= 20.2*( err + ari - x(5) )

if( abs(xd(5)) .gt. rrl) then
    xd(5)= sign(rrl, xd(5))           ! Rudder rate limit
end if
if(x(5).gt. rdl) then
    x(5)= rdl
    if(xd(5).gt. 0.0) xd(5)= 0.0
else if (x(5) .lt. -rdl) then
    x(5)= -rdl
    if(xd(5) .lt. 0.0) xd(5)= 0.0
else
    continue
end if
return
end

subroutine DISCRETE(time,ts,x,xd)
parameter (ll=20)
dimension x(*),xd(*)
common/controls/thtl,el,ail,rdr,pcom,qcom,rcom
common/output/op(ll)
if (time.lt. 5.0) then
  qcom= 0.0
  pcom= 0.0
  rcom= 0.0
else if (time.lt. 12.0) then
  qcom= 20.0
  thtl= 1.0
else if (time.lt. 16.0) then
  qcom= 0.0
  pcom= 300.0
else
  pcom = 0.0
  qcom = 0.0
end if
return
end
```

A pull-up at 20 deg/s is simulated, so that the angle of attack attains quite large values. When alpha reaches about 23° (Figure 4.7-8*a*), a large roll-rate command is applied; this causes the aileron and rudder actuators to saturate almost immediately (Figure 4.7-8*b*). The directional controls are then unable to control the sideslip tightly, and some of the angle of attack is rapidly converted to sideslip (Figure 4.7-8*c*) through kinematic coupling. As the roll and yaw rates build up (Figure 4.7-8*d*), the inertia coupling moment becomes strong. The elevator deflection then goes from a small negative value to its positive limit, as it tries to oppose the inertia coupling moment. Figure 4.7-8*e* shows the roll-angle variation, Figure 4.7-8*f* shows pitch attitude, and Figure 4.7-8*g* shows the decrease in airspeed during the maneuvers.

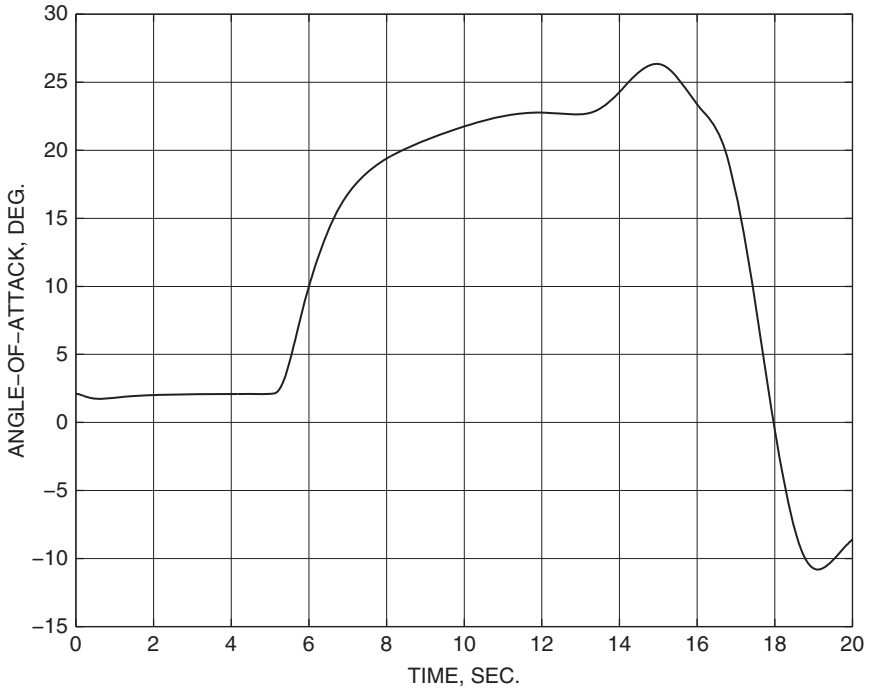

Figure 4.7-8*a* Simulation of limiting; alpha variation.

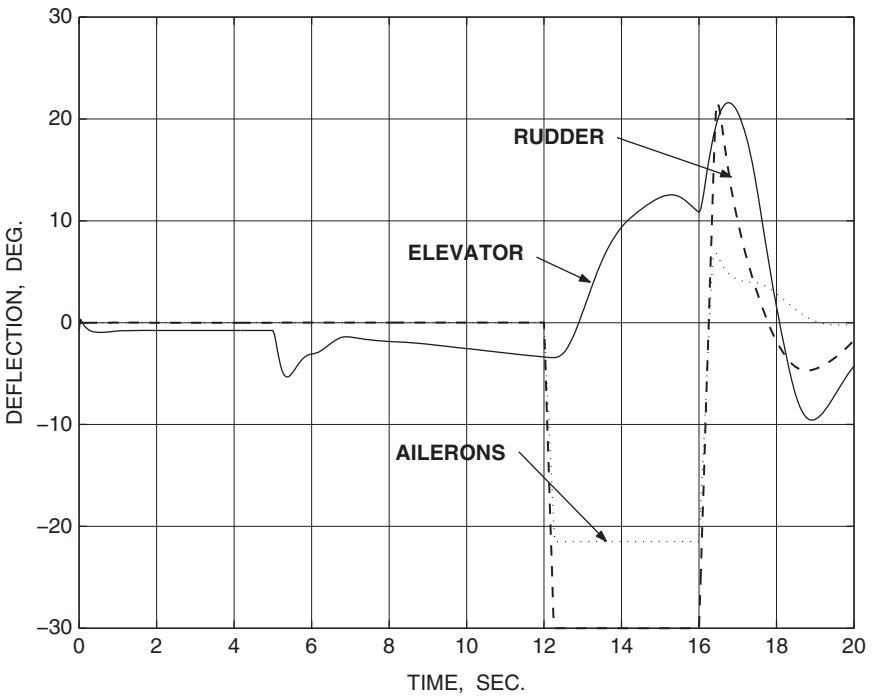

Figure 4.7-8*b* Simulation of limiting; control surface deflections.

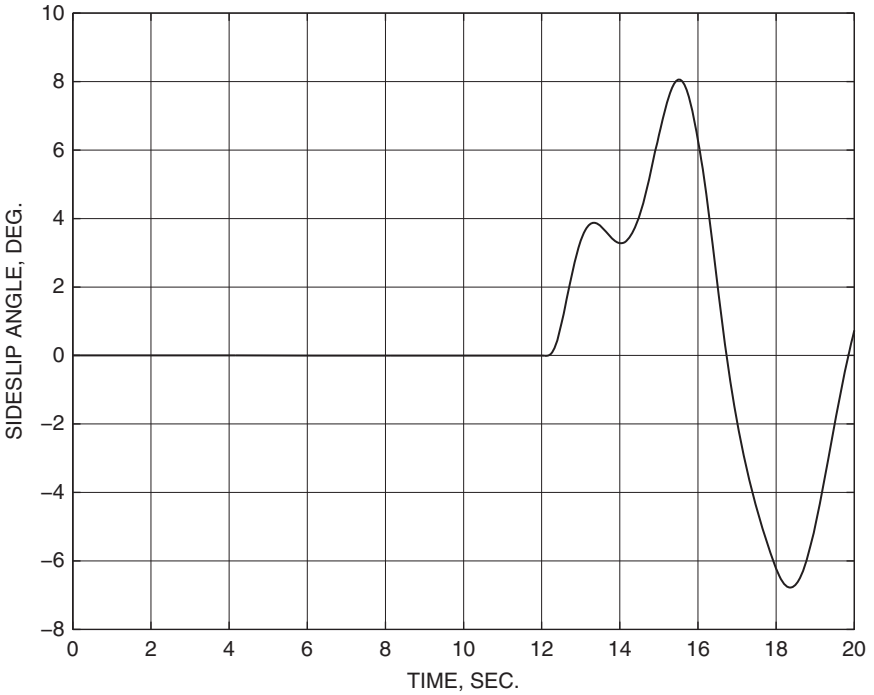

Figure 4.7-8*c* Simulation of limiting; sideslip variation.

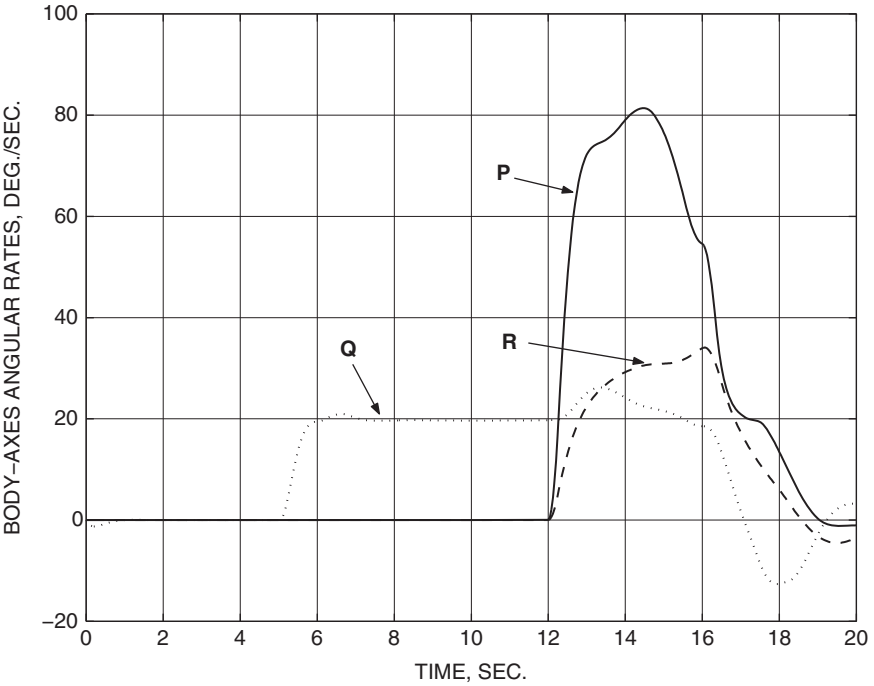

Figure 4.7-8*d* Simulation of limiting; aircraft angular rates.

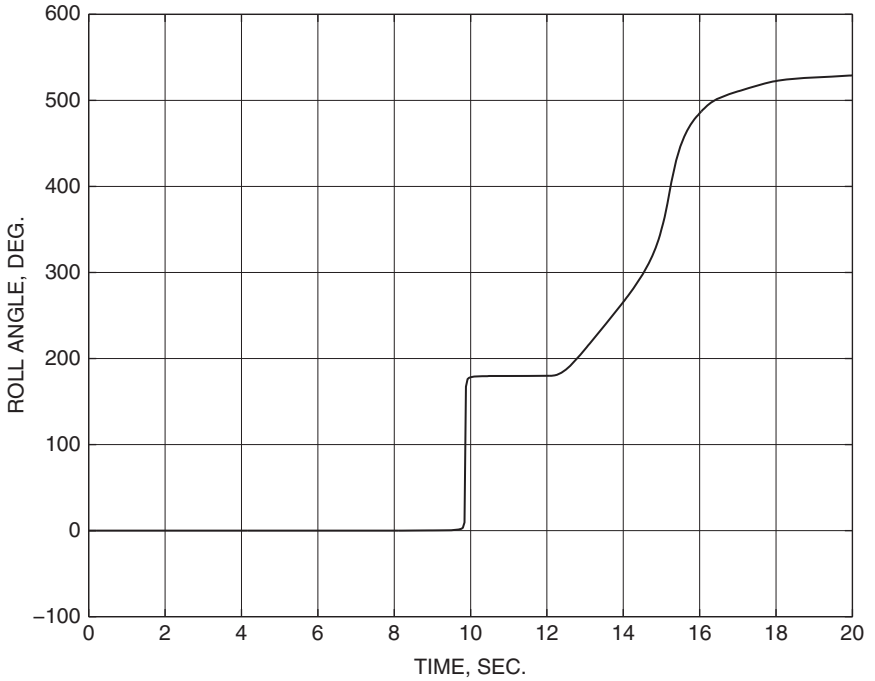

Figure 4.7-8*e* Simulation of limiting; roll angle variation.

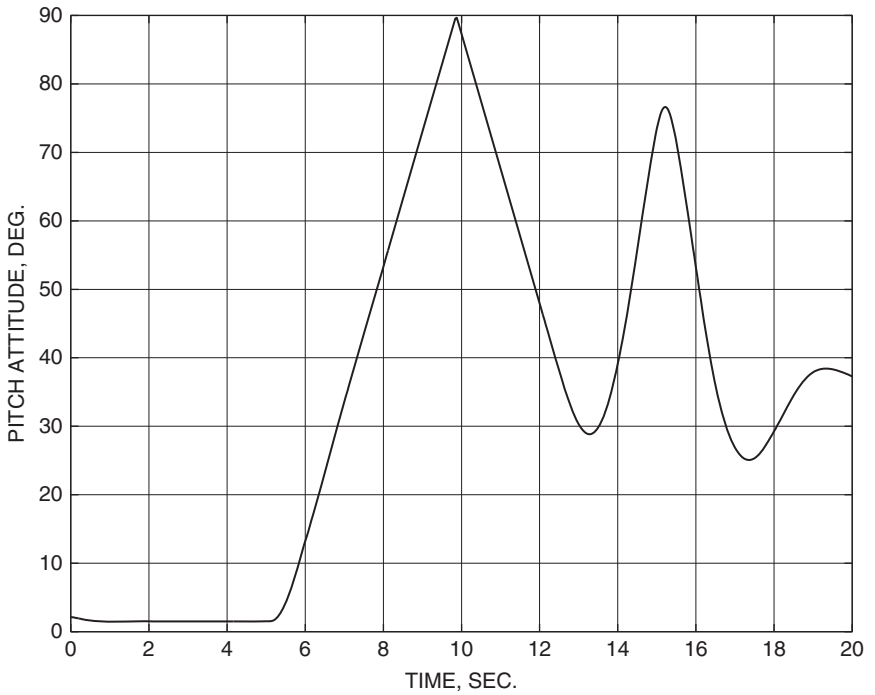

Figure 4.7-8*f* Simulation of limiting; pitch-attitude variation.

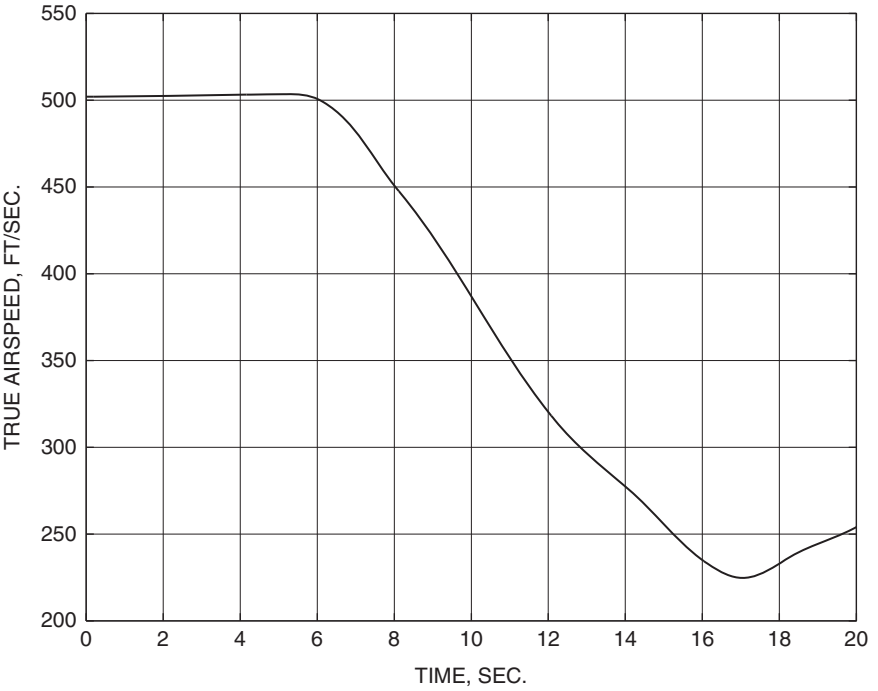

Figure 4.7-8*g* Simulation of limiting; airspeed variation.

In the flight condition illustrated, the available roll and yaw rates are insufficient to cause a pitch departure (due to inertia coupling), but the elevator saturation means that there is no longitudinal control available for 2 or 3 s. For this aircraft, pitch departure appears to be a problem only at very low dynamic pressure and high alpha, and more details can be found in the work of Nguyen et al. (1979). These types of problems are usually solved by using command limiters to limit the roll rate that the pilot can command or the angle of attack that can be reached through the longitudinal controls. The limiting values must be made functions of the flight conditions, and the design process is a lengthy one involving much nonlinear simulation. ■

4.8 SUMMARY

In this chapter we have described the effect of flight conditions on the aircraft modes, presented some background in handling qualities and control design criteria, and described the purpose and design requirements of a large number of commonly used control systems. The design examples are quite realistic, having been performed on nonlinear aircraft models that are quite accurately representative of two very different types of aircraft. An infinite number of variations on the designs are possible and some of these are suggested in the chapter problems. Time and space limitations have

not allowed the control designs to be gain scheduled over the aircraft envelope and to be evaluated thoroughly in terms of the handling qualities requirements, but the necessary cababilities have been developed.

The state-space formulation of modern control has provided an exceptionally convenient framework for the software and the use of classical design techniques. It should be evident that a primary requirement for successful design of aircraft control systems is an understanding of the physics of flight and that interpreting the results of simulations is a vital aspect of this. Classical control theory fits extremely well into this picture because it relates very closely to the physics of the problems and usually provides clues to the modifications needed to make the design successful. In the following chapters modern design techniques will be introduced. These techniques will come into their own in situations that we found difficult to handle up to this point, such as shaping the closed-loop time response when a number of poles and zeros all contribute significantly.

REFERENCES

AFWAL-TR-84-3105. *Proceedings of the Aeroservoelastic Specialists Meeting*, October 2-3, 1984, vols. I and II. Wright-Patterson AFB, Ohio: USAF Flight Dynamics Laboratory.

Ananthkrishnan, N., and S. Unnikrishnan. "Literal Approximations to Aircraft Dynamic Modes." *Journal of Guidance, Control, and Dynamics* 24, no. 6 (November–December 2001): 1196–1203.

Ashkenas, I. L. "Some Open and Closed-Loop Aspects of Airplane Lateral-Directional Handling Qualities." *AGARD Report* 533, 1966.

———. "Twenty-Five Years of Handling Qualities Research." *AIAA Journal of Aircraft* 21, no. 5 (May 1984): 289–301.

Bischoff, D. E. "Longitudinal Equivalent Systems Analysis of Navy Tactical Aircraft." AIAA paper 81-1775. *AIAA Guidance and Control Conference*, Albuquerque, NM, August 19–21, 1981.

Blakelock, J. H. *Automatic Control of Aircraft and Missiles*. New York: Wiley, 1965.

Bryan, G. H. *Stability in Aviation*. London: Macmillan, 1911.

Chalk, C. R. "Fixed-Base Simulator Investigation of the Effects of L_α and True Speed on Pilot Opinion Rating of Longitudinal Flying Qualities." *USAF ASD-TDR-63-399*. Wright-Patterson AFB, Ohio: USAF Flight Dynamics Laboratory, November 1963.

Chalk, C. R., T. P. Neal, and T. M. Harris. *Background Information and User Guide for MIL-F-8785B (ASG)*. Buffalo, N.Y.: Cornell Aeronautical Laboratories Inc., August 1969 (AFFDL-TR-69-72; AD860856).

Cooper, G. E., and R. P. Harper, Jr. "The Use of Pilot Rating in the Evaluation of Aircraft Handling Qualities." *NASA Technical Note D-5153*. Washington, D.C.: NASA, 1969.

Craig, S. J., and I. L. Ashkenas. *Background Data and Recommended Revisions for MIL-8785B (ASG), "Military Specification—Flying Qualities of Piloted Airplanes."* Technical Report TR-189-1. Hawthorne, Calif.: Systems Technology Inc., March 1971.

Etkin, B. *Dynamics of Atmospheric Flight*. New York: Wiley, 1972.

Gentry, T. A. "Guidance for the Use of Equivalent Systems with MIL-F-8785C." Paper 82–1355. *AIAA Atmospheric Flight Mechanics Conference*, San Diego, 1982.

George, F. L., and D. J. Moorhouse. "Relationship of the Flying Qualities Specification to Task Performance." *AFFTC/NASA-Dryden/AIAA Workshop Flight Testing to Identify Pilot Workload and Pilot Dynamics*. Edwards AFB, Calif., January 19–21, 1982.

Gerlach, O. H. "Developments in Mathematical Models of Human Pilot Behavior." *Aeronautical Journal* (July 1977): 293–305.

Hodgkinson, J. "Equivalent Systems Approach for Flying Qualities Specification." MCAIR 79–017. Paper presented at *SAE Aerospace Control and Guidance Systems Committee Meeting*, Denver, Colo., March 7–9, 1979.

Kisslinger, R. L., and M. J. Wendle. "Survivable Flight Control System Interim Report," No. 1, "*Studies Analysis and Approach, Supplement for Control Criteria Studies*." Technical Report AFFDL-TR-71-20, suppl. 1. Wright-Patterson AFB, Ohio: Air Force Flight Dynamics Laboratory, May 1971.

Kleinman, D. L., S. Baron, and W. H. Levison. "An Optimal Control Model of Human Response." Part I: Theory and Validation; Part II: Prediction of Human Performance in a Complex Task. *Automatica* 6 (1970): 357–369.

McRuer, D. T., D. Graham, E. Krendel, and W. Reisiner, Jr. *Human Pilot Dynamics in Compensatory Systems*. AFFDL-TR-65-15. USAF, Wright-Patterson AFB, Ohio: Air Force Flight Dynamics Laboratory, 1965.

McRuer, D., I. Ashkenas, and D. Graham. *Aircraft Dynamics and Automatic Control*. Princeton, N.J.: Princeton University Press, 1973.

MIL-F-8785C. "U.S. Dept. of Defense Military Specification: Flying Qualities of Piloted Airplanes." November 5, 1980.

MIL-F-9490D. "Flight Control Systems: Design, Installation, and Test of, Piloted Aircraft, General Specification for." USAF, June 1975.

Moorhouse, D. J., and R. J. Woodcock. "Background Information and User Guide for MIL-F-8785C." *AFWAL-TR-81-3109 (AD-A119-421)*. Wright-Patterson AFB, Ohio: Air Force Wright Aeronautical Laboratories, July 1982.

Neal, T. P., and R. E. Smith. "An In-flight Investigation to Develop Control System Design Criteria for Fighter Airplanes." *AFFDL-TR-70-74*, vols. I and II. Wright-Patterson AFB, Ohio, Air Force Flight Dynamics Laboratory, December 1970.

Nguyen, L. T., et al. "Simulator Study of Stall/Post-Stall Characteristics of a Fighter Airplane with Relaxed Longitudinal Static Stability." *NASA Tech. Paper 1538*. Washington, D.C.: NASA December 1979.

O'Hara, F. "Handling Criteria." *Journal of the Royal Aeronautical Society* 71, no. 676 (1967): 271–291.

Onstott, E. D., and W. H. Faulkner. "Production Evaluation and Specification of Closed-Loop and Multi-Axis Flying Qualities." *AFFDL-TR-78-3*. Wright-Patterson AFB, Ohio: Air Force Flight Dynamics Laboratory, February 1978.

Roskam, J. *Airplane Flight Dynamics and Automatic Flight Controls*. Lawrence, Kans.: Roskam Aviation and Engineering Corp., 1979.

Rynaski, E. G. "Flying Qualities in the Time Domain." AIAA paper 85-1849. *AIAA Guidance, Navigation and Control Conference*, Snowmass, Colo., August 1985.

Sheridan, T. B., and W. R. Ferrell. *Man-Machine Systems: Information, Control, and Decision Models of Human Operator Performance*. Cambridge, Mass.: MIT Press, 1974.

Shomber, H. A., and W. M. Gertsen. "Longitudinal Handling Qualities Criteria: An Evaluation." *Journal of Aircraft* 4, no. 4 (1967): 371–376.

Tobie, H. N., E. M. Elliot, and L. G. Malcom. "A New Longitudinal Handling Qualities Criterion." *Proceedings of the National Aerospace Electronics Conference*, Dayton, Ohio, May 16–18, 1966, pp. 93–99.

Toles, R. D. "Application of Digital Multi-Input/Multi-Output Control Law with Command Path Blended Gains for the Pitch Axis Task-Tailored Air Combat Mode of the AFTI/F-16." *Proceedings of the 1985 American Control Conference*, Boston, June 1985, p. 1475.

PROBLEMS

Section 4.2

4.2-1 Use the results of Section 4.2 to write a program that will calculate the damping and natural frequency of the phugoid and short-period modes from the dimensionless longitudinal stability derivatives. Use it to check the results given in Table 4.2-1.

4.2-2 Write a program to determine the lateral-directional modes from the appropriate dimensionless derivatives and use it to check the results of Example 4.2-1. Determine both the approximate values from the equations in Section 4.2 and accurate values from the eigenvalues of the coefficient matrices.

Section 4.4

4.4-1 When the F-16 model is trimmed for level flight at 30,000 ft and 820 ft/s, the dynamic pressure and angle of attack are the same as those of the nominal sea-level condition in Table 3.6-3. The A- and B-matrices are given by

$$A = \begin{array}{c} \begin{matrix} v_T & \alpha & \theta & q \end{matrix} \\ \begin{bmatrix} -5.9172E-03 & 8.8482E+00 & -3.2170E+01 & -3.5136E-01 \\ -9.5423E-05 & -6.2426E-01 & 0.0000E+00 & 9.6439E{-}01 \\ 0.0000E+00 & 0.0000E+00 & 0.0000E+00 & 1.0000E+00 \\ 2.4638E-11 & 8.2290E-01 & 0.0000E+00 & -6.6011E-01 \end{bmatrix} \end{array}$$

$$B = \begin{array}{c} \begin{matrix} \delta_e \end{matrix} \\ \begin{bmatrix} 1.7391E-01 \\ -1.3172E-03 \\ 0.0 \\ -1.7569E-01 \end{bmatrix} \end{array}$$

Explain how and why these dynamic equations differ from those in Example 4.4-1. Augment these dynamics with the same alpha filter and elevator actuator as in the example and find α and q feedback gains that will

yield closed-loop longitudinal dynamics as close as possible to those obtained in Example 4.4-1.

4.4-2 Using the same flight conditions as in Problem 4.4-1, the lateral-directional dynamics of the F-16 model are

$$A = \begin{array}{c} \begin{matrix} \beta & \phi & p & r \end{matrix} \\ \begin{bmatrix} -.19729 & .039205 & .036657 & -.99645 \\ 0 & 0 & 1.0 & .036878 \\ -30.666 & 0 & -2.2538 & .40705 \\ 8.5461 & 0 & -.015556 & -.29186 \end{bmatrix} \end{array}$$

$$B = \begin{array}{c} \begin{matrix} \delta_a & \delta_r \end{matrix} \\ \begin{bmatrix} 1.8078E-04 & 4.9356E-04 \\ 0 & 0 \\ -0.73388 & 0.13165 \\ -0.031891 & -0.062067 \end{bmatrix} \end{array}$$

Determine and identify the modes. Find suitable feedback gains for basic lateral-directional stability augmentation, as in Example 4.4-3. Compare the roll-rate response to an aileron doublet with the response shown in Example 4.4-3.

4.4-3 Repeat Example 4.4-3 with washout time constants of 0.5 s and 2.0 s and describe the difference in behavior and the effect on the dutch roll dampling.

4.4-4 Repeat Example 4.4-2 using the F-16 dynamics given in Problem 4.4-1. Is the lag compensator still useful?

Section 4.5

4.5-1 Repeat the pitch-CAS design (Example 4.5-1) using the F-16 dynamics given in Problem 4.4-1. Does the position of the PI zero need to be changed? Could this design be made to work, over at least the low-Mach part of the envelope, by changing only the proportional gain? Is it possible to say anything about the need for gain scheduling the controller? Determine the step response with and without the PI zero.

4.5-2 Repeat the design of the normal acceleration CAS in Example 4.5-2, but with the accelerometer placed at the aircraft cg. Attempt to obtain a step response that is fast but well damped and similar to that shown in Figure 4.5-6.

4.5-3 Use the MATLAB program NLSIM from Chapter 3 to simulate some maneuvers with the lateral-directional CAS from Example 4.5-3. In the state equation MATLAB function, use linear state equations for the longitudinal and lateral-directional dynamics but model the nonlinear ARI and yaw-rate feedback. Compare the results with and without the ARI operating.

Section 4.6

4.6-1 Redesign the pitch-attitude hold in Example 4.6-1 using the short-period approximation, with an additional integrator to produce pitch from pitch rate. Evaluate the design with a step-response simulation performed on the full dynamics.

4.6-2 Redesign the pitch-attitude hold in Example 4.6-2 with the PI zero placed at $s = -0.1$; compare the step response with that given in the text. Can this design be performed using the short-period approximation?

4.6-3 Attempt to design a Mach-hold autopilot using the same dynamics as in Example 4.6-3 and Figure 4.6-6, but with Mach as the controlled variable. Show that the throttle-to-Mach transfer function contains an NMP zero that makes this difficult or impossible. What is the way out of this difficulty?

4.6-4 Redesign the d-loop of the glide-slope controller in Example 4.6-4 with the PI zero at $s = -0.1$. Also attempt to design the lead compensator so that the elevator is less active during the acquisition of the glide slope. Compare the simulation results with those given in the text.

4.6-5 Modify Example 4.6-5 to use PI control and lead compensation (if necessary) so that zero steady-state roll angle error can be achieved.

Section 4.7

4.7-1 Use NLSIM to repeat the pitch CAS nonlinear simulation in Example 4.7-1 but, instead of the nonlinear F-16 model, use the linear state equations for the nominal flight condition. Show graphs for comparison with those in Example 4.7-1 and discuss the differences.

4.7-2 Reproduce the glide-path and flare simulations described in Examples 4.7-3 and 4.7-4. Add code to simulate rate limiting in the elevator actuator and determine how low the maximum elevator slew rate can be before the results are significantly changed.